UNIVERSIDADE FEDERAL DE MINAS GERAIS

School of engineering

Graduate Program in Mechanical Engineering

Thiago Torres Martins Rocha

FEASIBILITY OF A SIMPLIFIED MODEL FOR A LATENT THERMAL ENERGY STORAGE UNIT FOR INTEGRATION WITH MULTIPHYSICS SYSTEMS

Belo Horizonte

2023

Thiago Torres Martins Rocha

FEASIBILITY OF A SIMPLIFIED MODEL FOR A LATENT THERMAL ENERGY STORAGE UNIT FOR INTEGRATION WITH MULTIPHYSICS SYSTEMS

Thesis submitted to the Graduated Program in Mechanical Engineering of the Federal University of Minas Gerais, as a partial requirement for obtaining the degree of Doctor in Mechanical Engineering.

Concentration area: Energy and Sustainability

Advisor: Prof. Raphael Nunes de Oliveira

Co-advisor: Prof. Paulo Vinicius Trevizoli

Belo Horizonte

2023

Rocha, Thiago Torres Martins.
R672f Feasibility of a simplified model for a latent thermal energy storage unit for integration with multiphysics systems [recurso eletrônico] / Thiago Torres Martins Rocha. - 2023.
1 recurso online (97 f. : il., color.) : pdf.

Orientador: Raphael Nunes de Oliveira.
Coorientador: Paulo Vinicius Trevizoli.

Tese (doutorado) - Universidade Federal de Minas Gerais, Escola de Engenharia.

Apêndicas: f. 90-97.

Bibliografia: f. 76-89.
Exigências do sistema: Adobe Acrobat Reader.

1. Engenharia mecânica - Teses. 2. Calor - Armazenamento - Teses. 3. Energia - Teses. 4. Porosidade - Teses. 5. Dinâmica dos fluidos computacional - Teses. 6. Condutividade térmica - Teses. 7. Dinâmica dos fluidos - Teses. I. Oliveira, Raphael Nunes de. II. Trevizoli, Paulo Vinicius . III. Universidade Federal de Minas Gerais. Escola de Engenharia. IV. Título.

CDU: 621(043)

Ficha catalográfica elaborada pela Bibliotecária Ângela Cristina Silva CRB/6 2361
Biblioteca Prof. Mário Werneck, Escola de Engenharia da UFMG

UNIVERSIDADE FEDERAL DE MINAS GERAIS
ESCOLA DE ENGENHARIA
PROGRAMA DE PÓS-GRADUAÇÃO EM ENGENHARIA MECÂNICA

FOLHA DE APROVAÇÃO

FEASIBILITY OF A SIMPLIFIED MODEL FOR A LATENT THERMAL ENERGY STORAGE UNIT FOR INTEGRATION WITH MULTIPHYSICS SYSTEMS

THIAGO TORRES MARTINS ROCHA

Tese submetida à Banca Examinadora designada pelo Colegiado do Programa de Pós-Graduação em Engenharia Mecânica da Universidade Federal de Minas Gerais, constituída pelos Professores: Dr. Raphael Nunes de Oliveira (Orientador - Departamento de Engenharia mecânica/UFMG), Dr. Paulo Vinicius Trevizoli (Coorientador - Departamento de Engenharia Mecânica/UFMG), Dr. Antonio Augusto Torres Maia (Departamento de Engenharia Mecânica/UFMG), Dr. Luiz Machado (Departamento de Engenharia Mecânica/UFMG), Dr. Ralney Nogueira de Faria (Departamento de Engenharia Mecatrônica/CEFET) e Dr. Felipe Raul Ponce Arrieta (Departamento de Engenharia Mecânica/PUC Minas), como parte dos requisitos necessários à obtenção do título de **"Doutor em Engenharia Mecânica"**, na área de concentração de "**Energia e Sustentabilidade"**.

Tese aprovada no dia 14 de dezembro de 2023.

Por:

Documento assinado eletronicamente por **Raphael Nunes de Oliveira**, **Servidor(a)**, em 21/12/2023, às 09:21, conforme horário oficial de Brasília, com fundamento no art. 5º do Decreto nº 10.543, de 13 de novembro de 2020.

Documento assinado eletronicamente por **Felipe Raul Ponce Arieta**, **Usuário Externo**, em 21/12/2023, às 15:55, conforme horário oficial de Brasília, com fundamento no art. 5º do Decreto nº 10.543, de 13 de novembro de 2020.

Documento assinado eletronicamente por **Antonio Augusto Torres Maia**, **Professor do Magistério Superior**, em 21/12/2023, às 15:59, conforme horário oficial de Brasília, com fundamento no art. 5º do Decreto nº 10.543, de 13 de novembro de 2020.

Documento assinado eletronicamente por **Luiz Machado**, **Professor do Magistério Superior**, em 21/12/2023, às 17:05, conforme horário oficial de Brasília, com fundamento no art. 5º do Decreto nº 10.543, de 13 de novembro de 2020.

Documento assinado eletronicamente por **Paulo Vinicius Trevizoli**, **Professor do Magistério Superior**, em 22/12/2023, às 04:33, conforme horário oficial de Brasília, com fundamento no art. 5º do Decreto nº 10.543, de 13 de novembro de 2020.

Documento assinado eletronicamente por **Ralney Nogueira de Faria**, **Usuário Externo**, em 22/12/2023, às 11:50, conforme horário oficial de Brasília, com fundamento no art. 5º do Decreto nº 10.543, de 13 de novembro de 2020.

A autenticidade deste documento pode ser conferida no site https://sei.ufmg.br/sei/controlador_externo.php?acao=documento_conferir&id_orgao_acesso_externo=0, informando o código verificador **2900267** e o código CRC **D0A19184**.

ACKNOWLEDGEMENTS

Firstly, I thank to God for my life, for guiding me here, and providing me the strengths to move forward. Besides, it would not be possible to arrive at this stage without the help and encouragement received throughout this journey. My thanks go to:

- All my family and friends, who always believed in me and provided me the support in every step. Special thanks to my parents, Karla, Gilberto, and Efigênio, my sister Carol, my wife Luciana, and my kids Letícia and Augusto.
- My friend and professor Fernando, who encouraged me in the beginning of the academic trajectory.
- My advisors, Raphael Nunes and Paulo Trevizoli, for their availability, wise advises, and effort employed in this work.
- Professors and students who directly contributed with this work: Antônio Maia, Rudolf Huebner, Alexandre Abrão, Luiz Machado, and my partners Ramon and Guilherme.
- Dr. Tasso, for helping me to keep my body and mental health during the past years.
- IFMG Congonhas, specially my colleagues from the Department of Mechanics, who supported me with a lower teaching workload.

I also acknowledge CAPES for providing me four months of scholarship, FAPEMIG who financed the project APQ-00454-21, and the Graduate Program of Mechanical Engineering, especially Marina, always ready to give a hand.

Thanks to everyone.

This study was financed in part by the Coordenação de Aperfeiçoamento de Pessoal de Nível Superior - Brasil (CAPES) - Finance Code 001.

ABSTRACT

The goal of this work is to assess the suitability of a simplified model for the melting of a phase-change material, verifying its accuracy and simulation time. Initially, a mathematical model is formulated and solved with Ansys® Fluent, being validated with two experimental datasets, using lauric acid. The effects of altering the porosity constant, material properties, and their interaction were assessed. It was evidenced that, by holding the porosity constant of validation in another geometry, absolute average deviations as high as 38.0% could be achieved, whereas this error could be reduced to 5.7% with a proper adjustment. The numerical results of this computational fluid dynamics model were also used to derive an effective thermal conductivity, for later use. Subsequently, a simplified model based on the pure conduction was developed and implemented in Python language, including the natural convection of the liquid phase-change material trough the effective thermal conductivity. A horizontal shell-and-tube unit was chosen, since it is one of the most employed configuration in heat exchangers using phase-change materials. The results of this simplified model revealed maximum and absolute average deviations of 8.17% and 4.32%, compared to the computational fluid dynamics model, and 7.43 % and 1.67%, compared to experimental data, respectively, with a 3500 fold reduction on the simulation time. Therefore, the proposed model can be considered feasible for integration with multiphysics systems.

Keywords: latent thermal energy storage; phase-change material; computational fluid dynamics; porosity constant; effective thermal conductivity.

RESUMO

O objetivo deste trabalho é avaliar a adequação de um modelo simplificado para a fusão de um material com mudança de fase, verificando sua precisão e tempo de simulação. Inicialmente, um modelo matemático é formulado e resolvido com o Ansys® Fluent, sendo validado com dois conjuntos de dados experimentais, utilizando o ácido láurico. Os efeitos da alteração da constante de porosidade, das propriedades do material e de sua interação foram avaliados. Evidenciou-se que, mantendo-se a constante de porosidade de validação em outra geometria, desvios médios absolutos de até 38,0% são obtidos, enquanto esse erro pode ser reduzido para 5,7% com um ajuste adequado. Os resultados numéricos de dinâmica de fluidos computacional também foram utilizados para derivar uma condutividade térmica efetiva, para uso subsequente. Posteriormente, um modelo simplificado baseado na condução pura foi desenvolvido e implementado em linguagem Python, incluindo a convecção natural da fase líquida do material de mudança de fase através da condutividade térmica efetiva. Adotou-se uma unidade horizontal do tipo casco e tubo por ser largamente utilizada em trocadores de calor que utilizam materiais com mudança de fase. Os resultados deste modelo simplificado revelaram desvios máximo e médio absoluto de 8,17% e 4,32%, comparados ao modelo de dinâmica de fluidos computacional, e 7,43% e 1,67%, comparados aos dados experimentais, respetivamente, com uma redução de 3500 vezes no tempo de simulação. Portanto, o modelo proposto pode ser considerado viável para integração em sistemas multifísicos.

Palavras-chave: termoacumulação por calor latente; material de mudança de fase; dinâmica dos fluidos computacional; constante de porosidade; condutividade térmica efetiva.

NOMENCLATURE

b	Liquid layer thickness [m]
C	Porosity constant [Pa s m^{-2}]
c_p	Specific heat at constant pressure [J kg^{-1} K^{-1}]
D	Diameter [m]
f	Liquid fraction [-]
g	Gravitational acceleration [m s^{-2}]
h	Convective heat transfer coefficient [W m^{-2} K^{-1}], sensible enthalpy [J kg^{-1}]
H	Specific (total) enthalpy [J kg^{-1}]
k	Thermal conductivity [W m^{-1} K^{-1}]
L	Latent heat of fusion [J kg^{-1}], length [m]
Nu	Nusselt number [-]
P	Pressure [Pa]
Pr	Prandtl number [-]
r	Radial coordinate [m]
R	Radius [m]
Ra	Rayleigh number [-]
S_h	Energy source term [W m^{-3}]
S_u	Momentum source term [Pa m^{-1}]
t	Time [s]
T	Temperature [°C, K]
u	Velocity vector [m s^{-1}]
x	X coordinate [m]
X	characteristic length [m]
y	Y coordinate [m]
ΔH	Specific latent heat [J kg^{-1}]

Greek symbols

α	Thermal diffusivity [m^2 s^{-1}]
β	Thermal expansion coefficient [K^{-1}]
μ	Dynamic viscosity [Pa s]
ν	Kinematic viscosity [m^2 s^{-1}]
ρ	Density [kg^1 m^{-3}]

Subscripts

ef	Effective
i	Inner
ini	Initial
l	Liquid
m	Melting
o	Outer
ref	Reference
s	Solid
sl	Solid-liquid interface
W	Wall

Abbreviations

AAD	Absolute average deviation
AHC	Apparent heat capacity
CFD	Computational fluid dynamics
FDM	Finite differences method
FEM	Finite elements method
FVM	Finite volumes method
GCI	Grid convergence index
HTF	Heat transfer fluid
LTES	Latent thermal energy storage
NASA	National Aeronautics and Space Administration
NePCMs	Nano-enhanced phase-change materials

PCM	Phase-change material
STES	Sensible thermal energy storage
TES	Thermal energy storage
TTES	Thermochemical thermal energy storage
VOF	Volume-of-fluid

CONTENTS

1. INTRODUCTION

Over the last decades, several international treats to limit environment damages were proposed. More recently, in 2015, the Paris Agreement was firmed aiming to limit the rise on the global average temperature, in the present century, bellow 2ºC, and ideally, up to 1.5 ºC (UNFCCC, 2015). One year later, the Kigali Amendment set goals to further restrict the emissions of hydrofluorocarbons (HFCs). While the global energy consumption is estimated to keep growing (1.3% in 2021, compared to 2019 pre-pandemic level (bp, 2022)), alternatives to improve energy efficiency are imperative. In this context, the incorporation of thermal energy storage (TES) with renewable energy is a promising alternative towards a more sustainable economy (IRENA, 2020).

Briefly, TES refers to an alternative that stores energy at one point in time, to be harvested in a different period. Among the several benefits, it allows to flatten the mismatch between energy supply and demand, besides providing a better thermal management. This technique can be based on different principles: (i) sensible thermal energy storage (STES), in which energy is stored/recovered due a temperature variation on the storage medium; (ii) latent thermal energy storage (LTES), where a phase-change material (PCM) is subjected to a physical state change, to store/release energy through its latent heat content; (iii) thermochemical thermal energy storage (TTES), based on endothermic or exothermic reactions (Rocha *et al*., 2023b). Among the three, TTES stands out due to its highest energy density, requiring small storage volumes, but it is still a developing technology (Hameed *et al*., 2022). On its turn, STES is quite mature, being largely used in commercial scales. Nevertheless, its low energy density, traduced in large volumes, is a major drawback (Dong *et al*., 2022). Lastly, compared to STES, LTES has a higher energy density and provides an almost constant charge/discharge temperature, making PCMs suitable for large-scale and small-scale utilization. In contrast, a significant limitation can be considered the low heat transfer rates, due to the low thermal conductivity of PCMs.

Recently, LTES has been investigated in several energy-related fields, including concentrated solar power plants (Jayathunga *et al*., 2023), photovoltaic (Taqi Al-Najjar and Mahdi, 2022) and photovoltaic/thermal collectors (Gürbüz *et al*., 2023), solar heating (Yan *et al*., 2023), solar-based desalination (Kaabinejadian *et al*., 2023), heat pumps (Sun *et al*., 2023), refrigeration appliances (Ismail *et al*., 2023), and thermal management of buildings (Arfi *et al*., 2023). Novel applications of phase-changes materials are also reported (Ismail *et al*., 2022).

Due to the complex nature of the melting/solidification of PCMs, phase-change models require a set of assumptions to solve the coupled equations of mass, momentum, and energy, making the simulation a viable task. Notwithstanding, the computational resources required to perform such simulations are significant and the processing can be extended from a few days to several weeks, depending on the complexity. Nowadays, the majority of investigations dealing with the melting of PCMs employ commercial CFD software to perform this task. Most of them are based on the approach called to enthalpy-porosity scheme, which in turn, includes the porosity constant. Lately, there has been an increasing awareness concerning the proper selection of this variable, but a comprehensive study evaluating the simultaneous alteration of the porosity constant and the PCM thermophysical properties is missing in the literature. Therefore, such investigation is one of the contributions of the present work.

When the LTES unit is only one piece in a global system, e.g. in power and refrigeration plants, it is difficult to simulate the full melting process together with the whole cycle. It occurs due to the possible incompatibility between the platforms where the models were implemented and also due to the computational cost. In such cases, a simplified model, but accurate enough, must be developed for the PCM phase-change, allowing its integration with the remaining components. An alterative for this strategy is to develop a mathematical model that solves only the heat conduction equation, incorporating the natural convection trough an effective thermal conductivity. Often, a validated CFD model is used to generate this parameter that feeds the simplified version. However, to the best of the author knowledge, for a horizontal shell-and-tube configuration, only one dataset is available in the literature. Besides, the validation of the models employing this data were done considering the temperatures of the heat transfer fluid, used as the boundary conditions, while the actual charge condition of the PCM was not assessed. Therefore, there is a need to verify the suitability of a simplified mathematical model that is capable to reproduce the state-of-charge of the LTES unit, allowing its coupling into a more comprehensive system, such as a small-scale refrigerator. This is another contribution of the present study.

1.1. Objectives

The main goal of the present study is to assess the feasibility to use a simplified model for the melting of a PCM, in terms of accuracy and simulation time, that is properly validated and capable to be integrated with a multiphysics system.

Specific objectives of this work are:

- To develop a comprehensive (CFD) model to investigate the melting of a PCM, solving the set of mass, momentum, and energy equations to account the natural convection.
- To investigate the role of the PCM properties and its combining effect with the porosity constant on the accuracy of the numerical solution.
- To develop a simplified model for the PCM melting in a horizontal shell-and-tube unit, based on the pure conduction, but including the natural convection through the effective thermal conductivity.
- To describe a methodology to calculate the effective thermal conductivity.
- To verify the applicability of existing correlations to predict the effective thermal conductivity for the PCM melting in a horizontal shell-and-tube unit.

2. LITERATURE REVIEW

This chapter presents the literature review of phase-change materials regarding its applications in latent thermal energy storage systems. Section 2.1 presents an overview on LTES systems and a classification of PCMs. Subsequently, section 2.2 describes some approaches to model the melting/solidification problem, while section 2.3 introduces some numerical methods commonly used. As commented in the Introduction, PCMs possess low thermal conductivities, which leads to low heat transfer rates. Therefore, one of the major research efforts is to improve the heat transfer characteristics of LTES units. Some alternatives to do so are discussed in section 2.4. In subsection 2.5, the state of the art concerning the effect of altering the PCM properties, the porosity constant value, their interaction, and the relation with the natural convection intensity is presented. In subsection 2.6, the effective thermal conductivity is discussed in terms of available correlations for its prediction, with emphasis on the horizontal shell-and-tube configuration. The main outcomes and literature gaps are indicated in the last subsection.

2.1. Overview

Differently from STES, where energy is stored trough an increase in the medium temperature – indicated in Eq. 1, the working principle of LTES is to store/release heat through a phase-change of a material – indicated in Eq. 2. Often, the sensible term contributes to the totality of energy stored into the LTES system, as illustrated in Figure 1 for a pure or eutectic substance. Different alterations of physical-states may occur, e.g. solid-solid, solid-liquid, liquid-gas, and solid-gas. Solid-solid transformations have been reported in cutting edge technologies such as memory of electronic devices (Le Gallo and Sebastian, 2020). Liquid-gas and solid-gas transformations would require large volumes to store energy, being not recommended for practical use. For LTES applications, solid-liquid states are, universally, the choice.

Figure 1. Energy stored in a latent thermal energy storage system with contribution of the sensible term.

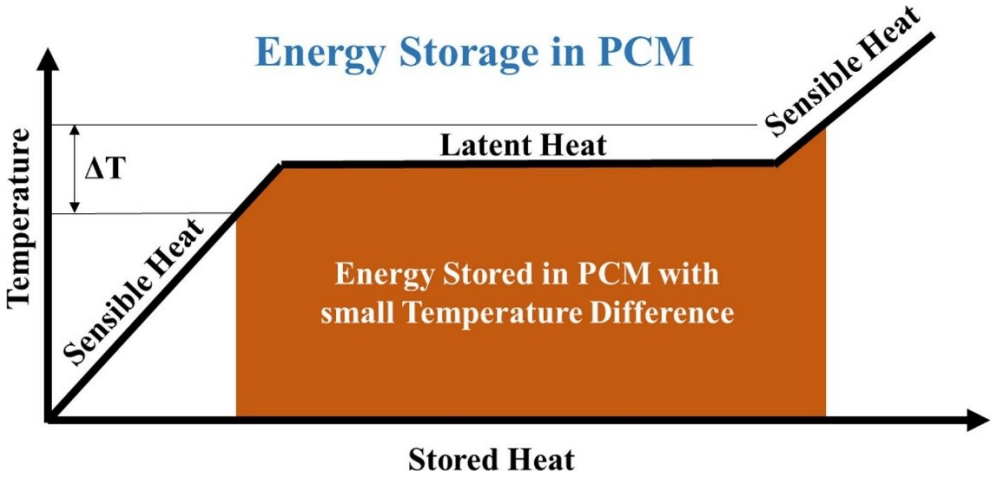

Source: Hameed *et al*. (2022).

$$Q = mc_{\mathrm{p}}\Delta T \tag{1}$$

$$Q = mL \tag{2}$$

where Q is the amount of energy being stored/released, m is the mass of the medium, c_{p} is the specify heat at constant pressure, ΔT is the temperature variation, and L is the latent heat of the phase-change. To be considered a good candidate, the PCM must present: suitable termophysical properties, long-term thermochemical stability, none toxicity, low or none flammability, high availability, and low cost (Jouhara *et al*., 2020). In practice, there is no ideal material, so that the pros and cons must be balanced. There are several ways to categorize PCMs, but they are commonly grouped into organics, inorganics, and eutectics. The main subgroup on the first category are the paraffin waxes, which consist in saturated hydrocarbons, with the number of carbons usually varying from 15 to 30 (Alva *et al*., 2018). These materials possess good thermal stability and low corrosiveness, but suffer from poor thermal conductivity. Fatty acids, such as lauric acid, have become widely investigated PCMs, due to their characteristics of high heat capacity, low vapor pressure, and good long-term thermochemical stability (Yang *et al*., 2019). Besides, its melting temperature makes it suitable for a wide range of applications involving heating and cooling, when the desired temperature is about 45°C. Concerning inorganic PCMs, salts and hydrated salts are the most used. They have higher thermal conductivity, compared to paraffin waxes, but present worse thermal stability and more corrosiveness issues. The eutectics are formed by a mixture of two or more

PCMs, either organic or inorganic, which present a constant (or small range of) melting/solidification temperature.

As briefly mentioned in the Introduction section, the utilization of PCMs may improve the performance of several systems, but the purpose of adding the thermal accumulator may differ. The objective of the LTES unit may be (i) the storage and recovery of heat in distinct periods, which is the definition of a TES unit itself, but it can also be (ii) a better thermal management of the system. An example in the first case is the integration of an ice tank in an air-conditioning system, where the final goal is to reduce the electricity bill and/or to reduce the capital expenses. This is achieved through one or more of the following benefits (Rocha *et al*., 2023a):

- Reduced energy consumption during peak periods: when time-of-use tariffs apply, the peak demand is offset to off-peak periods. This is done by operating the system during the off-peak period in order to charge the thermal accumulator, which is responsible to supply the demand during the peak-period. Besides, the power factor is improved over the day, avoiding surcharges. In this way, the electricity bill is reduced;
- Higher system efficiency: during night time, when ambient temperature is lower, the refrigeration cycle runs with higher COP. If this efficiency improvement suppresses the energy losses during the charging/discharging process, the final energy consumption is even lowered;
- Smaller capacity equipment: with a more efficient system, an equipment with smaller rated power (lower consumption and cost) can be selected for the same function. Besides, depending on the operational strategy (partial storage), the charging process can be levelled over the entire cycle, further reducing the nominal power. These factors lead to a reduction of the capital expenses.

Solar power plants, that present intermittent generation, may also apply a LTES reservoir to recover the heat when solar radiation is not available or when the energy demand is higher than the production. The energy stored in the PCM may be directly used as heat or converted back into electricity, e.g. generating steam for turbines. In the second case, systems such PV panels, refrigerators, and batteries are also enhanced by the addition of PCMs, but in these situations, the storage of heat with further recovery, is not the purpose. The objective is to achieve a better thermal management, avoiding the superheat of some components, which could degrade the performance. This is achieved since the excess heat is absorbed by the PCM with none or a

small temperature variation during its phase-change. Subsequently, instead of recovering the heat to the system, it is released to the ambient air during the off-periods.

2.2. Mathematical modelling of melting/solidification

Latent thermal energy storage systems are, intrinsically, a phase-change process, which is a complex moving boundary problem. Besides, phenomena such natural convection, PCM thermal expansion, and supercooling may occur and interact between them, making the physical description a difficult task. In this sense, analytical results are limited to idealized situations, e.g. infinite or semi-infinite regions with simple boundary and initial conditions, and because of this, approximate solutions and numerical methods were already reported in 1959 by Carslaw and Jaeger. The first analytical discussion concerning the phase-change problem, particularly the solidification of water, was published by J. Stefan in 1891. It treated the medium as a semi-infinite rectangular domain, considering one-dimensional pure conduction. Since there, the melting and solidification were referred to as Stefan´s problem. Figure 2 illustrates this problem, governed by Eqs. 3-5, for the liquid phase, solid phase, and the interface, respectively, with the boundary condition at the interface given by Eq. 6.

Figure 2. Domain of Stefan´s problem in rectangular coordinates.

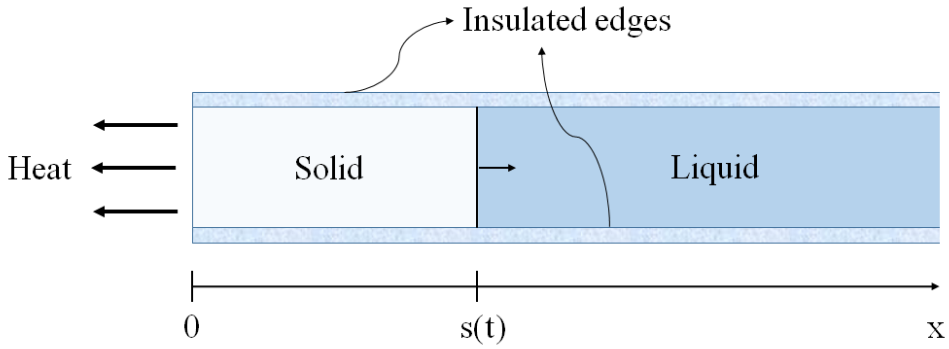

Source: Rocha *et al*. (2023b).

$$\rho c_{\mathrm{p,l}} \frac{\partial T_{\mathrm{l}}}{\partial t} = \frac{\partial}{\partial x}\left(k_{\mathrm{l}} \frac{\partial T_{\mathrm{l}}}{\partial x}\right) \tag{3}$$

$$\rho c_{\mathrm{p,s}} \frac{\partial T_{\mathrm{s}}}{\partial t} = \frac{\partial}{\partial x}\left(k_{\mathrm{s}} \frac{\partial T_{\mathrm{s}}}{\partial x}\right) \tag{4}$$

$$-k_{\mathrm{l}} \frac{\partial T_{\mathrm{l}}}{\partial x}\bigg|_{x=s(t)} + k_{\mathrm{s}} \frac{\partial T_{\mathrm{s}}}{\partial x}\bigg|_{x=s(t)} = \rho_{\mathrm{s}} L \frac{\partial s(t)}{\partial t} \tag{5}$$

$$T_{\mathrm{l}}(s(t),t) = T_{\mathrm{s}}(s(t),t) = T_{\mathrm{sl}} \tag{6}$$

where x is the phase-change direction, k is the thermal conductivity, T is the temperature, ρ is the density, c_{p} is the specific heat, t is time, and $s(t)$ is the position of the phase-change interface. The subscripts are: s for solid phase, l for liquid phase, and sl for solid-liquid interface. Although this class of problems is called by Stefan´s problem, a general solution of Eqs. 3-5 is kwon as Neumann´s solution, in reference to his work published in 1912. In the following decades, many phase-change works were developed considering the melting/solidification of pure metals and alloys as the motivation. The main incentive to investigate PCMs used in LTES systems can be attributed to the NASA´s effort to develop thermal control systems of space vehicles.

Until the mid-1960's, it was a common engineering practice to consider only conduction as the transport mechanism in phase-change problems, although the occurrence of convective fluid motion had already been recognized. At that time, feasible alternatives to include natural convection began to appear in the literature (Yen, 1966). In 1970, Szekely and Chhabra made one of the first attempts to quantitatively investigate the effect of natural convection on the solidification problem. They applied a convective heat transfer coefficient (h) at the solid-liquid interface, based on existing Nusselt numbers. In this way, the effect of natural convection was only considered at this position, while the remaining fluid was treated as motionless. The first term in the left-hand side of Eq. 5 is, then, replaced by $h(T_l - T_{sl})$. The authors compared the numerical results, considering limited transient conditions, to experimental ones and they found a good agreement for the solidification front. It was concluded that integrating the knowledge of natural convection to solidification problems might provide a better description of the process.

In 1978, experiments demonstrated conclusive evidences on the dominant role of natural convection in the melting of a solid around a heated cylinder (Sparrow *et al*., 1978) and around a vertical heated wall (Hale and Viskanta, 1978; Ramsey and Sparrow, 1978). Since there, some theoretical analyses were performed trying to incorporate the effects of natural convection by including the resolution of momentum equation, as accomplished by Okada and Ho and Viskanta, both in 1984. These two works treated the problem in dimensionless form, solving the stream and vorticity equations, a common practice at that time. Validation was done by comparing predictions with experimental data. Besides, they provided correlations to predict the melt fraction and the Nusselt number.

Most of the studies including the effects of natural convection adopted the traditional relation of the Boussinesq approximation, Eq. 7, where the density variation is only considered at the buoyancy term of the momentum equation. For the remaining terms, the density is taken as a constant, in order to reduce the computational effort. However, for water, Eq. 7 cannot be employed, since it exhibits a non-linear density-temperature relationship near its maximum density point, at $T = 3.98°C$ (Braga and Viskanta, 1992). In 1986, Ho and Chen numerically studied the melting of ice around a cylinder considering the density inversion of water near 4°C and its effect on natural convection. A relation between density and temperature, specifically for water, was considered, to allow the density variation only in the buoyancy term. The authors concluded that the density anomaly caused changes on the recirculation flow, which in turn, strongly affected the melting process.

$$\rho = \rho_{\mathrm{ref}}[1 - \beta(T - T_{\mathrm{ref}})] \tag{7}$$

where β is the thermal expansion coefficient and the subscript ref indicates a reference value. Another strategy that can simplify the natural convection and to skip the resolution of momentum equations is to consider an effective thermal conductivity (k_{ef}) for the liquid state that includes conduction and convection. Differently from applying convection at the interface, in this case, k_{ef} replaces k_{l} in Eqs. 3 and 5, keeping them unaltered. Nevertheless, the same Nusselt number (Nu) can be employed in both techniques, once this parameter is the ratio of heat transfer by convection to the heat transfer by pure conduction ($Nu = 1$), related by Eq. 8.

$$Nu = \frac{hX}{k_{\mathrm{l}}} = \frac{k_{\mathrm{ef}}}{k_{\mathrm{l}}} \tag{8}$$

where X is a characteristic length. As a disadvantage by using k_{ef}, it is not possible to track the correct position of the melting/solidification front, since only the heat conduction equation is implemented.

According to Jany and Bejan (1988), the melting process is governed by four regimes: (i) pure conduction, (ii) mixed conduction and convection (transition), (iii) natural convection, and (iv) shrinking solid. The first is characterized by high initial Nu that sharply drops to a minimum. In this stage, the melting front is nearly symmetric to the heated wall. In regime (ii) a slightly increase in Nu is observed, which can be attributed to an increase of convection currents. The

third regime presents an almost stationary Nu, explained by the dominance of the convection. Lastly, regime (iv) exhibits a decrease of Nu due to the shrinkage of the convective flow.

2.3. Numerical methods

The finite difference method (FDM) had been successfully employed up to the 1980's, but attention to the finite element method (FEM) started to grown as more complex geometries and coupled stress/thermal problems had arisen (Thomas *et al*., 1984). Regardless the discretization scheme, the classical Stefan formulation (Eqs. 3-5), with temperature as the dependent variable was usually adopted. In such cases, the position of the phase-change front has to be continuously tracked in order to allow the application of boundary conditions. Using fixed grids, i.e. discretizing the domain equally in space and time, may result the phase-change front to fall between two nodal points in a given time step, making its application not straightforward. Instead, deforming grids or coordinates transformation (Ho and Chen, 1986; Ho and Viskanta, 1984; Okada, 1984) was employed as an easier way to locate the phase-change front, but at the expenses of more complex numerical schemes. An illustration of the coordinate transformation is visualized in Figure 3.

Figure 3. a) Example of a physical domain; b) Discretized domain with coordinates transformation.

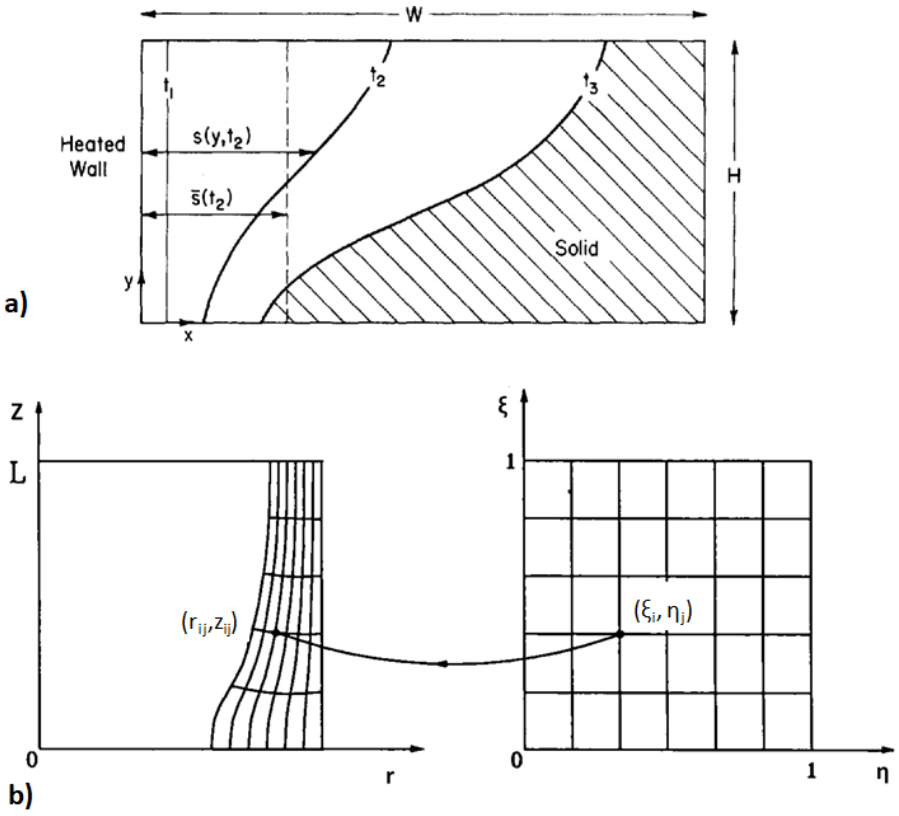

Source: a) Webb and Viskanta (1985); b) Prud'homme *et al*. (1993).

Another constraint adopting Stefan's formulation is that the phase-change should stand to a single temperature value, which is not the case for many PCMs that present a temperature range for solidification/melting. To overcome the above limitations, enthalpy formulations can be used for both cases. There are different solution strategies in this approach, such the apparent or equivalent heat capacity (Bonacina *et al*., 1973; Lewis and Roberts, 1987), and source-based methods. The latter was selected to be discussed due to the wider utilization. In this approach, the left-hand side of the energy conservation equation is rewritten in terms of the total enthalpy (H). The whole process is, then, governed by a single equation, Eq. 9, instead of three (Eqs. 3-5). The total enthalpy is the sum of sensible (h) and latent (ΔH) heats, as described in Eq. 10.

$$\frac{\partial \rho H}{\partial t} + \nabla.(H\rho u) = \nabla.(k\nabla T) \tag{9}$$

$$H = h + \Delta H \tag{10}$$

where u is the velocity vector. Moreover, the contribution of the latent heat is isolated in a source term (S_h), Eq. 11. Then, Eq. 9 is rewritten as Eq. 12.

$$S_{\mathrm{h}} = -\frac{\partial \rho \Delta H}{\partial t} = -L\frac{\partial \rho f}{\partial t} \tag{11}$$

$$\frac{\partial \rho h}{\partial t} + \nabla.(h\rho u) = \nabla.(k\nabla T) + S_{\mathrm{h}} \tag{12}$$

where f is the liquid fraction. Besides de advantages mentioned above, there are no boundary conditions to be satisfied at the phase-change front and, hence, no need to track it accurately. On the other hand, the enthalpy-based solutions, at that time, suffered from oscillatory behavior in case of small phase-change temperature ranges (Voller and Cross, 1981).

Although temperature-based or enthalpy-based schemes are independent of the discretization method, the finite volume method (FVM) started to become more popular than the FDM and FEM as the development of enthalpy formulations increased. In 1987, Voller *et al*. proposed a general numerical methodology to study convection/diffusion problems, with mushy or single point phase-changes. As the PCM turns from liquid to solid, the advection must vanishes, and vice-versa. In their study, besides analyzing exiting strategies to zero the velocities at the solidification front, they introduced a source term based on Darcy´s law, in momentum

equation, Eq. 13. This new proposal considered the phase-change region as a porous medium, whose porosity is a function of the liquid fraction.

$$\rho \frac{Du}{Dt} = \rho g - \nabla P + \mu \nabla^2 u + S_{\mathrm{u}} \tag{13}$$

where g is the gravitational acceleration, P is pressure, μ is the dynamic viscosity, and $\vec{S}_{\mathrm{u}}$ is the momentum source term. The algorithm was implemented with the finite volume method (control-volume formulation), as detailed by Patankar (1980). Test problems were solved and the predictions matched analytical and numerical results from the literature. According to the authors, the Darcy source correction performed better and was easier to implement than the other velocity corrections. In the same year, Voller and Prakash (1987) improved the Darcy source term by considering a porosity function (A) based on the Carman-Koseny equation. The new momentum source term took the form of Eq. 14, with A described in Eq. 15.

$$S_{\mathrm{u}} = -Au \tag{14}$$

$$A = C \frac{(1-\lambda)^2}{\lambda^3 + q} \tag{15}$$

where C is the porosity constant, which varies according to the problem, λ is the porosity, equal to the liquid fraction (f), and q is a small number, 0.001, to avoid division by zero. In the liquid region, i.e. f = 1, the source term becomes zero and the momentum equations are dominated by the other terms. However, in the mushy region, as the liquid fraction tends to zero, the source term predominates and Darcy law exerts greater influence on the momentum equation. For f = 0, the function A tends to a large value, forcing the velocity to approach zero. A test case was performed, being reported consistency with the previous study. Although the enthalpy-porosity formulation has been proposed to make physical significance for a mushy phase-change, according to the authors, it is also suitable for single temperature phase-change problems.

2.4. Performance improvement

In this section, different alternatives to improve LTES systems are presented, including the utilization of multiple PCMs, the adoption of fins, nano-particles, porous foams, as well as other non-convectional techniques. A few approaches specifically for shell-and-tube configurations are also discussed.

2.4.1. Cascaded PCMs

The utilization of different PCMs, with distinct melting temperatures, to improve the performance of LTES systems dates to the 1980's (Farid and Kanzawa, 1989). Subsequently works in the next decade (Adebiyi *et al*., 1996; Watanabe *et al*., 1993; Watanabe and Kanzawa, 1995; Zhen-Xiang and Mujumdar, 1995) reported a better performance using multiple PCMs, compared to systems with a single PCM. Besides, for shell-and-tube configurations, it turned to be a consensus that ordering the melting temperature in a decreasing order, in regards to the hotter heat transfer fluid (HTF) side, is the best option. In charging mode (melting), the hot HTF would flow, at first, through the PCM with the highest melting temperature, exiting at lower temperatures where the PCM has the lowest melting temperature. For discharging, the flow sense is reversed, but the temperature gradients between PCMs and HTF is kept the same as in charging process. This more uniform temperature difference leads to a better efficiency of the LTES unit.

From 2010 on, perpendicularly (Figure 4a) and circumferentially (Figure 4b) cascaded configurations appeared in the literature, beyond the already known axially arrangement (Figure 4c). These new investigations brought new insights. The first important point that emerged is that the best combination of cascaded PCMs can differ between melting and solidification processes. Secondly, regardless the arrangement, in practice, it is required solid walls to separate the different PCMs. For units axially and circumferentially cascaded, these walls act as fins and the effect of their inclusion could further improve the system performance. Therefore, optimal configurations can be explored through the combined use of multiple PCMs and fins. However, when cascading perpendicularly, the solid walls represent an additional thermal resistance, without the benefits of fins, once they are not linked to the heat source/sink. Therefore, the walls should not be neglected in simulations. This corroborates the findings by Elsanusi and Nsofor (2021) and Singh *et al*. (2020), that indicated a superior performance for axially cascaded PCMs, compared to perpendicularly ones. Nevertheless, more studies comparing these configurations are required, especially for axially versus circumferentially PCMs.

Figure 4. Arrangement of cascaded horizontal shell-and-tube: a) segmented along the tube diameter; b) segment along the circumference; c) segmented along the tube length.

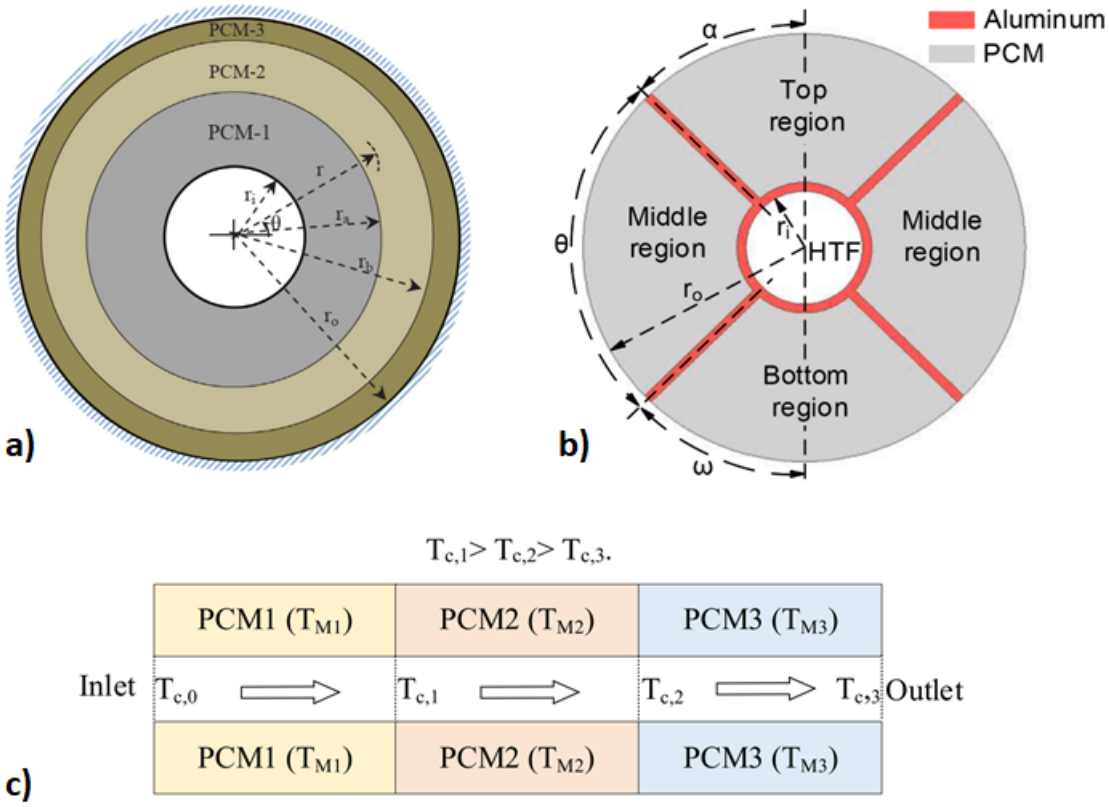

Source: a) adapted from Mahdi *et al*. (2020); b) adapted from Liu *et al*. (2021); c) Shen *et al*. (2022).

The above comments are valid for shell-and-tube configurations, where a HTF is subjected to a temperature gradient between the inlet and outlet. For cavities heated from an isothermal wall or subjected to a constant heat flux, only one work was found (Li *et al*., 2020). Hence, further investigations are recommended. Recently, Rocha *et al*. (2023a) suggested a novel configuration for a wire-on-tube condenser employing the concept of cascaded PCMs, that would be suitable for small refrigeration appliances, such as household refrigerators. This concept, presented in Figure 5, was based on the three flow regimes in which the refrigerant fluid is subjected.

Figure 5. Novel design of a wire-on-tube condenser with cascaded PCMs: a) Overview; b) Detail on a horizontal section.

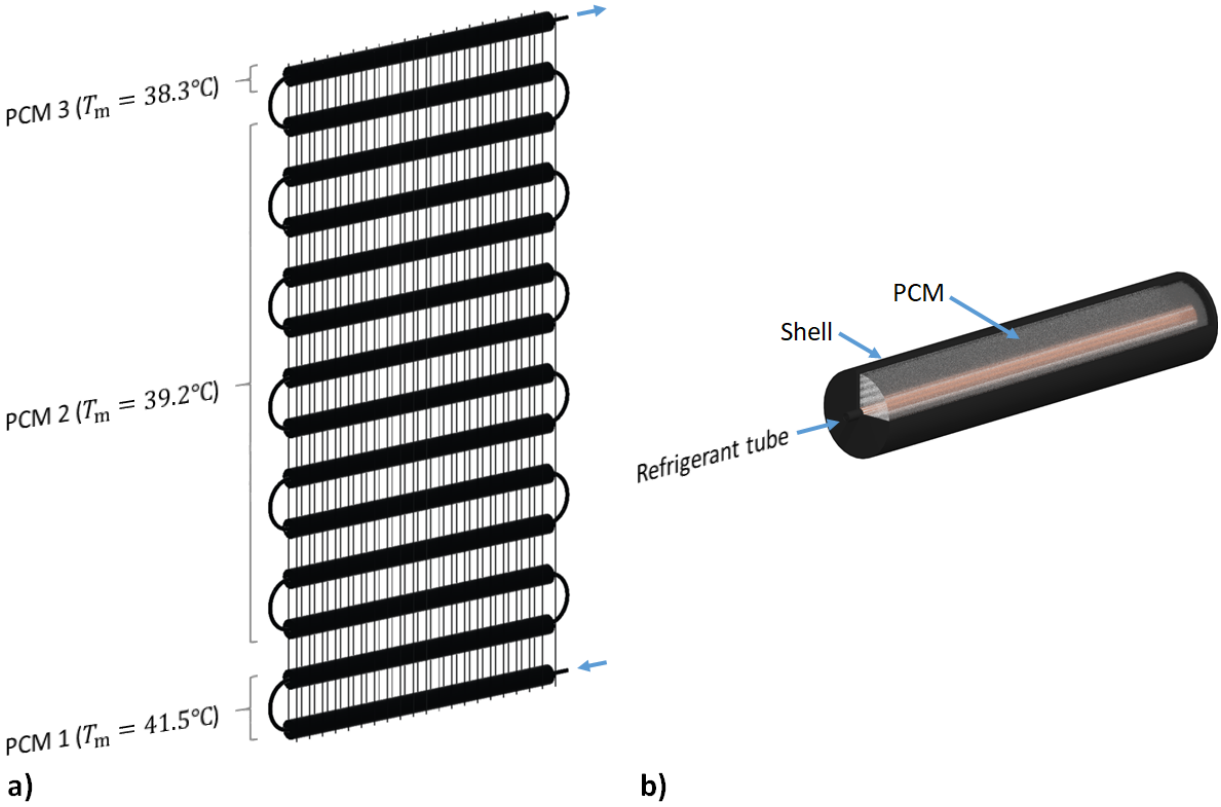

Source: Rocha *et al*. (2023a).

2.4.2. Fins, nanoparticles, and porous foams

A major drawback of PCMs, especially paraffins, is the low thermal conductivity, around 0.2 W/mK (Tian and Zhao, 2011), which implies in limited heat charge and discharge rates. One alternative to alleviate this limitation is to employ extended surfaces with good thermal conductivity. The usage of fins was already reported in 1977 by Humphries and Griggs as a way to improve the heat transfer between the container and the PCM. Since there, several investigations appeared in the literature. In 1998, Lacroix and Benmadda numerically investigated the melting of n-octadecane from a heated wall with vertically oriented fins. The authors concluded that the melting time could be minimized for an optimal distance between the fins. Subsequently, Ismail *et al*. (2000) reported a significant effect on the solidification time when altering the fin number, length, and aspect ratio, while fin thickness exerted little influence. In the past decade, the number of published studies investigating the utilization of fins significantly increased. Besides the traditional axial or radial finned configurations, novel arrangements were reported, as illustrated in Figure 6.

Figure 6. Sample of novel geometries investigated in the past decade: a) internal and external axial fins in a triplex-tube heat exchanger; b) bifurcated (snowflake) axial fins; c) helical fins.

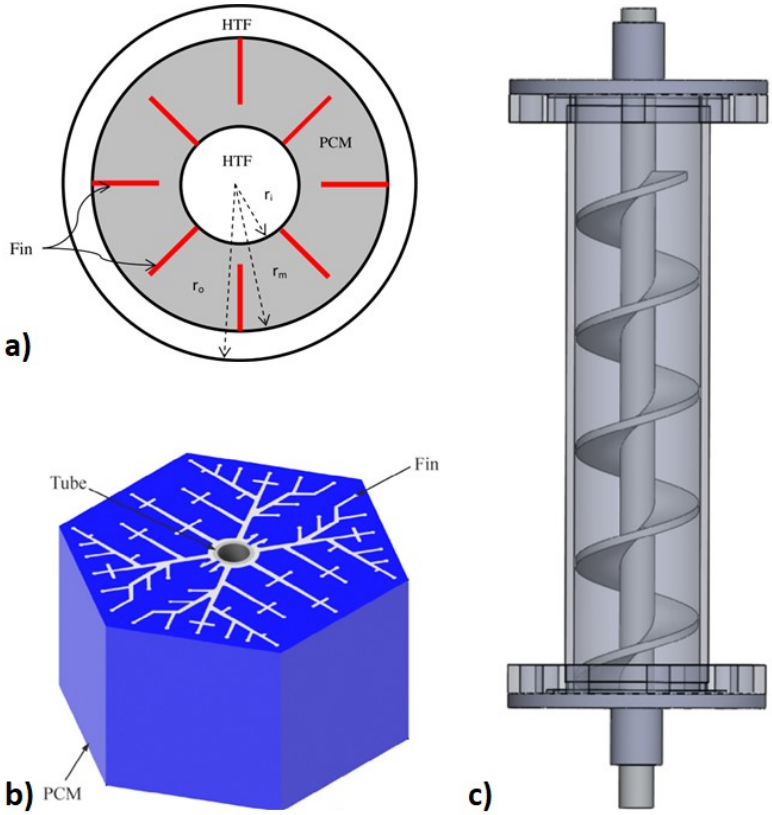

Source: a) adapted from Mat *et al*. (2013); b) adapted from Vogel and Johnson (2019); c) adapted from Rozenfeld *et al*. (2017).

For a given LTES system, e.g. horizontal shell-and-tube, there would exist fin arrangements that lead to the maximum performance, considering a fixed amount of PCM and fin material. Indeed, the majority of the published studies goes towards finding this best configuration, by proposing novel finned geometries. However, most of this knowledge are scattered in literature, being not possible to establish a direct comparison. If one wants to use this information to design a LTES system, it could get lost choosing one among the available options. Finding the optimal configuration, if it is possible, would require hardworking investigations employing optimization methods. Meanwhile, significant contributions can still be achieved through less complex alternatives, such comparing existing and/or novel geometries and, then, discarding those less efficient.

Another strategy to enhance the heat charge/discharge rates in phase-change problems is to disperse high conductivity particles into the PCM. This approach was investigated in 1977 by Siegel, who proposed a model to estimate the improvements in the heat transfer rate, when compared to the system without particles. Up to the 1990's the idea of mixing high conductivity

solids into HTFs had been restricted to conventional-sized particles, i.e. particles in the microscale or greater. In 1995, Choi and Eastman proposed the concept of nanofluids, in which metallic particles with sizes of about 10 nanometers were added into a HTF. According to the authors, the much larger surface area to volume ratio of nanoparticles is suitable to significantly improve the heat transfer capabilities and the stability of the suspension. To verify this new proposition, they employed an existing model (Hamilton and Crosser, 1962) to estimate the apparent thermal conductivity, developed for conventional-sized particles. Although not validated, the results confirmed the improvement on the thermal conductivity and on the heat transfer. Even if this work had not dealt with the application of LTES, the innovative idea of nanofluids proposed here is the origin of the so-called nanoparticles-enhanced PCMs (NePCMs). From 2007 on, NePCMs prevailed over conventional-sized enhanced PCMs. These new materials brought additional considerations, once other thermophysical properties, than the thermal conductivity, are influenced by the volumetric fraction of solid, being required models to estimate them. Similarly to what occurred with the utilization of fins, investigations with NePCMs significantly increased in the last decade.

Almost universally, the theoretical studies consider a reduction in the latent heat of a NePCM, compared to the pure PCM, because the nanoparticle does not contribute to the phase-change. This is taken into account once the material mass effectively changing phase is reduced, such that a linear relation (simple mixing) with the nanoparticle addition is used for calculation. However, this may not be always the case. In fact, in some circumstances, the latent heat of the NePCM can, even, be enhanced. This was reported by Colla *et al*. (2015), where the experimental measurements indicated an improvement for the NePCM latent heat. The authors removed the mass of nanoparticles dispersed in the PCM, but even doing so, the latent heat was still higher. This indicates that interactions between nanoparticles and PCMs may occur, requiring the development of specific relations to compute the latent heat of fusion. Besides, it is a consensus that the addition of nanoparticles increases the thermal conductivity and the viscosity of the PCM. This has different consequences in melting and solidification process. In the first case, except for the earliest stages, the heat transfer is dominated by natural convection, which is weakened by the addition of nanoparticles, due to the increased viscosity. In consequence, the melting time could raise if the shrinkage of convective motion supplants the improvement of thermal conductivity. In the second process, conduction often dominates the heat transfer and the solidification time is reduced as the content of nanoparticles is raised, due to the higher thermal conductivity.

A third strategy to overcome the low thermal conductivity of PCMs is to embed the PCM in a porous matrix with high thermal conductivity. Since the pioneering work attributed to Maxwell, in 1891, many investigations had dealt with heat conduction in porous matrices, without phase-change, as a way to improve the heat transfer characteristics. The first use of metal foams to improve LTES systems seems to have appeared in the 1960's with NASA (Bentilla *et al*., 1966). Similarly to the dispersed particles approach, a common task is to determine an apparent/effective thermal conductivity for the combined two-phase medium, i.e. PCM/porous matrix. For melting/solidification problems, this application appeared to become more relevant in the 1980´s. Subsequently, in the 2000's, there was an increased interest in using carbon materials. This could be related to the capacity to improve the performance of LTES systems, demonstrated by the first works, but it can also be an effect of the overall increase on the utilization of these nanomaterials, including in non-engineering applications. Nevertheless, the use of non-carbon matrices was also reported (Mesalhy *et al*., 2005). The utilization of carbon-based materials did not get the same attention from 2010 on. Despite the advantages of low density and excellent thermal stability, their properties are extremely sensitive to the synthesis process. Metals, on the other hand, possess well-defined properties, but have higher densities and can suffer from corrosiveness.

2.4.3. Non-conventional techniques

Besides the techniques described in Sections 2.4.1 and 2.4.2, other less traditional alternatives can improve the performance of LTES systems, such as rotating tubes, magnetic fields, ultrasounds, and others.

The experimental investigation on the effects of rotating surfaces on metals solidification dates to the 1980's (Vivès, 1988). However theoretical studies on the melting problem seems to have been addressed only in 1993, by Prud'homme *et al*.. The authors analyzed the melting of solids, with different Pr numbers, inside rotating cylinders. The results indicated that the existence of the secondary flow is important only near the moving wall, for high Re. Besides, for low Pr, melting was found to be insensitive to the rotation speed, while it was significant for moderate Pr. The investigations in this field became more noticeable in the past decade, where the number of published papers significantly grew. Kurnia and Sasmito (2018) revealed an improvement of both the melting and solidification processes with the introduction of small rotations, as visualized by the liquid fraction in Figure 7a. Besides, increasing the velocity from 0.1 rpm to 1 rpm conducted to a more uniformity, seen in Figure 7b.

Figure 7. Liquid fraction prediction with rotational speed: a) Over time; b) Distribution at t=30 minutes.

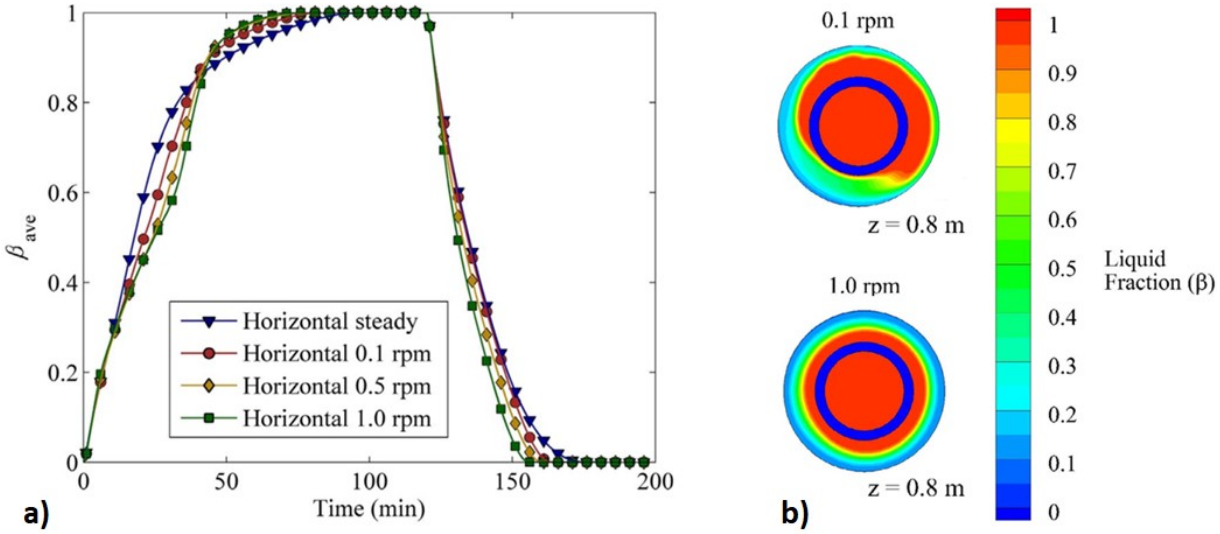

Source: adapted from Kurnia and Sasmito (2018).

Another non-conventional technique to enhance heat transfer is to employ an ultrasound (wall vibration) during the phase-change process. This approach was revealed useful in an experimental work from 1979 (Fairbanks, 1979), confirmed by a different experiment in 1990 (CHOI and HONG, 1990). Nevertheless, the first theoretical study to explore this feature was conducted in 1998, by Shiruanian *et al*., being reported an increase in the melting rate by 15%. Besides, for very high vibration frequencies, the liquid fraction approached that for the case without vibration. In the 2000's, Yang and Oh (2007, 2006) confirmed the viability of this method, where the melting assisted by ultrasound was about 2.3 times faster.

A third technique concerns the application of magnetic fields. Much of the first developments in phase-change problems were done considering the melting/solidification of metals as the motivation. This also holds for magnetic fields, whose capacity to affect the solidification is documented since the 1960's (Youdelis *et al*., 1964). However, it can be considered that the inspiration of employing Lorentz forces in NePCMs came, again, from the nanofluids. In such approach, a NePCMs containing magnetic particles is subjected to an external magnetic field. It seems that the first study focused on the application of magnetic fields for LTES purposes was published in 2017 (Kohyani *et al*., 2017). Therefore, there is a great opportunity for future investigations in this field. As a general trend from these previous works, it can be said that increasing the magnetic field weakens the natural convection, which causes the following effects: (i) increases the total melting time, (ii) reduces the total solidification time, (iii) turns the solid-liquid interface to be more uniform. Therefore, once Lorentz forces affect differently

the melting and solidification, it could be valuable to investigate the whole cycle, by turning the magnetic fields on and off during these processes. Besides the techniques discussed above, the investigation of melting assisted by electric field was also found (Selvakumar *et al*., 2021).

2.4.4. Alterations of shell-and-tube units

An arrangement often considered for a LTES system is the shell-and-tube configuration, with a HTF flowing in the inner tube and the PCM filling the annular region. In a review study published in 2010 (Agyenim *et al*., 2010), this configuration accounted for more than 70% among the analyzed works. For a horizontal position, several studies showed that eccentrically placing the inner tube at the bottom region could shorten the melting process. This can be explained by the higher intensity of natural convection currents acting at the upper region of the annulus, accelerating the melt at this location, while the bottom region suffers from the weak pure conduction. By placing the inner tube below the center, the influence area of natural convection raises, reducing the total melt time. When contrasting some of these studies, different absolute values of the eccentricity, 5 mm in Darzi *et al*. (2012) and 30 mm in Cao *et al*. (2018), provided an improvement of about the same magnitude, 65.5 versus 57%, respectively. Nevertheless, the quantities 5 mm or 30 mm do not give to the readers the idea of how much eccentric the system is, because tube and shell radii can differ between LTES units. Therefore, some authors defined a dimensionless factor, the eccentricity (ε), to overcome this problem. However, it was defined in different ways, being recommended to standardize this factor for future studies. Besides, it seems to exist an optimal eccentricity value, as demonstrated with the conjugated use of copper foams (Xu *et al*., 2021).

Other strategies concerning the geometry alteration of shell-and-tube units were found in the literature, such to incline the system, employing a helical configuration, and splitting the inner tube to multiple tubes. While experimental studies on the role of orientation were found in 1994 (Hasan, 1994a, 1994b), an increasing number of theoretical investigations was observed in the past decade. A result of such kind of work is illustrated in Figure 8. Comparing horizontal and vertical orientations, the first was found to be the best choice in four papers (M. S. Mahdi *et al*., 2020; Mahdi *et al*., 2019; Mehta *et al*., 2019; Seddegh *et al*., 2016), while the second was the best in one (Al Siyabi *et al*., 2019). Nevertheless, at the current stage, it cannot be generalized that horizontal is the best option, being required more comprehensive investigations. For solidification, one study reported that orientation did not play an important role. On the other hand, inclining the system and employing coiled configurations seems to be a good idea for melting, but further evidences are required for the solidification process.

Figure 8. a) Representation of vertical, horizontal, and coiled arrangements; b) melt fractions versus time for each geometry.

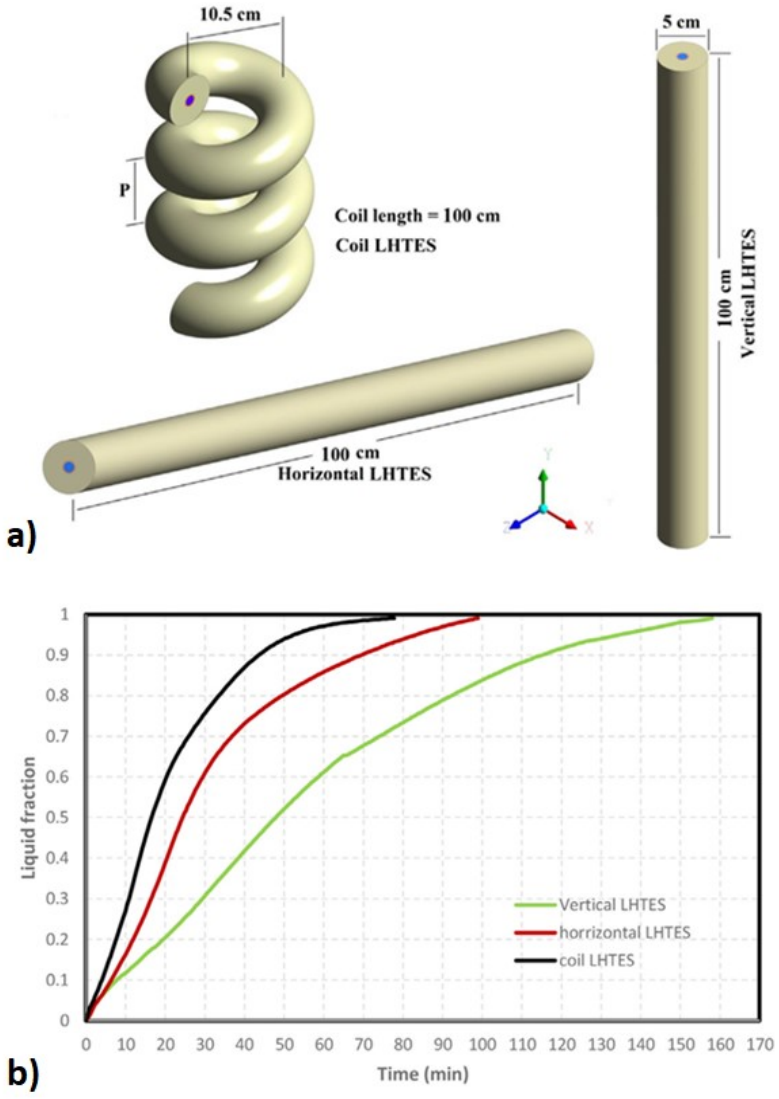

Source: adapted from Mahdi *et al*. (2020).

2.5. Porosity constant and PCM properties

A common characteristic of theoretical studies on LTES systems is to validate a mathematical model and explore it in different conditions to find the best scenarios. Nevertheless, it frequently happens that validation is carried out with a different PCM or in a completely different condition than that in which the model is to be used, probably due to the absence of available experiments. To illustrate the above-mentioned validation problem, Table 1 lists some numerical studies.

Table 1. A sample of numerical studies employing different systems and/or PCMs that those of validation.

Reference	System (model)	PCM (model)	Boussinesq approximation	System (validation)	PCM (validation)
(Chen and Fan, 2022)	Vertical shell-and-tube with radial fins	RT55	Yes	Vertical shell-and-tube	RT35
(Ye and Khodadadi, 2022)	Horizontal shell-and-tube with arrow fins	N-octadecane	Yes	Horizontal shell-and-tube	Lauric acid
(Haddad *et al*., 2021)	Trapezoidal cavity heated by a wavy wall	n-eicosane	Yes	Rectangular cavity heated by one side	Gallium
(Wang *et al*., 2021)	Finned plate heat exchanger	RT82	Yes	Rectangular (vertical) cavity heated by both lateral sides	Hydrated salt ($T_{\mathrm{m}} = 58.4℃$)
(Zhang *et al*., 2022)	Printed circuit heat exchanger with cascaded PCMs	3 PCMs enhanced with expanded graphite or 5 PCMs without it ($180℃ < T_{\mathrm{m}} < 318℃$)	Yes	Parallel slabs heat exchanger	Paraffin ($T_{\mathrm{m}} = 21.7℃$)
(Ghalambaz *et al*., 2021)	Horizontal shell-and-tube (double pass) with NePCMs	Capric acid enhanced with Copper and graphene oxide particles	Yes	Rectangular cavity heated by one side	Lead (Pb)
(Saeed *et al*., 2022)	Pear-shaped container with fins	N-octadecane enhanced with Al_2O_3 nanoparticles	Yes	Square cavity heated by one side (numerical)	Paraffin ($T_{\mathrm{m}} \approx 47℃$) enhanced with Al_2O_3 nanoparticles
(Ahmed *et al*., 2021)	Horizontal shell-and-tube with fins	N-octadecane enhanced with Al_2O_3 nanoparticles	Yes	Spherical capsule (constrained melting)	N-octadecane without particles
(Mourad *et al*., 2022)	Horizontal shell-and-tube with lobulus-shaped tube	Paraffin ($T_{\mathrm{m}} \approx 54℃$) enhanced with copper particles	Yes	Square cavity heated by one side (numerical)	Paraffin ($T_{\mathrm{m}} \approx 47℃$) enhanced with Al_2O_3 nanoparticles

Source: Rocha *et al*. (2023c).

The majority of models found in the literature are established on CFD codes that adopt the enthalpy-porosity approach (Voller and Prakash, 1987). In this scheme, the energy equation is written in an enthalpy formulation, while a source term is added at the momentum equation to handle the phase-change (mushy) region, considered a porous medium. Besides porosity, described by the liquid fraction, the source term also includes the porosity constant (C), being the recommended values from 10^4 to 10^7 (*ANSYS FLUENT User's Guide*, 2013), although higher values have also been reported. Kheirabadi and Groulx (2015) reported the dependency between this constant and the melting temperature range, recommending the verification with

other material properties. Nevertheless, the boundary conditions and the geometry also represent important factors in this discussion. In practice, after establishing all PCM properties, verifying grid and time step independency results, and other numerical parameters, the porosity constant is used as an "adjustment factor" to find the best accuracy, when simulation results are contrasted with experiments. It is quite common to find studies adopting $C = 10^5$ as a default value, without testing its influence on the results. Nevertheless, discussions on the proper value of C are available in the literature and investigations reporting its variation are becoming more frequent. As it could be expected, the best C value varies for different PCMs, as verified by contrasting the references of Shmueli *et al*. (2010) ($C = 10^8$ for RT27) and Marušić and Lončar (2020) ($C = 10^9$ for sodium nitrate), although the value of the porosity constant cannot be considered unique for a given PCM. Therefore, if the model is validated with another PCM, holding the porosity constant unaltered, significant deviations may be incurred in. Besides, large divergences on the best C value can also be noted for the same PCM, e.g. lauric acid, by comparing some studies in Table 2, although different assumptions were considered.

Table 2. Sample of papers reporting the alteration of the porosity constant (C) value for lauric acid melting.

Reference	**System**	**Boussinesq approximation**	***C* values**	**Best results**
(Fadl and Eames, 2019)	Rectangular cavity	?	10^5, 5×10^5, 10^6, 10^7 for horizontal and vertical orientations, plus 2×10^5 for horizontal.	For vertical orientation, $C = 5 \times 10^5$ performed best, while for horizontal, 2×10^5 was the best
(De Césaro Oliveski *et al*., 2021)	Rectangular cavity with fin	No	Non informed	$C = 10^{11}$
(Troxler *et al*., 2023)	Inclined rectangular cavity	Yes (one model) and no (another model)	10^4, 3×10^4, 5×10^4, 7×10^4, 10^5	$C = 10^5$ and 3×10^4 were the best for wall temperatures of 60°C and 70°C, respectively.

Source: Rocha *et al*. (2023c).

Still in Table 2, Fadl and Eames (2019) reported variations on the most suitable C value by just turning the system from vertical to horizontal oriented, while Troxler *et al*. (2023) found different values when changing the wall temperature. This findings indicate that, if the material properties and the other parameters are unaltered, the root cause for this behavior would be the intensity alteration of natural convection. Tian *et al*. (2020) also reported different C values when investigating the melting of lauric acid in non-finned (10^6) and finned (3×10^6) vertical enclosures. Therefore, it is inferred a dependency between the porosity constant and the

intensity of natural convection. This implies that a new condition should not present strong differences on the liquid PCM flow, compared to that of validation.

The necessity to adjust the porosity constant for new scenarios can be considered a limitation of the enthalpy-porosity method. Reichl *et al*. (2022) performed a comparison between two models to solve melting and solidification problems, both implemented in Fluent software. The first used the enthalpy-porosity scheme by turning on the melting/solidification mode. The second was developed considering the apparent heat capacity (AHC) method (melting/solidification mode off), in which the phase-change is included by modifying the specific heat curve to include the latent heat of melting/solidification. With the AHC, the porosity constant, included on the source term of the momentum equation, is not needed, but a very high viscosity value must be inputted to the solid PCM, in order to force its velocity approach zero. According to the authors, a continuous viscosity function should be used for the entire temperature range to allow stable results. It was concluded that both methods provide accurate results, but the AHC was recommenced due to its independency with the porosity constant, although an artificial viscosity needs to be used.

It could be suggested that, considering all temperature-dependent properties and accounting for the volumetric expansion of the PCM by the volume of fluid (VOF) model, the dependency of the porosity constant value with the natural convection intensity would not exist. Based on the literature published so far, the authors cannot affirm so, but this idea needs to be verified. However, the VOF model has been seldom adopted due to its significantly higher computational effort. Therefore, the problem of the dependency between the porosity constant and the natural convection intensity still would exist in practice.

Another comment concerning Tables 1 and 2 is that several investigations adopt the Boussinesq approximation, Eq. 7, to reduce the simulation time, keeping an acceptable precision, as demonstrated in some investigations (Reichl *et al*., 2022; Vogel and Thess, 2019). This benefit can be achieved once the density appearing in all governing equations is assumed constant, while only the buoyancy term of the momentum equation considers its variation, although indirectly. One may be in doubt in what value to consider as reference for density. Some authors argue that, considering the stored energy, the mean density between the solid and liquid PCM is a more suitable choice. On the other hand, from a hydrodynamics point of view, the density value at the liquid state could be the most suitable option, once the melting process is dominated by natural convection (Vogel and Thess, 2019). Recently, Troxler *et al*. (2023) recommended to use different values of density for the liquid and solid PCM. However, this choice lead to

longer simulation times. The other PCM properties should also be selected with caution, since they can directly affect the results accuracy. Table 3 compiles the thermophysical properties of the lauric acid, for different sources.

Table 3. Thermophysical properties of lauric acid found in different references.

Reference	T_m [°C]	L [kJ/kg]	c_p [J/(kg.K)]	ρ [kg/m³]	k [W/(m.K)]	μ [Pa.s]	β [1/K]
(Mahdi *et al*., 2021)	44.5 (solidus); 48.3 (liquidus).	178.78	2200	857	0.157	0.0067	0.0006
(Yuan *et al*., 2016)	44.2 (melting)	173.8	2300 (liquid)	862.9 (60°C), 856 (70°C), 848.3 (80°C),	0.147 (liquid)	0.005336 (60°C), 0.004269 (70°C), 0.003469 (80°C).	0.000615
(Cao *et al*., 2018)	44.2	174.9 (melting); 173.4 (solidification)	2300 (liquid)	862.9 (solid); 856 (liquid at 70°C).	0.147 (liquid)	-	0.000615
(Kalapala and Devanuri, 2020)	43.5 (solidus); 50.0 (liquidus).	156.8	1390 (solid); 1570 (liquid).	-	-	-	-
(Shokouhmand and Kamkari, 2013)	43.5 (solidus); 48.2 (liquidus).	187.2	2180 (solid); 2390 (liquid).	940 (solid); 885 (liquid).	0.16 (solid); 0.14 (liquid).	-	-
(Liu and Groulx, 2014)	44	182	2400 (solid); 2000 (liquid).	950 (solid at 20°C); 873 (liquid at 45°C).	0.150 (solid); 0.148 (liquid).	0.008 (at ~T_m)	-
(Shaker *et al*., 2021)	40.5 (solidus); 42.5 (liquidus).	129.5	2180 (solid); 2390 (liquid).	940 (solid); 885 (liquid).	0.16 (solid); 0.14 (liquid).	0.005930	0.00083
(Li *et al*., 2022)	43 (solidus); 44 (liquidus).	143.8	2300	848.3	0.147	0.003469	0.000615

Source: Rocha *et al*. (2023c).

Although the claimed purity of lauric acid used in the works of Table 3 is, generally, 99%, there is a significant variation in its reported properties. Therefore, a proper combination of the C constant with the thermophysical properties must be done. The adequacy of this choice needs to be confirmed by comparing simulating and experimental results, considering similar conditions and the same PCM.

2.6. Effective thermal conductivity

The effective thermal conductivity approach is an alternative to avoid the high computational effort required to solve the coupled equations of mass, momentum, and energy. With this approach, a pure conduction model considers both conduction and convection mechanisms by boosting the thermal conductivity of the medium (Rocha *et al*., 2023b). Therefore, considerable time savings can be achieved by solving only the energy equation. For instance, Tehrani *et al*. (2019) reported a 3000 fold reduction on the simulation time for the melting of PCMs in a vertical shell-and-tube, while a maximum difference of 8.6% was noted for the melting time, compared to the full CFD model. A further advantage of using k_{ef} in phase-change problems is that, in several cases, the solution domain drops in one dimension, i.e. a 3D geometry can be modelled with a 2D domain, while a 2D is reduced to a 1D. This occurs due to the symmetric and parabolic nature of the conduction mechanism, differently to what occurs with natural convection. On the other hand, this approach is useful only in terms of average values, such heat transfer rates, stored energy, and liquid fraction, since it does not capture the actual temperature field nor the phase-change interface. It occurs because the conduction mechanism leads the melted region to be symmetric, which is not the case in real situations involving natural convection. Nevertheless, using the effective thermal conductivity may be of particular interest when the PCM heat exchanger is only one component in a global system, e.g. solar power plants, batteries, buildings, Rankine and refrigeration cycles.

For a horizontal annulus, this concept was proposed in 1931 by Beckmann, who experimentally investigated the natural convection of air, hydrogen, and carbon dioxide. Since there, other proposals appeared to estimate k_{ef} for this configuration, where both tubes are isothermal, maintained at different temperatures. Raithby and Rollands (1975) developed a theory to investigate the natural convection in several configurations, among them, concentric cylinders. Although their correlation (Eq. 16 - Table 4) was proposed for the annular region, it is recommended when curvature effects can be neglected, situation valid for $\mathrm{Ra_D} \gtrsim 10^5$, based on an isolated (inner or outer) cylinder. The authors also outlined the procedure to incorporate curvature effects, while the algebraic manipulation was found in the work of Atayilmaz (2011) (Eq. 17 - Table 4). Subsequently, a more complex (and accurate) correlation was developed by Kuehn and Goldstein (1976), who theoretically investigated the natural convection at the annular region, including eccentricity effects. Besides the proposed correlation to estimate k_{ef}, the authors identified that, for large diameter ratios, the heat transfer coefficient approaches that of an immersed infinite cylinder. For their specific conditions, to reach 95% of the infinite

cylinder solution, $D_o/D_i > 360$ is required for $Ra_{D_i} = 10^7$, while $D_o/D_i > 700$ is needed for $Ra_{D_i} = 0.1$. In another work, Hessami *et al*. (1985) performed experiments and simulations with air, glycerin, and mercury in order to cover a wide range of Pr. Besides, the authors considered a higher value of $D_o/D_i = 11.4$, as an extension of the experimental data available in the literature at that time. They tried to correlate all data for the convective coefficient at the inner tube with the form $Nu_{D_i} = C\ Pr^m\ {Gr_{D_i}}^n$, but reported unsatisfactory results. A better alternative proposed for both, the infinity cylinder and the annulus, took the form of Eq. 18. (Table 4). The authors also reported that, for their conditions, 97.7% of the infinite cylinder solution was obtained for $D_o/D_i = 10$. Several other correlations with the traditional form $C\ {Ra_b}^n$ or that reported by Hollman (1986), Eq. 19 (Table 4), are available in the literature. The Rayleigh number (Ra), used in these correlations is defined in Eq. 21.

Table 4. Correlations to estimate the effective thermal conductivity in a circular annulus, without phase-change.

Ref.	$\mathbf{Nu} = \frac{\boldsymbol{hX}}{\boldsymbol{k}} = \frac{\boldsymbol{k_{ef}}}{\boldsymbol{k}} =$	**Constants**	**Eq.**
(Raithby and Hollands, 1975)	$C\left[\left(\frac{Pr}{Pr+m}\right)\left(\frac{[\ln(D_o/D_i)]^4}{b^3\left({D_o}^{-3/5}+{D_i}^{-3/5}\right)^5}\right)Ra_b\right]^{1/4}$	$C = 0.386$ $m = 0.861$	(16)
(Raithby and Hollands, 1975) written by (Atayilmaz, 2011)	$\frac{\ln(D_o/D_i)}{\ln\left[1+2/\left(C\left(\frac{Pr}{Pr+m}Ra_{D_i}\right)^{1/4}\right)\right]}\frac{T_i-T_{avg}}{T_i-T_o}$	$C = 0.386$ $m = 0.861$	(17)
(Hessami *et al*., 1985)	$C\left[\frac{(D_o/D_i)-1}{D_o/D_i}\right]^m\ \left(\frac{Pr}{Pr+n}Ra_{D_i}\right)^{1/4}$	$C = 0.53$ $m = 0.25$ $n = 0.952$	(18)
(Holman, 1986)	$C\ {Ra_b}^n\left(\frac{X}{b}\right)^m$	-	(19)
(Teertstra *et al*., 2005)	$1+\frac{\ln(D_o/D_i)}{2\pi}\left\{\left[\frac{1.028\ F\ {Ra_{P_i}}^{1/4}}{\left(1+\left(\frac{D_i}{D_o}\right)^{3/5}\right)^{5/4}}\right]^{-2}+\left[\frac{1}{720\pi^4}\ \frac{\left(\frac{D_o}{D_i}-1\right)^3}{\left(1+\frac{D_o}{D_i}\right)}\right]^{-2}\right\}^{-1/2}$ where $F = \frac{0.67}{[1+(0.5/Pr)^{9/16}]^{4/9}}$ and $P_i = \pi D_i$	Not needed	(20)

Source: the author.

$$\mathrm{Ra} = \frac{g\beta\left(T_{\mathrm{ref},1} - T_{\mathrm{ref},2}\right)X^3}{\alpha\nu} \tag{21}$$

where ν is the kinematic viscosity and $\left(T_{\mathrm{ref},1} - T_{\mathrm{ref},2}\right)$ is the driving temperature. Teertstra and Yovanovich (1998) performed a literature review on existing correlations that predict the effective thermal conductivity for the horizontal circular annulus. They identified three regions for this kind of problem, as shown in Figure 9: (i) the conductive limit, where pure conduction dominates and Nu is only a function of $D_\mathrm{o}/D_\mathrm{i}$; (ii) the transition, marked by a balanced contribution of conduction and convection, with Nu as a function of $D_\mathrm{o}/D_\mathrm{i}$ and Ra; (iii) the boundary layer limit, characterized by a stronger influence of Ra rather than $D_\mathrm{o}/D_\mathrm{i}$. The authors assessed the accuracy of several correlations and concluded that, among the candidates, Kuehn and Goldstein (1976) was the only model recommended for the transition region. Therefore, caution was advised when selecting a predictor for this region. Subsequently, Teertstra *et al*. (2005) developed an analytical model that combined the asymptotic solutions for the three regions of Figure 9, in order to derive a single correlation, Eq. 20 (Table 4). The authors verified the accuracy of their correlation against experimental datasets from the literature, being reported maximum root mean square error of 6%. Usually, the applicability of the equations in Table 4 spans a large range of Ra and Pr. However, for specific recommendations, readers are referred to the respective papers.

Figure 9. Characteristic regions of the natural convection problem in a horizontal annulus.

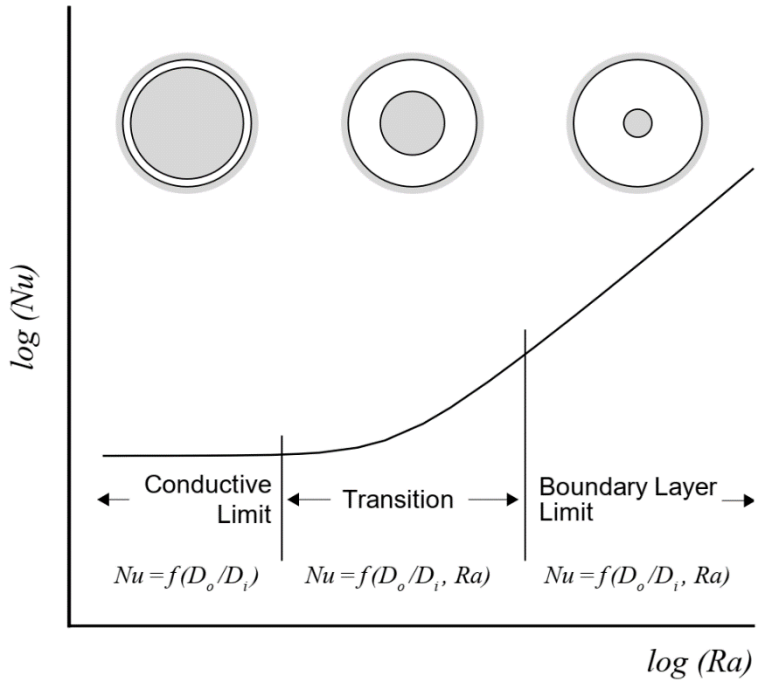

Source: Teertstra and Yovanovch (1998).

In 1967, Boger and Westwater suggested to use the same idea to the melting and solidification of water. They investigated if correlations developed for steady-steady conditions would also be suitable for the transient conditions of phase-change problems. A few years later, studies concerning the melting of PCMs began to appear, adapting the coefficients of $C\ \mathrm{Ra_b}^n$ and Eq. 19 for different configurations, such as vertical (Farid *et al*., 1989; Farid and Mohamed, 1987) and horizontal (Hirata and Nishida, 1989) cylinders, spheres (Amin *et al*., 2014; Gao *et al*., 2019), rectangular enclosures (Farid and Husian, 1990; Souayfane *et al*., 2018), and vertical shell-and-tube systems (Michels and Pitz-Paal, 2007; Mostafavi Tehrani *et al*., 2019). The majority of these correlations were developed for the dominant natural convection regime, the third of Figure 9. However, the melting of PCMs exhibits a fourth regime, characterized by a decrease of Nu, where the correlation of the previous region does not apply, as demonstrated by Jany and Bejan (1988). Therefore, it is recommended to investigate the applicability of such prediction methods whenever the fourth regime presents a significant duration. For the melting of a PCM inside a sphere, Gao *et al*. (2019) indicated that the transition to the fourth regime is anticipated for higher Ra, calculated with the sphere radius as the characteristic length, i.e. constant Ra.

Some correlations are also available for horizontal shell-and-tube units, as presented in Table 3.5. This geometry was favored since it is the configuration for the present investigation. Other studies adopting the equations presented in Table 5 were also found in the literature (Bechiri and Mansouri, 2015; Shakrina *et al*., 2022).

Table 5. Correlations to estimate the effective thermal conductivity in a horizontal shell-and-tube, considering phase-change.

Ref.	$\mathbf{Nu} = \frac{\boldsymbol{hX}}{\boldsymbol{k}} = \frac{\boldsymbol{k_{ef}}}{\boldsymbol{k}} =$	**PCM or Pr range**	**Boundary conditions or Ra range**	**Eq.**
(Lacroix, 1993)	$0.099\ \mathrm{Ra_{R_i}}^{0.25}$	n-octadecane	Forced convection with water	(22)
(El Qarnia, 2009)	$C\ \mathrm{Ra_b}^{0.25}\left(\frac{b}{R_o - R_i}\right)^{0.8}$ $\begin{cases} C = 0.24, & \text{for } T_{HTF,in} \leq 310.7\ \mathrm{K} \\ C = 0.18, & \text{for } 310.7\ \mathrm{K} < T_{HTF,in} \leq 320.7\ \mathrm{K} \\ C = 0.16, & \text{for } T_{HTF,in} > 310.7\ \mathrm{K} \end{cases}$	n-octadecane	Forced convection with water	(23)
(Adine and El Qarnia, 2009)	$C\ \mathrm{Ra}^{0.25}$	n-octadecane	Forced convection with water	(24)

	$\begin{cases} C = 0.08, & \text{for } T_{\text{HTF,in}} \leq 310.7 \text{ K} \\ C = 0.18, & \text{for } 310.7 \text{ K} < T_{\text{HTF,in}} \leq 320.7 \text{ K} \\ C = 0.16, & \text{for } T_{\text{HTF,in}} > 310.7 \text{ K} \end{cases}$ OBS: the characteristic length scale was not provided.			
(Wang *et al*., 2013)	$0.099\ \text{Ra}_{\text{R}_\text{i}}{}^{n}$ $\begin{cases} n = 0.26, & \text{for } T_{\text{HTF,in}} \leq 310.7 \text{ K} \\ n = 0.24, & \text{for } 310.7 \text{ K} < T_{\text{HTF,in}} \leq 320.7 \text{ K} \\ n = 0.22, & \text{for } T_{\text{HTF,in}} > 310.7 \text{ K} \end{cases}$	n-octadecane	Forced convection with water	(25)

Source: the author.

Although a few equations are available for horizontal shell-and-tube systems, as presented in Table 5, it should be highlighted that, El Qarnia (2009), Adine and El Qarnia (2009), and Wang *et al*. (2013) fitted the coefficients of their equations from the same experimental dataset of Lacroix (1993). Therefore, Eqs. 22-25 are not completely independent and the verification on the suitability to use them for different conditions, as well as the development of new correlations, are highly encouraged. The same comment concerning the validity of such predictors only for the regime of natural convection dominance applies. Besides, the development of the correlations and validation of the models of all works in Table 5 were done considering the inlet and outlet temperatures of the HTF. By doing so, it is not possible to properly assess the content of latent heat that has been stored in the PCM, which is mainly accounted through the liquid fraction. Related to that is the methodology to extract the appropriate liquid layer thickness from an asymmetric melted shape, which was not discussed in these investigations.

2.7. Concluding remarks from the literature review

It was noted that a comprehensive study evaluating the impact of altering the thermophysical properties of PCMs in a physically meaningful manner remains absent in the existing literature. Many references merely report random variations (Zeneli *et al*., 2021), without delving into the systematic effects of adjusting these properties. Moreover, while Troxler *et al*. (2023) made an attempt to combine density with porosity constant, various other properties exhibit significant disparities across different references. Furthermore, the synergy between selecting appropriate PCM properties and setting the porosity constant value remains a relatively unexplored territory. Lastly, there is a scarcity of research addressing the implications of validating a model for a specific configuration and subsequently employing it in different geometries, while maintaining the original set of variables. This investigation is especially pertinent as significant errors can potentially arise when utilizing a simulation model under conditions differing from

those used for validation. Therefore, the present investigation seeks to bridge these aforementioned research opportunities, with particular emphasis on the latter, which merits thorough discussion given its potential to impact the accuracy and applicability of the simulation model in diverse scenarios.

The second topic concerns the availability of correlations to predict the effective thermal conductivity for horizontal shell-and-tube heat exchangers employed in LTES systems. This geometry was selected for a deeper discussion since it is the choice of the present work. As mentioned, the available predictors were mainly developed for the region of natural convection dominance, regime (iii). However, the melting process possess a fourth regime, of shrinkage of natural convection, where the same Nu relation is not applicable. Besides, all the available correlations for this geometry were based on the same experimental dataset, which was not able to quantify the energy stored in the PCM. Therefore, there is a necessity to verify the applicability of the existing correlations for different operational conditions, to assure that a simplified model is able to predict the liquid fraction. In this sense, the second set of contributions of the present work are: (i) to verify the possibility to use Eqs. 22-25 for other conditions in a horizontal shell-and-tube unit; and (ii) to establish a methodology to calculate the effective thermal conductivity with the appropriate average radius of the solid/liquid interface.

3. METHODOLOGY

This chapter introduces two mathematical models for simulating the melting of a PCM. A full CFD model is described in subsection 3.1, aiming to investigate the role of the porosity constant and PCM thermophysical properties. In subsection 3.2, a simplified model is developed to verify the accuracy of the liquid fraction prediction compared to the CFD model and to experimental results from the literature, as well as to assess the applicability of existing correlations to estimate the effective thermal conductivity.

3.1. CFD model

The description of the CFD model initiates stablishing the physical domain, followed by the mathematical formulation, numerical implementation, and verification of mesh and time step.

3.1.1. Physical domain

In this section, two distinct reference configurations were employed. The first configuration involves a rectangular cavity measuring 120 mm in length and 50 mm in height, as depicted in Figure 10a. In this setup, the bottom wall was maintained at a constant temperature of 70°C, while the remaining walls were treated as perfectly insulated, ensuring adiabatic conditions. The initial temperature of the PCM was set at 25°C. This particular configuration corresponds to the scenario with an inclination angle of 0°, as established by Kamkari *et al*. (2014). The second reference configuration represents a shell-and-tube unit, characterized by an inner tube with an outer diameter of 40 mm and an outer tube with an inner diameter of 80 mm, as illustrated in Figure 10b. In this configuration, the inner tube serves as the heated wall, maintained at a temperature of 80°C, while the shell is assumed to be adiabatic. The initial temperature of the PCM in this case was set at 20°C, in accordance with the experimental setup by Yuan *et al*. (2016). Throughout this study, lauric acid is adopted as the PCM, and its thermophysical properties for the reference cases 1 and 2 are detailed in Table 6. It is worth noting that, the properties from Kamkari *et al*. (2014) were originally derived from a prior work of the authors (Shokouhmand and Kamkari, 2013), which includes distinct values for the liquid and solid phases of the PCM. However, specific information regarding viscosity and the coefficient of thermal expansion was not provided. For case 1, it was assumed the specific heat, density, and thermal conductivity as the average values between the liquid and solid phases, while the values for viscosity and the coefficient of thermal expansion were obtained from Yuan *et al*. (2016).

Figure 10. Physical domains under investigation: a) Case 1 – rectangular cavity; b) Case 2 – shell-and-tube unit.

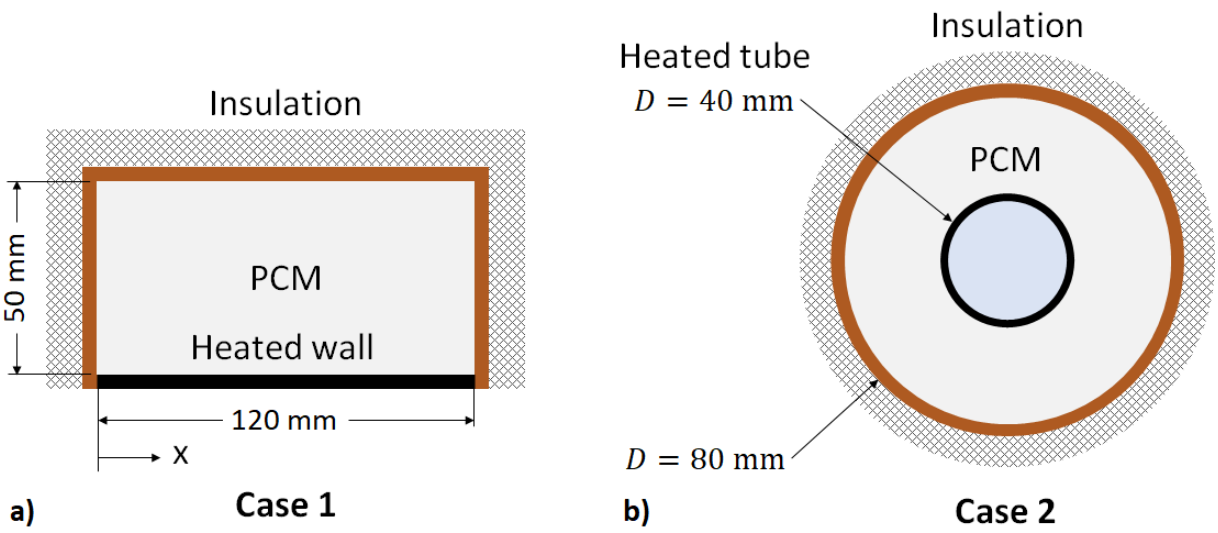

Source: Rocha *et al*. (2023c).

Table 6. Thermophysical properties of lauric acid for cases 1 and 2.

Reference	T_m [°C]	L [kJ/kg]	c_p [J/(kg.K)]	ρ [kg/m³]	k [W/(m.K)]	μ [Pa.s]	β [1/K]
Case 1 (Shokouhmand and Kamkari, 2013)	43.5 - 48.2	187.2	2285*	912.5*	0.15*	0.005336**	0.000615**
Case 2 (Yuan *et al*., 2016)	43.5***	173.8	2300	862.9	0.147	0.003469	0.000615

* Average of solid and liquid values.
** From Yuan *et al*. (2016).

***The value of Yuan *et al*. (2016) is 44.2. Nevertheless, 43.5 demonstrated to be a best choice, as discussed in section 4.1.3.

Source: Rocha *et al*. (2023c).

3.1.2. Mathematical formulation

The full model of melting/solidification is based on the enthalpy-porosity scheme (Voller and Prakash, 1987), which solves the mass, momentum, and energy conservation equations, Eqs. 26-28, respectively. Furthermore, the present model considers the following assumptions: (i) the liquid PCM behaves as a Newtonian fluid, (ii) the flow of the liquid PCM is laminar and incompressible, (iii) thermophysical properties are constant, (iv) contact thermal resistance of the solid PCM with the tube wall is negligible, (v) heat conduction through the axial direction of the tubes is negligible, and (vi) Boussinesq approximation is valid, i.e. the volumetric thermal expansion is neglected.

$$\nabla \cdot \vec{u} = 0 \tag{26}$$

$$\frac{\partial}{\partial t}(\rho\vec{u}) + \nabla \cdot (\rho\vec{u}\vec{u}) = \rho\vec{g}\beta(T - T_{\text{ref}}) - \nabla P + \mu\nabla^2\vec{u} + \vec{S}_{\text{u}} \tag{27}$$

$$\frac{\partial(\rho H)}{\partial t} + \nabla \cdot (\rho H\vec{u}) = \nabla \cdot (k\nabla T) \tag{28}$$

where the gradient operator is given by Eqs. 29 and 30 for Cartesian and cylindrical coordinates, respectively. Concerning the energy equation, the total enthalpy (H) is split in sensible (h) and latent heat (ΔH) terms, as indicated by Eq. 31.

$$\nabla = i\frac{\partial}{\partial x} + j\frac{\partial}{\partial y} + k\frac{\partial}{\partial z} \tag{29}$$

$$\nabla = e_{\text{r}}\frac{\partial}{\partial r} + e_{\theta}\frac{1}{r}\frac{\partial}{\partial \theta} + k\frac{\partial}{\partial z} \tag{30}$$

$$H = h + \Delta H \tag{31a}$$

$$h = h_{\text{ref}} + \int_{T_{\text{ref}}}^{T} c_{\text{p}}\, dT \tag{31b}$$

$$\Delta H = fL \tag{31c}$$

Where i, j, k, e_{r}, and e_{θ} are unitary vectors normal to their respective directions. A linear relation between enthalpy and temperature is assumed at the mushy region, such that the liquid fraction can be recovered from the temperature field, and vice-versa, according to Eq. 32.

$$f = \begin{cases} 0, & \text{if } T < T_{\text{s}} \\ \dfrac{T - T_{\text{s}}}{T_{\text{l}} - T_{\text{s}}}, & \text{if } T_{\text{s}} \leq T \leq T_{\text{l}} \\ 1, & \text{if } T > T_{\text{l}} \end{cases} \tag{32}$$

where T_{s} and T_{l} are the solidus and liquidus temperatures, respectively. The initial and boundary conditions for this work are as follows:

- The no-slip condition imply in zero velocity at the walls, i.e. $\vec{u} = 0$;
- At the heated walls, the temperature assumes the prescribed wall temperature, i.e. $T = T_{\mathrm{W}}$;
- At the insulated walls, adiabatic conditions apply, i.e. $\frac{\partial T}{\partial x} = \frac{\partial T}{\partial y} = \frac{\partial T}{\partial r} = 0$;
- The initial condition is a uniformly distributed temperature, i.e. at $t = 0$, $T = T_{\mathrm{ini}}$.

3.1.3. Numerical implementation

The mathematical model was discretized with FVM and solved with ANSYS® Fluent 17. A pressure-based solver was employed with PISO as the pressure-velocity coupling. Second order central differences was employed (default of Fluent) as the interpolation function for the diffusive terms in the energy equation, while second order upwind was used to interpolate the convective terms in momentum and energy equations. Discretization of pressure and time were done with PRESTO! and first order implicit schemes, respectively. Concerning the under-relaxation factors, 0.3, 0.7, 0.9, and 1 were chosen for pressure, momentum, liquid fraction update, and energy, respectively. Iterations at each time step were terminated when the residuals for the continuity, momentum, and energy equations fell below 10^{-3}, 10^{-3}, and 10^{-6}, respectively, although, continuity was found to be the constraint.

Since both cases are symmetric, only half of the domain could be solved. However, the experiments of Kamkari *et al.*(2014) showed a non-symmetric pattern of the melted regions in some time intervals. Therefore, it was decided to simulate the whole domain in case 1. For the shell-and-tube unit (case 2), only half of the domain was simulated. This choice was based on the experimental visualization reported by Cao *et al*. (2018), who performed investigations on the melt of lauric acid in a shell-and-tube unit.

3.1.4. Mesh and time step verification

For both cases, structured grids with quadrilateral elements were adopted. The mesh sensitivity analysis was carried out with the grid convergence index (GCI) method (Celik *et al*., 2008), which represents the uncertainty due to the numerical discretization. It is expressed by Eq. 33.

$$CGI = \frac{1.25 e_{\mathrm{a}}}{{r_{21}}^{p} - 1} \tag{33a}$$

$$e_{\mathrm{a}} = \left| \frac{\varphi_1 - \varphi_2}{\varphi_1} \right| \tag{33b}$$

$$p = \frac{|\ln|\varepsilon_{32}/\varepsilon_{21}| + q|}{\ln(r_{21})} \tag{33c}$$

$$q = \ln\left(\frac{{r_{21}}^p - s}{{r_{32}}^p - s}\right) \tag{33d}$$

$$s = 1 \cdot sgn(\varepsilon_{32}/\varepsilon_{21}) \tag{33e}$$

where $\varepsilon_{32} = \varphi_3 - \varphi_2$, $\varepsilon_{21} = \varphi_2 - \varphi_1$, φ_{k} is the solution (liquid fraction) on the k$^{\mathrm{th}}$ grid, and r is the grid refinement ratio. The function sgn on Eq. 33e assumes the values of -1, 0, or 1. For case 1, three meshes with 9,261, 16,600, and 29,304 volumes were considered. The GCI was calculated in six different periods (900, 1800, 2700, 3600, 4500, and 5400 s) of the total solution time, with an average value of 2.35%, considering the second grid. For case 2, meshes with 19,229, 35,490, and 62,315 volumes were chosen and five periods were selected (400, 800, 1200, 1600, and 2000 s) to calculate the GCI, with an average value of 3.87%, for the second grid. Based on the results of Figures 11a and 12a and considering average GCI of 2.35% and 3.87%, meshes with 16,600 and 35,490 volumes were selected for cases 1 and 2, respectively.

A time step verification was also performed, with values of 0.2 s, 0.1 s, and 0.05 s for both cases, and the trend of the liquid fraction is presented in Figures 11b and 12b, for cases 1 and 2, respectively. As a good trade-off between accuracy and computational time, 0.1 s were selected for both cases. It is worth noting that, for case 2, 0.2 s also provided an independent solution for the time step. Nevertheless, the number of iterations to achieve convergence significantly increased, such that the simulation time was not advantageous, compared to that of 0.1 s.

Figure 11. a) Mesh and b) time step verification results for case 1.

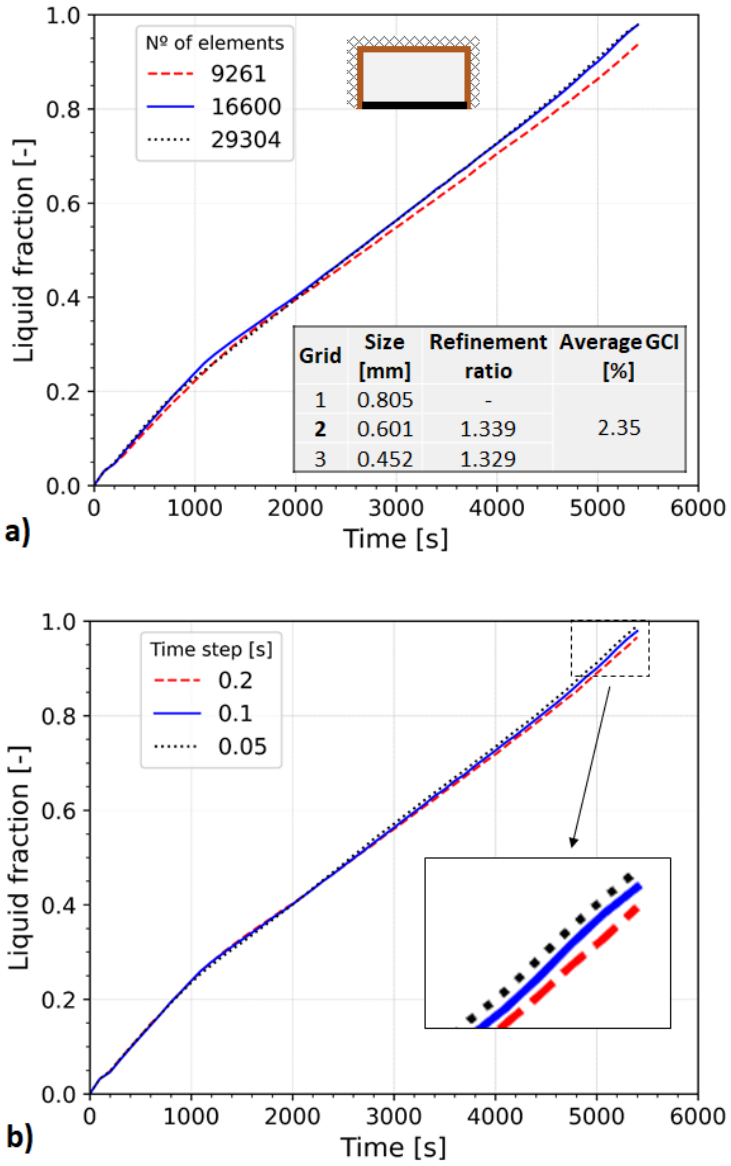

Source: adapted from Rocha *et al*. (2023c).

Figure 12. a) Mesh and b) time step verification results for case 2.

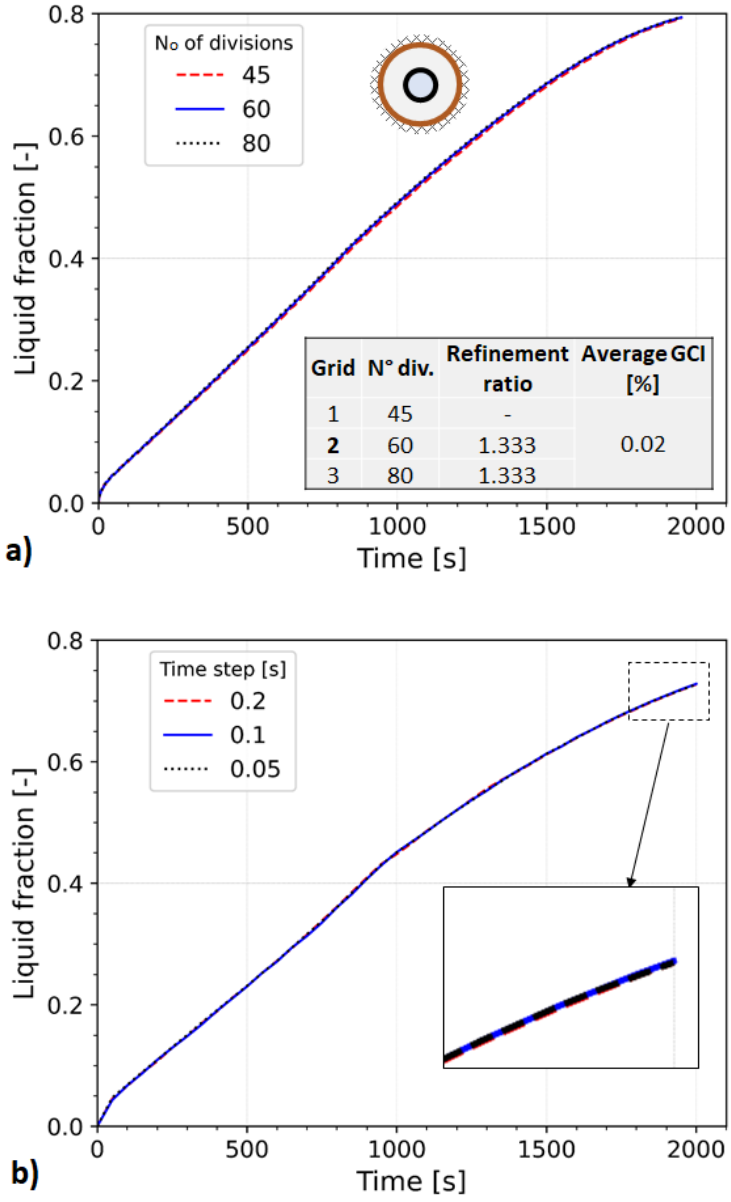

Source: adapted from Rocha *et al*. (2023c).

3.2. Simplified model

The description of the simplified model follows the same sequence of the CFD model, with few differences. It begins stablishing the physical domain, followed by the mathematical formulation, numerical implementation, development of the effective thermal conductivity, and verification of mesh and time step.

3.2.1. Physical domain

The major complexity of the previous model is to solve the coupled governing equations. However, if, somehow, the natural convection could be disregarded, continuity and momentum equations will not be required anymore, such that the model would be treated as a pure conduction. Nevertheless, natural convection is the major phenomenon affecting melting and simply disregarding it could cause a great loss in accuracy (Rocha et al., 2023b). Therefore, this simplified model is based on the pure conduction model, but takes natural convection into account via the effective thermal conductivity. Another advantage of the pure conduction assumption is that an axisymmetric melting occurs around the inner tube. This implies in reducing the problem to a one-dimensional case. Nevertheless, a two-dimensional model was developed to allow the possibility to include a variable convective coefficient as the boundary condition. A schematic representation of the physical domain is depicted in Figure 13. The PCM thermophysical properties and the dimensions for this simplified model match that of case 2 of the CFD model.

Figure 13. Physical domain of the PCM heat exchanger for the simplified model.

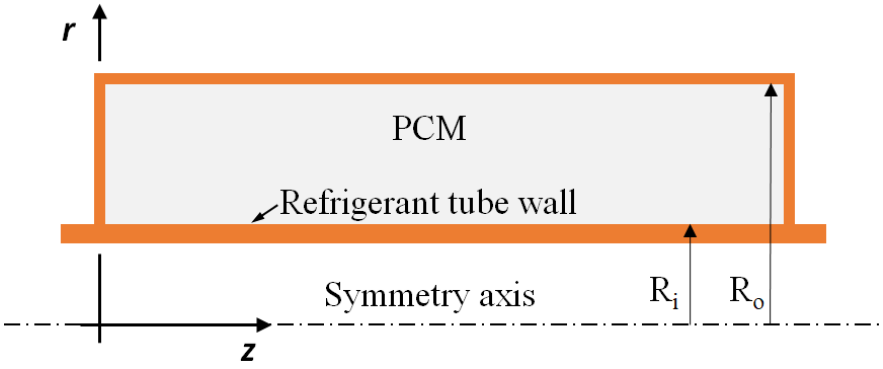

Source: the author.

3.2.2. Mathematical formulation

Considering the domain of this model, the governing (energy conservation) equation for the PCM is given by Eq. 34. Additional assumptions are: (i) constant thermophysical properties (except the thermal conductivity); (ii) contact thermal resistance of the solid PCM with the tube wall is negligible; (iii) thermal resistance of the tube wall is negligible.

$$\frac{\partial h}{\partial t} = \frac{1}{r}\frac{\partial}{\partial r}\left(\alpha r \frac{\partial h}{\partial r}\right) + \frac{\partial}{\partial z}\left(\alpha \frac{\partial h}{\partial z}\right) - \rho L \frac{\partial f}{\partial t} \tag{34}$$

The relation between the total enthalpy (H), sensible (h), and latent (ΔH) is the same as that presented by Eq. 31. In this simplified model, h_{ref} is set to zero, T_{ref} is considered to be the

melting temperature (T_{m}), and only isothermal phase-changes are considered, as illustrated by the enthalpy-temperature curve in Figure 14.

Figure 14. Total enthalpy versus temperature diagram for an isothermal phase-change.

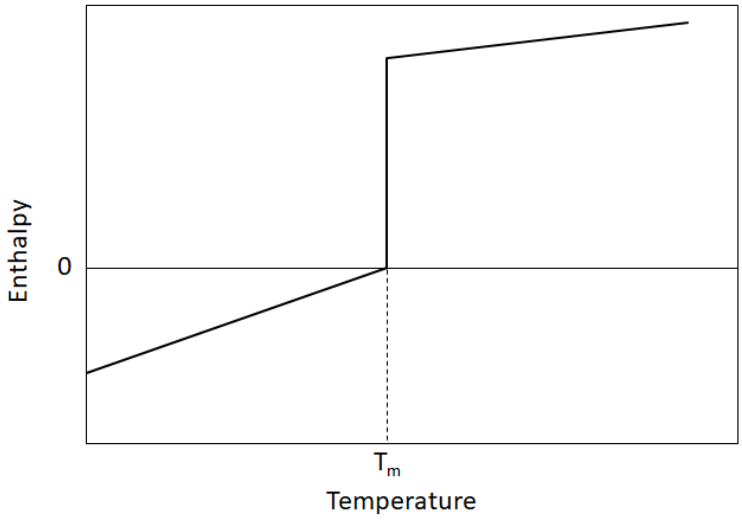

Source: the author.

To recover the temperature from the total enthalpy, Eq. 35 can be used, which is the exact representation of Figure 14.

$$T = \begin{cases} \dfrac{H}{\rho c_{\mathrm{p}}} + T_{\mathrm{m}}, & \text{if } H < 0 \\ T_{\mathrm{m}}, & \text{if } 0 \leq H \leq \rho L \\ \dfrac{H - \rho L}{\rho c_{\mathrm{p}}} + T_{\mathrm{m}}, & \text{if } H \geq \rho L \end{cases} \tag{35}$$

For this model, the external surfaces can be considered as adiabatic or subjected to natural convection with the ambient air, while the inner surface may be subjected to convection or be isothermal. These boundary conditions are given by Eq. 36, while the initial condition is presented in Eq. 37.

$$\text{at } r = R_{\mathrm{i}}, \qquad -k\frac{\partial T}{\partial r} = h_{\mathrm{HTF}}(T_{\mathrm{HTF}} - T_{\mathrm{W}}) \text{ or } T = T_{\mathrm{W}} \tag{36a}$$

$$\text{at } r = R_{\mathrm{o}}, \qquad \frac{\partial h}{\partial r} = 0 \quad \text{or} \quad -k\frac{\partial T}{\partial r} = h_{\mathrm{air}}(T_{\mathrm{air}} - T_{\mathrm{W}}) \tag{36b}$$

$$\text{at } z = 0 \text{ and } z = L, \qquad \frac{\partial h}{\partial z} = 0 \quad \text{or} \quad -k\frac{\partial T}{\partial z} = h_{\text{air}}(T_{\text{air}} - T_{\text{W}}) \tag{36c}$$

$$\text{for } t = 0, \qquad T(r, z) = T_{\text{ini}} \tag{37}$$

3.2.3. Numerical implementation

The simplified model was also based on the FVM, but implemented in Python language. This programming language was chosen due to its crescent utilization in several engineering areas, its open-source nature, and wide availability of modules. The discretization considered cell-centered volumes as represented in Figure 15.

Figure 15. Discretized domain to apply the FVM for the simplified model.

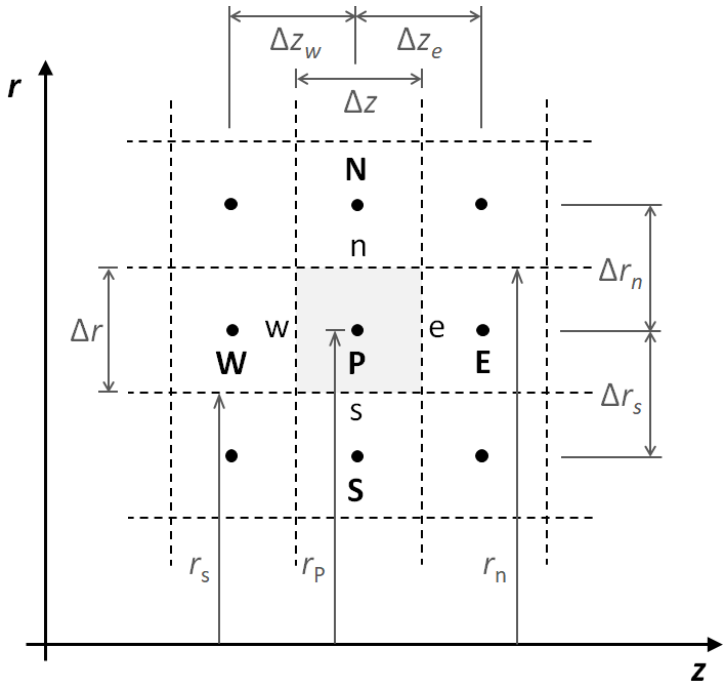

Source: the author.

After integrating Eq. 34 in time and space over each control volume and rearranging it, a system of algebraic equations with the general form of Eq. 38 can be written. For the central volumes, the coefficients of Eq. 38 are given by Eq. 39. A similar procedure was done to incorporate the boundary conditions and all the details can be found in Appendix A.

$$A_{\text{P}}h_{\text{P}} = A_{\text{E}}h_{\text{E}} + A_{\text{W}}h_{\text{W}} + A_{\text{N}}h_{\text{N}} + A_{\text{S}}h_{\text{S}} + B \tag{38}$$

$$A_{\mathrm{N}} = \frac{\Delta z}{\Delta r_{\mathrm{n}}} \alpha_{\mathrm{n}} r_{\mathrm{n}} \tag{39a}$$

$$A_{\mathrm{S}} = \frac{\Delta z}{\Delta r_{\mathrm{s}}} \alpha_{\mathrm{s}} r_{\mathrm{s}} \tag{39b}$$

$$A_{\mathrm{E}} = \frac{\Delta r}{\Delta z_{\mathrm{e}}} \alpha_{\mathrm{e}} r_{\mathrm{P}} \tag{39c}$$

$$A_{\mathrm{W}} = \frac{\Delta r}{\Delta z_{\mathrm{w}}} \alpha_{\mathrm{w}} r_{\mathrm{P}} \tag{39d}$$

$$A_{\mathrm{P}} = A_{\mathrm{N}} + A_{\mathrm{S}} + A_{\mathrm{E}} + A_{\mathrm{W}} + \frac{r_{\mathrm{P}} \Delta z \Delta r}{\Delta t} \tag{39e}$$

$$B = \frac{r_{\mathrm{P}} \Delta z \Delta r}{\Delta t} \left[{h_{\mathrm{P}}}^{0} + \rho L \left({f_{\mathrm{P}}}^{0} - f_{\mathrm{P}} \right) \right] \tag{39f}$$

A fully implicit scheme was chosen for time interpolation, while central differences were selected to approximate the diffusive terms. Eq. 38 was solved iteratively, with the liquid fraction update, using the tridiagonal matrix algorithm (TDMA). When the phase-change is occurring inside a volume, its liquid fraction must be updated for the next iteration. The method proposed by Voller (1990), with the form of Lacroix (1993), is used to calculate ${f_{\mathrm{P}}}^{k+1}$, as shown by Eq. 40. If a nodal point is suffering phase-change, then the coefficient A_{P} is forced to a large number, e.g. 10^{15}.

$${f_{\mathrm{P}}}^{k+1} = {f_{\mathrm{P}}}^{k} + \frac{A_{\mathrm{P}} h_{\mathrm{P}}}{\rho L r_{\mathrm{P}} \Delta z \Delta r} \tag{40}$$

where ${f_{\mathrm{P}}}^{k} = f_{\mathrm{P}}$, which is the liquid fraction at the k$^{\mathrm{th}}$ iteration and ${f_{\mathrm{P}}}^{k+1}$ is the liquid fraction at the k+1$^{\mathrm{th}}$ iteration. In practice, Eq. 40 is applied at every node, but a correction, expressed by Eq. 41, may be necessary for those nodes not suffering phase-change.

$$f_{\mathrm{P}}{}^{k+1} = \begin{cases} 0, & \text{if } f_{\mathrm{P}}{}^{k+1} < 0 \\ 1, & \text{if } f_{\mathrm{P}}{}^{k+1} > 1 \end{cases} \tag{41}$$

The convergence of the iterative solution between enthalpy and liquid fraction, in a given time step, is verified considering the sum of residuals, Eq. 42 (Voller, 1990). The global algorithm of the simplified model is represented in Figure 16.

$$\sum \frac{|A_{\mathrm{P}} h_{\mathrm{P}} - A_{\mathrm{E}} h_{\mathrm{E}} - A_{\mathrm{W}} h_{\mathrm{W}} - A_{\mathrm{N}} h_{\mathrm{N}} - A_{\mathrm{S}} h_{\mathrm{S}} - B|}{c_{\mathrm{p}}} < 10^{-4} \tag{42}$$

Figure 16. Algorithm of the simplified model of the PCM heat exchanger.

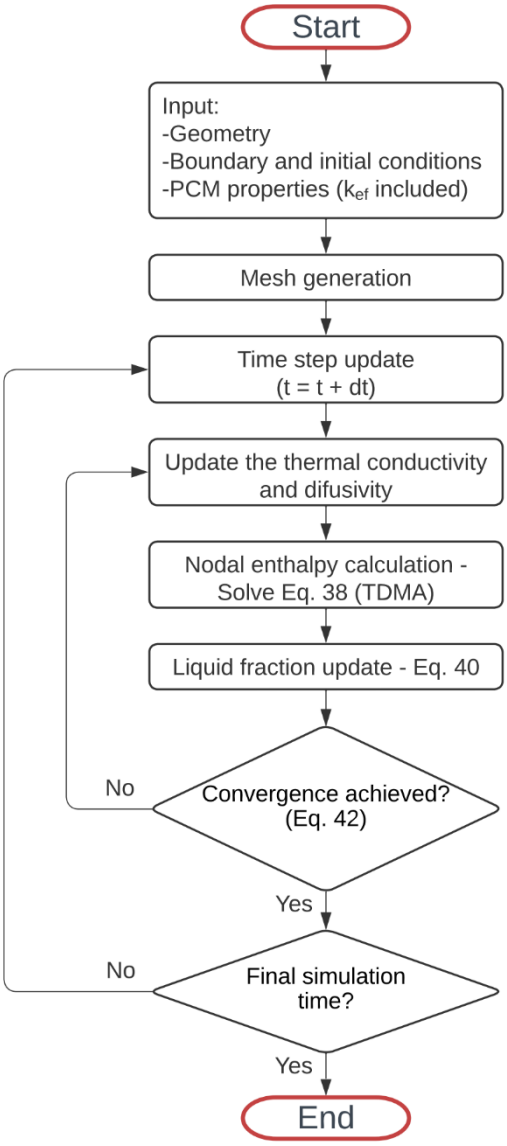

Source: the author.

3.2.4. Development of the effective thermal conductivity

Based on the results of the CFD model, the effective thermal conductivity can be derived from an energy balance, expressed by Eq. 43, where the left-hand side express the heat transfer by convection and the right-hand side is the heat transfer by conduction, occurring in the melted PCM.

$$hA(T_{\mathrm{W}} - T_{\mathrm{m}}) = \frac{2\pi L k_{\mathrm{ef}}(T_{\mathrm{W}} - T_{\mathrm{m}})}{\ln(R_{\mathrm{sl}}/R_{\mathrm{i}})} \tag{43}$$

where R_{sl} is the radius of the solid/liquid interface and L is the length of the heat exchanger. Note that the reference temperature in the left-hand side of Eq. 43 was selected as the melting temperature, T_{m}, when calculating the convective coefficient trough Eq. 44.

$$h = \frac{q''}{T_{\mathrm{W}} - T_{\mathrm{m}}} \tag{44}$$

where q'' is the heat flux. Recognizing that the heat transfer area is expressed by $A = \pi D_{\mathrm{i}} L$, Eq. 43 is rearranged to give the effective thermal conductivity, Eq. 45.

$$k_{\mathrm{ef}} = h[R_{\mathrm{i}}\ln(R_{\mathrm{sl}}/R_{\mathrm{i}})] \tag{45}$$

It should be highlighted that, $k_{\mathrm{ef}} < k_{\mathrm{l}}$ does not have a physical meaning, once the effective thermal conductivity cannot be lower than that of the pure conduction situation, so that $k_{\mathrm{ef}} = k_{\mathrm{l}}$ is assumed in this case.

Since the melted region evolves in a non-symmetric shape, due to natural convection, it is necessary to establish a procedure to calculate an equivalent radius for the solid/liquid interface. The methodology considered in the present work is based on that described by Liao *et al.* (2018), who investigated the PCM melting inside a sphere. By definition, the liquid fraction is the ratio of the liquid PCM volume to the total PCM volume, which, for a shell-and-tube unit, is given by Eq. 46a. After rearrangement, Eq. 46b. gives the radius of the solid-liquid interface.

$$f = \frac{\pi\left({R_{\mathrm{sl}}}^2 - {R_{\mathrm{i}}}^2\right)}{\pi\left({R_{\mathrm{o}}}^2 - {R_{\mathrm{i}}}^2\right)} \tag{46a}$$

$$R_{\mathrm{sl}} = \left[f\left({R_{\mathrm{o}}}^2 - {R_{\mathrm{i}}}^2\right) + {R_{\mathrm{i}}}^2\right]^{1/2} \tag{46b}$$

3.2.5. Mesh and time step verification

Although the model was developed in two dimensions, the constant temperature of the tube lead the problem to a one-dimensional situation. Hence, the discretization in the z direction is not necessary for this specific boundary condition. Indeed, this condition was verified where the number of volumes in the axis z did not alter the results. Two volumes were chosen for the z direction as a default for all the simulations, since the model cannot assign the appropriate coefficients for just one volume.

The verification for grid and time step independence results were done considering the same approach described in Section 4.1.4. The results are presented in Figure 17, where the number of divisions (Figure 17a) concerns the radial coordinate. The number of divisions of 60 and a time step of 1 second were chosen for further investigations.

Figure 17. a) Mesh and b) time step verification results for case 1.

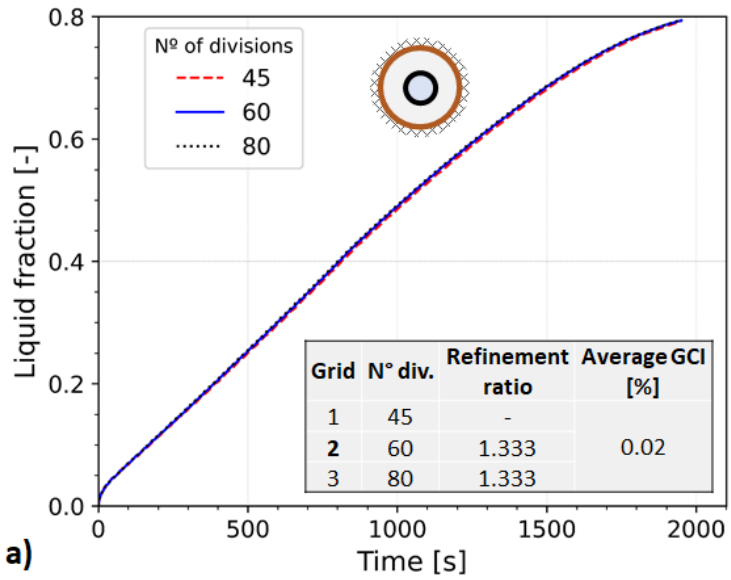

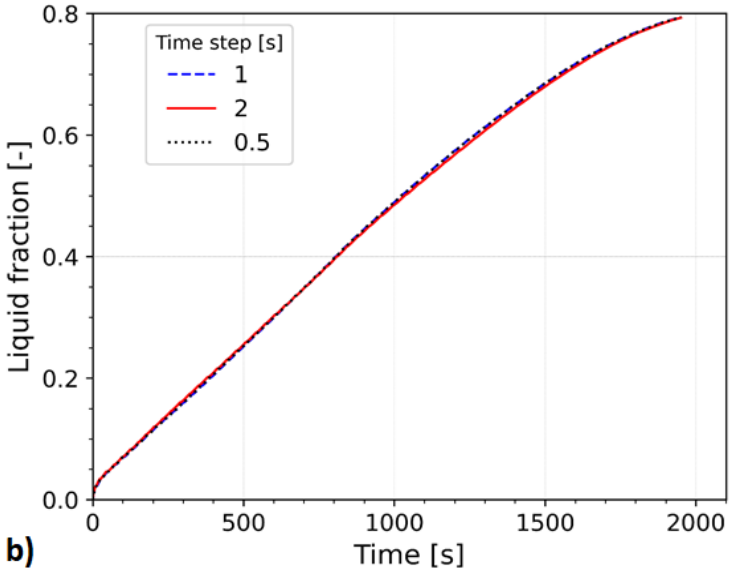

Source: the author.

To compare the numerical results of the CFD and simplified models among them and with experimental results, the absolute average deviation (AAD) is calculated with Eq. 47

$$\mathrm{AAD}=100\%\left(\frac{1}{n}\sum_{n}\left|\frac{\text{predicted}-\text{experimental}}{\text{experimental}}\right|\right) \tag{47}$$

where n is the number of calculation points.

4. RESULTS AND DISCUSSIONS

In this chapter, the results concerning the simulations with the CFD model are presented in subsection 4.1, while the outcomes related to the simplified model are discussed in subsection 4.2.

4.1. CFD model

The results of this section comprises the validation, the analysis of the porosity constant, PCM properties, combining effect of porosity constant with PCM properties, and interdependency between natural convection and the porosity constant.

4.1.1. Validation

To assure the adequacy of the proposed model, the predicted results for the liquid fraction (Figure 18a) and the average convective coefficient (Figure 18b), for case 1, were contrasted with the experimental values reported by Kamkari *et al*. (2014). Concerning the liquid fraction, a maximum deviation of 11.2% (at 800 s) and AAD of 3.3% were found. For the convective coefficient, larger deviations were observed, being the maximum and AAD values of 41.5% (at 500 s) and 9.1%, respectively. Nevertheless, the trend is consistent and the maximum deviation occurred at the beginning of the melting process. From 1000 s onwards, the maximum deviation was 11.6%. Therefore, the adopted parameters, with the porosity constant equal to 7.5×10^5, were considered satisfactory to validate the model. The experimental ranges in case 1 were considered to be between 400 s and 5300 s and between 400 s and 5100 s for the liquid fraction and convective coefficient, respectively, in order to avoid data extrapolation.

Figure 18. Comparison of the predicted: a) liquid fraction; b) convective coefficient against the experimental values of Kamkari *et al*. (2014), for case 1.

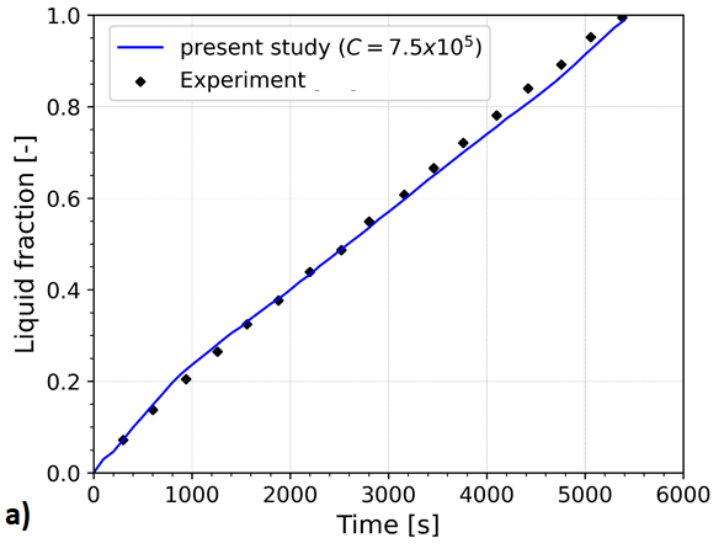

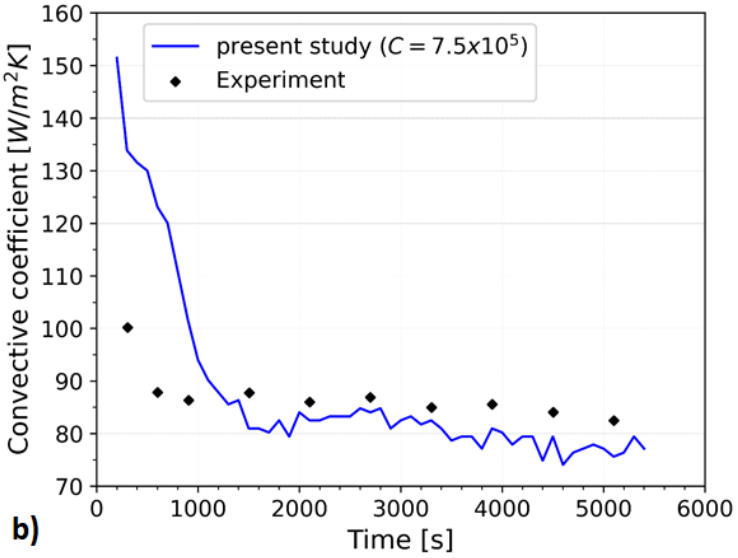

Source: Rocha *et al*. (2023c).

For case 2, the liquid fraction predictions were contrasted with the experiments of Yuan *et al*. (2016), as presented in Figure 19. Maximum and AAD of 9.3% (at 550 s) and 4.51% were found for the experimental range, between 550 s and 1700 s. The predictions are also consistent with the numerical results reported by Li *et al*. (2022). In this sense, this second validation set, with $C = 7.5 \times 10^4$, was also considered satisfactory, for case 2. These values of the porosity constant chosen for validation were those who led to the best accuracy, as presented in the next section (3.1).

Figure 19. Comparison of the predicted liquid fraction versus the numerical data of Li *et al*. (2022) and the experiments of Yuan *et al*. (2016), for case 2.

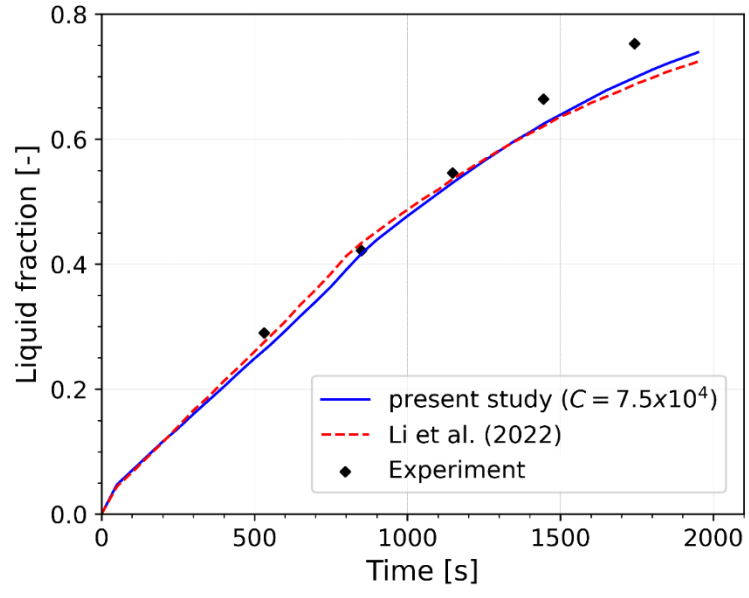

Source: adapted from Rocha *et al*. (2023c).

4.1.2. Porosity constant

Initially, the isolated effect of the porosity constant on the results accuracy was assessed in terms of the liquid fraction. For case 1 (Figure 20a), five values between 2.5×10^5 and 10^6 were tested, being $C = 7.5 \times 10^5$ the most suitable. A typical value of $C = 10^5$ was also tried, but the solution started not converging from about 2000 s onwards. For $C = 2.5 \times 10^5$, convergence was not achieved for several time steps between 4700 s and 5400 s. The maximum and AADs, compared to the experimental data, are indicated in Table 7. As observed, despite the lower variation of the C values, AAD of up to 11.8% were identified. For case 2, eight values between 10^4 and 10^7 were verified, as shown in Table 7. For a better visualization, some of them were omitted in Figure 20b. As noted, the value of 10^4 over predicted the liquid fraction up to about 1750 s, when, from there on, it became to under predict it. This behavior could be connected to an alteration of the natural convection intensity at $f \approx 0.4$, as discussed in Section 3.4. For lower values than the reference (7.5×10^4), the behavior was the opposite, i.e. the solution initially under predicted the liquid fraction and at the end of the simulation, started to over predict it.

Figure 20. Liquid fraction evolution for different values of the porosity constant: a) case 1; b) case 2.

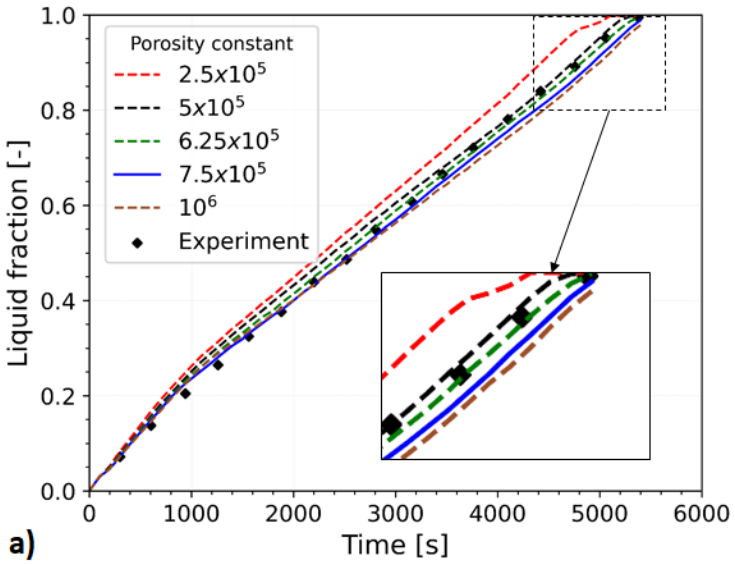

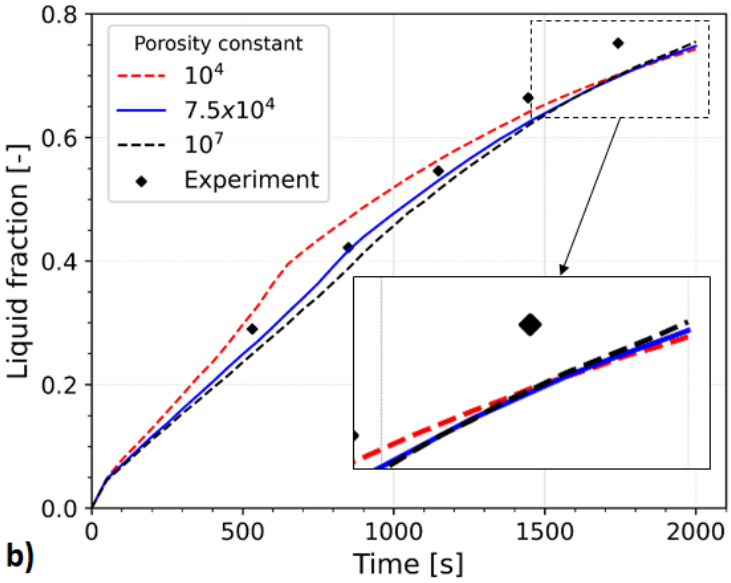

Source: adapted from Rocha *et al*. (2023c).

Table 7. Deviations on the liquid fraction for different values of the porosity constant for cases 1 and 2.

Case 1 (validation 7.5×10^5)			**Case 2 (validation 7.5×10^4)**		
C value	Maximum [%]	AAD [%]	*C* value	Maximum [%]	AAD [%]
5×10^5	16.1	5.9	10^4	16.5	7.0
6.25×10^5	12.9	3.8	5×10^4	8.7	4.9
10^6	11.1	4.3	10^5	9.3	4.8
			5×10^5	11.0	5.2
			10^6	11.3	5.6
			2.5×10^6	12.4	6.4
			10^7	13.7	7.5

Source: Rocha *et al*. (2023c).

Another aspect that could be observed analyzing Table 7 is that case 2 (isothermal) was less impacted by the alteration of the porosity constant, compared to case 1 (non-isothermal). This result agrees with the hypothesis of Vogel and Thess (2019). Nevertheless, it is clear that the isothermal material (case 2) was also affected by the porosity constant. Therefore, based on the present results, it is recommended to check this parameter when validating the model, regardless if a mushy or isothermal material is considered.

4.1.3. PCM thermosphysical properties

Since Boussinesq approximation is frequently adopted in phase-change simulations, the effect of altering the density and the coefficient of thermal expansion, appearing in Eq. 7, was investigated. The liquid fraction progress over the simulation time is represented in Figure 21a,

for case 1. As it can be observed, a slightly improvement was found when altering from the average (912.5 kg/m³) to the liquid PCM density reported by Shokouhmand and Kamkari (2013) (885 kg/m³, Table 3), where the AAD changed from 5.9% to 5.4%, respectively. Nevertheless, this is negligible compared to the influence of β, when the AAD changed from 5.9% ($\beta = 0.000615\ \mathrm{K}^{-1}$) to 13.4% ($\beta = 0.00083\ \mathrm{K}^{-1}$, Shaker *et al*. (2021)). For case 2, the density alteration from 862.9 kg/m³ (at 60°C, Yuan *et al*. (2016)) to 848.3 kg/m³ (at 80°C, Yuan *et al*. (2016)) was also verified, but the difference on the liquid fraction evolution was negligible. Therefore, selecting appropriate values of β is more critical than the density value.

Considering case 2 (isothermal), the phase-change temperature also produced different results, as depicted in Figure 21b. The liquidus temperature of case 1 (43.5°C) demonstrated to be the most representative value to be assumed for the melting temperature, followed by the value of Yuan *et al*. (2016) (44.2°C), and the average of the liquidus and solidus temperatures of case 1 (45.85°C). In this order, the AADs were 4.8%, 6.9%, and 11.7%, compared to the experimental results. Nevertheless, for solidification, it is suggested to also test the solidus temperature as the phase-change temperature.

Figure 21. Liquid fraction evolution by varying the: a) density and coefficient of thermal expansion, in case 1; b) melting temperature, in case 2.

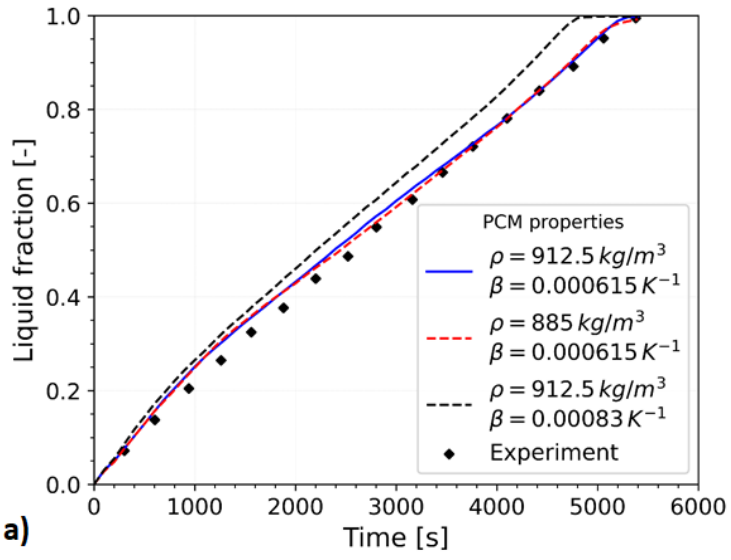

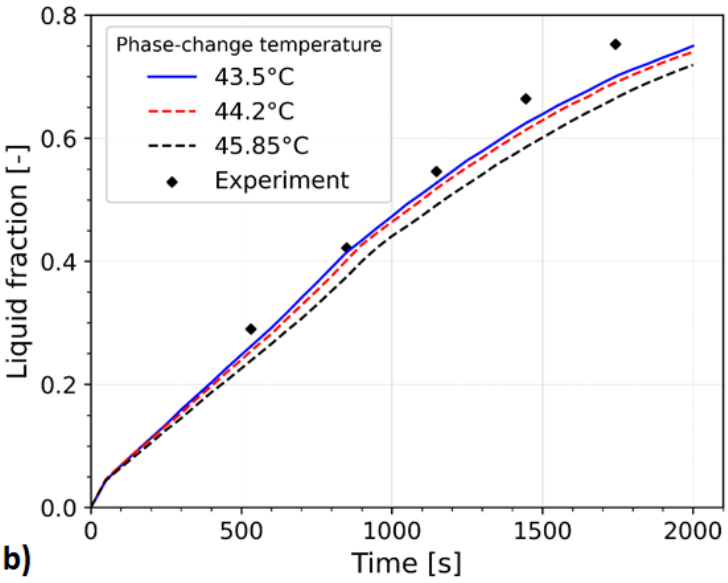

Source: adapted from Rocha *et al*. (2023c).

4.1.4. Combination of porosity constant and PCM properties

A practice frequently observed in the literature consists in validating the model for a given PCM, but using it to simulate problems that adopt different PCMs or keeping the original PCM in variable geometric configurations, as illustrated in Table 1. Frequently, the porosity constant value used for validation is kept unaltered when using the model. The effect of such an approach is assessed here.

Initially, the PCM properties and the porosity constant of case 2 were combined with the geometry and boundary conditions of case 1, which means a geometry alteration for an already validated set. The liquid fraction evolution is illustrated in Figure 22a and, as it can be seen, keeping the original value of $C = 7.5 \times 10^4$ implied in a difference for the total melting time of 1400 s (4000 s versus 5400s), or 26%, compared to the experimental results of Kamkari *et al*. (2014). Up to the total melting time, i.e. 4000 s, the maximum deviation and AAD as large as 57.9% and 38.0%, respectively, were obtained. In order to reduce these discrepancies to 23.8% and 5.7%, respectively, a correction should be done on the porosity constant, with a new value of $C = 7.5 \times 10^6$.

Subsequently, the opposite was also verified, i.e. the PCM properties and the porosity constant of case 1 were combined with the geometry and boundary conditions of case 2, as visualized in Figure 22b, where maximum and AAD of 28.1% and 23.4%, respectively, were obtained. Nevertheless, in this situation, the solution did not converge for $C \leq 5 \times 10^5$, being not possible to assess the necessary correction on the porosity constant that would lead to a

satisfactory agreement. These results clearly indicates that the combining effect of the original porosity constant with the new geometry could lead to unreliable findings. It should be highlighted that the PCM properties were not altered, i.e. the same information used in validation was repeated for the new simulation. Therefore, altering the PCM used in novel simulation scenarios, compared to that of validation, could further exacerbate this discrepancy.

Figure 22. Liquid fraction evolution for: a) PCM properties of case 2 and geometry of case 1 – experiment of Kamkari *et al*. (2014); b) PCM properties of case 1 and geometry of case 2 – experiment of Yuan *et al*. (2016).

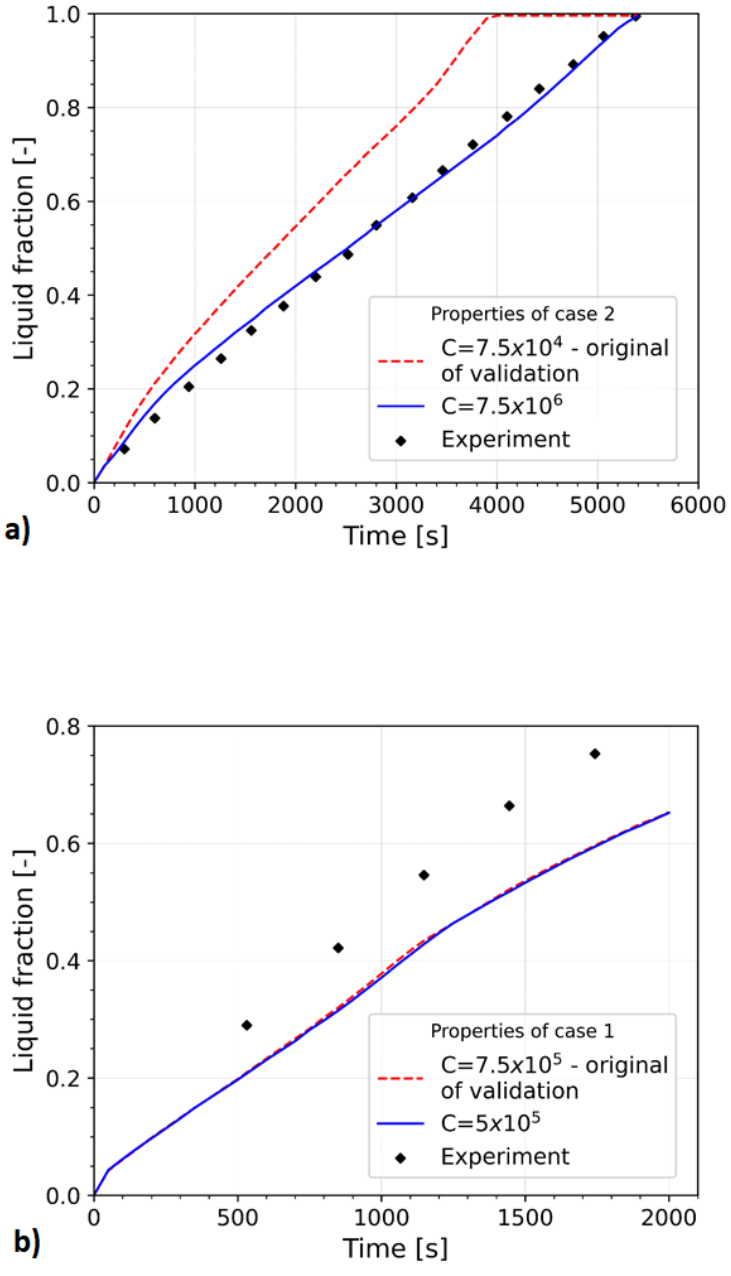

Source: adapted from Rocha *et al*. (2023c).

4.1.5. Further insights on the porosity constant and natural convection

The phenomenon behind the behavior appearing in Figure 22a is the alteration of the natural convection intensity, which changed the optimal porosity constant from 7.5×10^4 (geometry of case 2) to around 7.5×10^6 (geometry of case 1). Since the Rayleigh number, Eq. 21, depends on the proper choice of a characteristic length, it is not possible to directly compare the natural convection intensity for these two different configurations. Therefore, the velocity and the convective coefficient were examined to verify if any relation is revealed. These variables were contrasted considering instants with the same liquid fraction, since the dimensionless time (Fourier number) also depends on the characteristic length. Noting that the PCM properties are those of case 2, the velocity field is indicated in Figure 23, for cases 1 and 2, in instants where $f = 0.4$. As it can be noted, the maximum velocity for case 2 (11.8 mm/s) is 80% higher than that of case 1 (6.56 mm/s), indicating a stronger convective motion for case 2. To verify if this is a trend for the entire melting process, the average velocity of the whole PCM domain is plotted versus the liquid fraction, as shown in Figure 24a. The maximum liquid fraction for case 2 was 0.75 and, therefore, this threshold was also employed for case 1.

Figure 23. Velocity field for instants where the liquid fraction is equal to 0.4: a) geometry of case 1; b) geometry of case2.

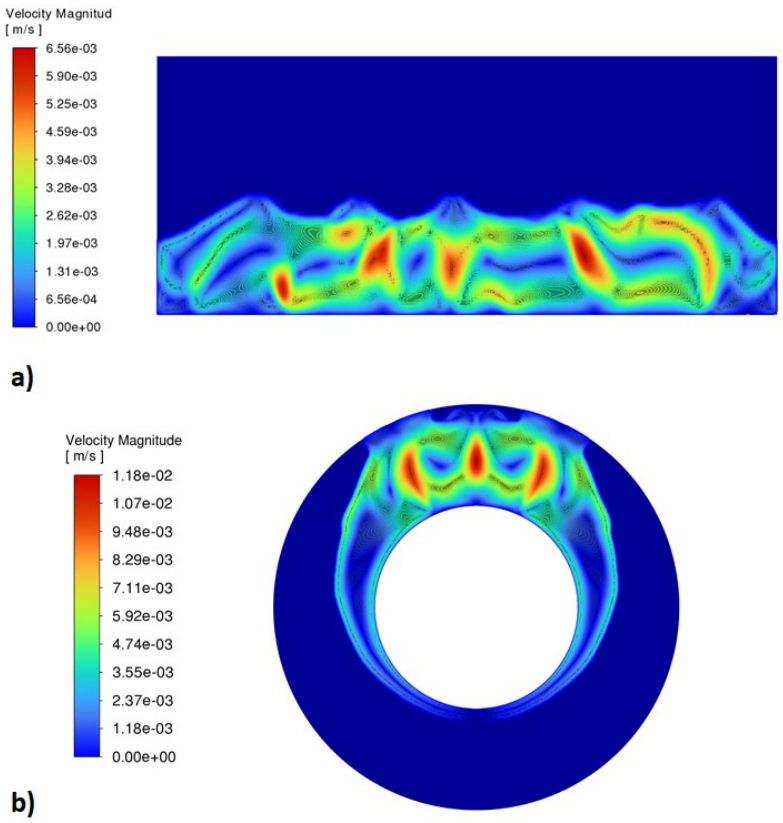

Source: Rocha *et al*. (2023c).

Figure 24. Evolution of the average: a) PCM velocity; b) convective coefficient for geometries of cases 1 and 2.

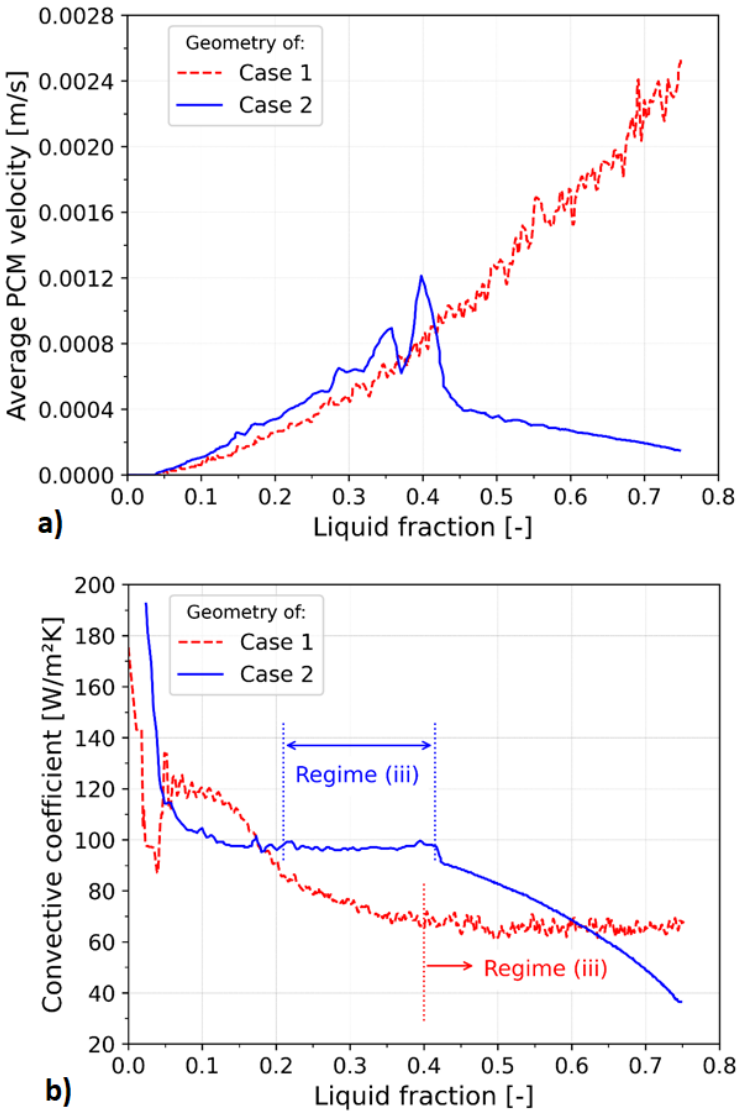

Source: adapted from Rocha *et al*. (2023c).

As it can observed from Figure 24a, the velocity of case 2 increased up to $f \approx 0.4$, when it started decreasing, differently to what occurred for case 1, where the velocity kept raising. This can be explained by the reduction of natural convection in case 2 and happened because the average temperature of the liquid PCM approached the wall temperature, reducing the buoyancy force that promotes the PCM flow. This is illustrated in Figure 25 for instants where the liquid fraction is 0.6.

Figure 25. Temperature field for instants where the liquid fraction is equal to 0.6: a) geometry of case 1; b) geometry of case 2.

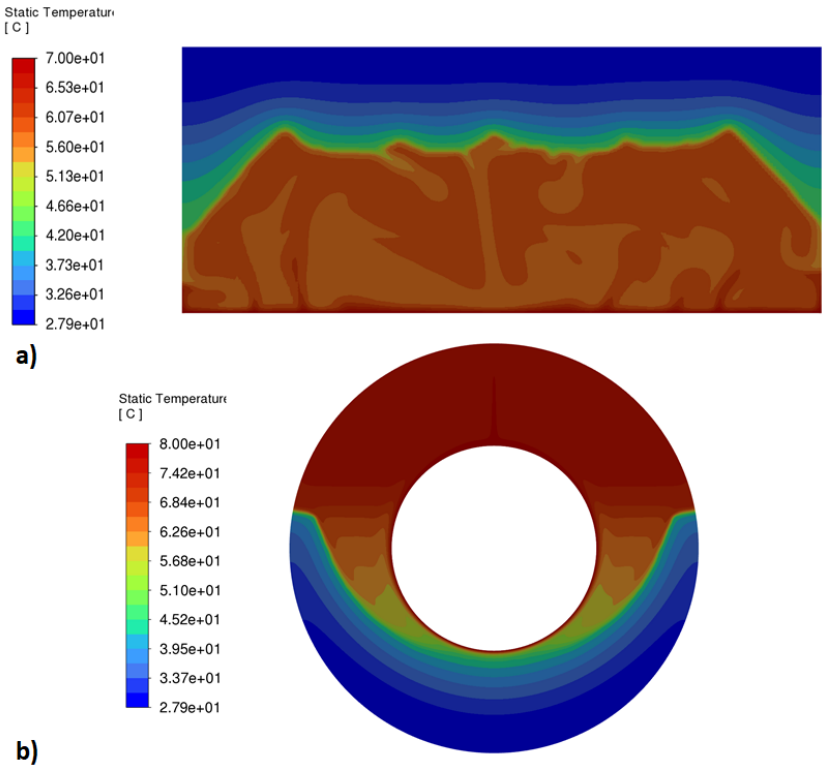

Source: Rocha *et al*. (2023c).

From Figure 25b, it is possible to see that the upper part of the annulus (geometry of case 2) is almost entirely at the same temperature, approaching the wall temperature of 80°C, while the remaining liquid phase presents a stratified temperature distribution. In contrast, the geometry of case 1 exhibits a temperature gradient more randomly distributed in the liquid fraction (Figure 25a), which could justify a higher convective flow. Nevertheless, up to $f \approx 0.4$, the average velocity of case 2 is higher than that of case 1, which can be associated with the natural convection intensity in these situations. To corroborate this hypothesis, the convective coefficient is plotted versus the liquid fraction in Figure 24b.

In some situations, as in the present study, it is not possible to easily identify the boundaries between the regions identified by Jany and Bejan (1988), especially the transition one. Nevertheless, the natural convection dominant regime (iii) can be clearly seen in Figure 24b, for both geometries. The convective heat transfer coefficient is associated to Nu and, from the equations on Tables 4 and 5, it is observed that this coefficient is proportional to the Rayleigh number, which is an indicator of the natural convection intensity. Hence, considering regime (iii), it can be said that the intensity in case 2 is greater than that of case 1. Concerning the porosity constant, its value was lower for case 2, where natural convection is stronger. This

result is also in line with that of Troxler *et al*. (2023), in which the best C value changed from 10^5, for a wall temperature of 60°C (lower Ra), to 3×10^4, for a wall temperature of 70°C (higher Ra). Therefore, the lower the natural convection intensity, the higher the porosity constant should be. One attempt to calculate the porosity constant was found in the work of Zeneli *et al*. (2019), who modelled the melting of silicon as the PCM. Although their correlation was related to the viscosity, density, and distance between dendrites secondary arms, the development of other estimators is encouraged.

4.2. Simplified model

Initially, this section presents the comparison of the results obtained with the simplified model with those obtained experimentally and with the CFD model. Subsequently, the available correlations are to predict the effective thermal conductivity are assessed.

4.2.1. Validation

To verify the suitability of the simplified model, the predictions for the liquid fraction were compared to those of the experimental data of Yuan *et al*. (2016) and to the CFD model, as presented in Figure 26. Considering the CFD model, maximum and AAD of 8.17% (at 1700 s) and 4.32%, respectively, were observed between 0 and 1950 s of simulation. This is comparable to the 8.6% reported by Tehrani *et al*. (2019), who investigated the melting of high temperature PCMs in a vertical shell-and-tube unit. Concerning the experimental data, the simulation range is narrowed to 550 and 1700 s, achieving maximum and AAD of 7.43 % (at 550 s) and 1.67%, respectively.

One of the features of a pure conduction (simplified) model is the lower processing time, compared to a full CFD model. For instance, the simulation with the simplified model took 28 seconds versus 1656 minutes for the CFD model, being, at least, 3500 times faster. Therefore, besides being able to properly predict the liquid fraction evolution, this model is a useful tool for integration with more comprehensive systems.

Figure 26. Comparison of the predicted liquid fraction for the simplified model versus the CFD model and the experiments of Yuan *et al*. (2016).

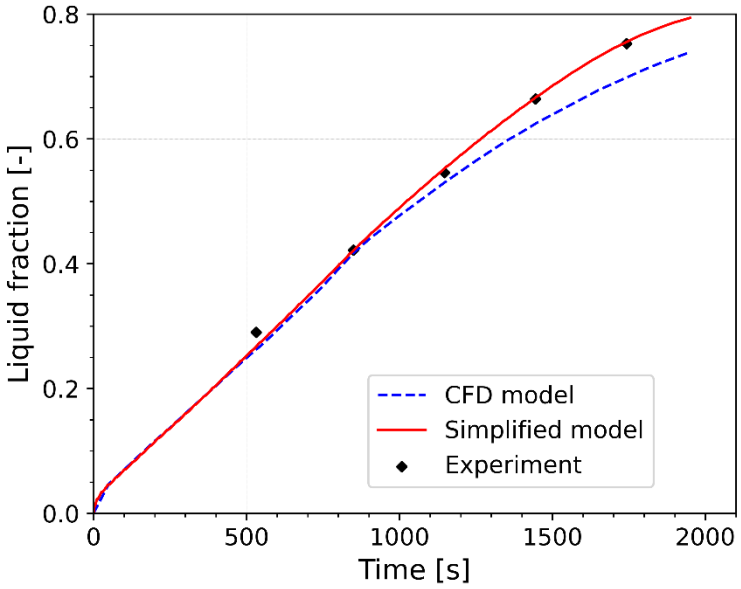

Source: the author.

4.2.2. Assessment of correlations for the effective thermal conductivity

The effective thermal conductivity derived from the numerical data of the CFD model was contrasted with those of the correlations provided by Lacroix (1993), El Qarnia (2009), Adine and El Qarnia (2009), and Wang *et al*. (2013), Eqs. 22-25, respectively. The results are illustrated in Figure 27 and, as observed, none of them was able to capture the reduction of k_{ef} due to the shrinkage of natural convection (fourth regime). This behavior was expected since all of them were developed exclusively for the region of natural convection dominance (third regime). The correlation of Adine and El Qarnia (2009) reproduced very well k_{ef} up to $f \approx 0.15$, presented satisfactory agreement for $0.15 < f < 0.4$, and diverged for $f > 0.4$, while the remaining predictors deviated in the entire range.

Figure 27. Effective thermal conductivity provided by the numerical data of the CFD model and by different correlations.

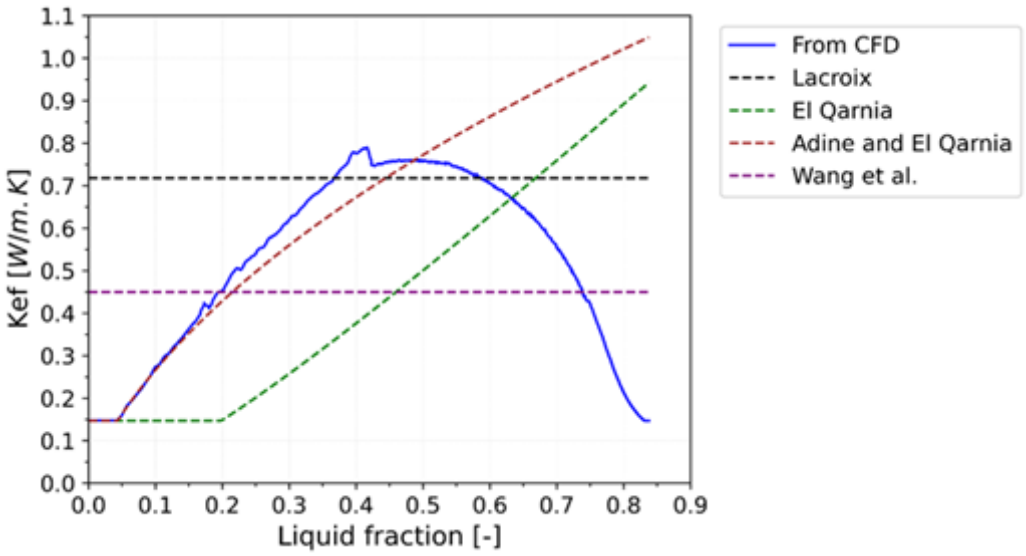

Source: the author.

The values of k_{ef} for these different correlations were implemented in the simplified model to verify the liquid fraction evolution, as presented in Figure 28. To provide a more comprehensive comparison, the simulation was extended up to 3000 s. The maximum and AAD were indicated in Table 8. As it is shown, none of them was able to accurately reproduce the melting progress, which was also expected due to the behavior reported in Figure 27. Therefore, caution is advised when using such correlations and the development of other predictors are strongly encouraged.

Figure 28. Liquid fraction evolution for the CFD model and for the simplified model with different effective thermal conductivities.

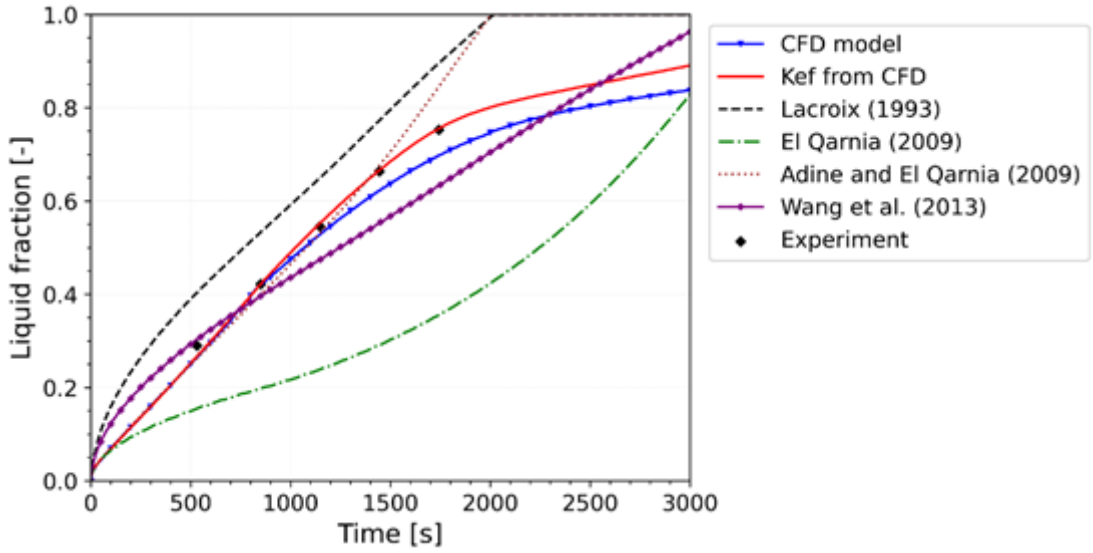

Source: the author.

Table 8. Deviations of the simplified model with different effective thermal conductivities compared to the numerical results of the CFD model.

	K_{ef} from CFD	**Lacroix (1993)**	**Qarnia (2009)**	**Adine and El Qarnia (2009)**	**Wang *et al.* (2013)**
Maximum [%]	8.17	144.82	54.92	33.60	91.42
AAD [%]	4.58	38.54	37.26	13.42	14.45

Source: the author.

5. CONCLUDING REMARKS

This section initially presents the conclusions of this work, followed by a recommendation for future investigations.

5.1. Conclusions

The theoretical investigation of thermodynamic cycles, e.g. refrigeration, employing latent thermal energy storage systems requires an integrated model of the basic system with that of the PCM melting/solidification. Besides, to be feasible, this model should present low computational time and good accuracy. Therefore, the main objective of this work was to assess the feasibility of a simplified model of a horizontal shell-and-tube PCM unit that is capable to be integrated with multiphysics systems. To accomplish that, prior simulations with a CFD software were carried out to derive an effective thermal conductivity, i.e. a boosted conductivity where the heat transfer by pure conduction equals that promoted by natural convection plus conduction. Subsequently, a pure conduction model, incorporating the effective thermal conductivity, was developed based on the enthalpy-porosity scheme and implemented in Python language.

Concerning the CFD simulations, the melting process of lauric acid was evaluated in two different scenarios: a rectangular horizontal enclosure with a non-isothermal (mushy) phase-change (case 1), and a shell-and-tube unit with an isothermal melting (case 2). A mathematical model that adopts the enthalpy-porosity scheme was written and solved, being properly validated with experimental results for both cases. The main outcomes of this investigation are:

- Concerning the porosity constant: for case 1, the best value was $C = 7.5 \times 10^5$. By altering it to 2.5×10^5, the AAD increased from 3.3% to 11.8%. The typical value of $C = 10^5$ led the solution to not converge from about 2000 s onwards. For case 2, the best value was $C = 7.5 \times 10^4$ and changing it to 10^7took the AAD from 4.5% to 7.5%. This indicated that both isothermal or mushy range materials are impacted by the porosity constant, although the first is more affected. Therefore, this parameter should always be checked when using the enthalpy-porosity scheme.
- Concerning the PCM properties: for case 1, altering from the average PCM density (912.5 kg/m³) to the liquid PCM density (885 kg/m³) cause a reduction of 0.5% on the AAD. On the other hand, by changing the source of the coefficient of thermal expansion increased the AAD in 7.5% (from $\beta = 0.000615\ \mathrm{K}^{-1}$ to $\beta = 0.00083\ \mathrm{K}^{-1}$). For case 2, the melting temperature also played a significant role, where the AAD increased in 6.9% by changing from the liquidus temperature of case 1 (43.5°C) to the average

liquidus-solidus temperature of case 1 (45.85°C). Hence, similarly to the porosity constant, the PCM properties should be validated with experimental results.

- Concerning the interaction between porosity constant and PCM properties: for the geometry of case 1 with the porosity constant (7.5×10^4) and PCM properties of case 2, a difference for the total melting time of 1400 s (26%) was found. The maximum deviation was as large as 57.9%, with an AAD for the liquid fraction of 38.0%. In order to reduce this deviation to 5.7%, the porosity constant should be adjusted to 7.5×10^6 in the new configuration. The opposite also revealed this issue, i.e. geometry of case 2 with the porosity constant and properties of case 1, with AAD of 23.4%. Nevertheless, in this situation, it was not possible to assess the proper correction on the porosity constant, since the solution did not converge for some C values that would tend to reduce the deviation. Therefore, the practice of validating the model with a PCM and using it with a distinct material or in a completely different geometry could lead to unclear results. In this sense, this praxis should be discouraged as possible, although experimental results may not be available for the desired condition.
- Concerning the relation between porosity constant and natural convection intensity: since the characteristic length is different for cases 1 and 2, which blocks a comparison of Ra, the natural convection intensity has been indirectly inferred through the assessment of velocity and convective coefficients. Notably, the findings in this work suggest that, in instances of elevated natural convection intensities, a reduction in the porosity constant is recommended.

Concerning the simplified (pure conduction) model, it was tested for the same condition (case 2) of the CFD model, being reported a good agreement with both, the CFD and experimental results, with AAD of 4.32% and 1.67%, respectively. However, the simplified model was 3500 times faster than the CFD model, proving its feasibility for integration with more comprehensive systems. The evaluation of the correlations to predict the effective thermal conductivity indicated that none of them was suitable for the full range of the present investigation, with maximum deviations achieving more than 140%, in the worst case. Therefore, caution is recommended for their utilization and a verification with experimental or validated CFD results should be carried out to assure their suitability for different PCMs and operational conditions. Although the PCM melting was considered in this work, the same methodology can be used to deal with the PCM solidification, but selecting an appropriate effective thermal conductivity.

5.2. Future works

The results presented in this work may be of interest to those engaged with the simulation of LTES systems, when using the enthalpy-porosity scheme. In this case, quantitative outcomes should be used with caution whenever the validation condition significantly differs from that of utilization. However, further investigations with different materials and/or distinct geometries could be performed to endorse, or not, the findings of this work. Besides, although the objectives of the present work were fully achieved, some opportunities for future investigations are: (i) to integrate the simplified model of the PCM melting with more comprehensive systems, e.g. a validated refrigeration cycle; (ii) to develop correlations to predict the effective thermal conductivity for horizontal shell-and-tube units; (iii) to perform experiments to validate LTES heat exchangers in different conditions.

REFERENCES

Adebiyi, G.A., Hodge, B.K., Steele, W.G., Jalalzadeh-Azar, A., Nsofor, E.C., 1996. Computer Simulation of a High-Temperature Thermal Energy Storage System Employing Multiple Families of Phase-Change Storage Materials. J. Energy Resour. Technol. 118, 102–111. https://doi.org/10.1115/1.2792700

Adine, H.A., El Qarnia, H., 2009. Numerical analysis of the thermal behaviour of a shell-and-tube heat storage unit using phase change materials. Appl. Math. Model. 33, 2132–2144. https://doi.org/10.1016/j.apm.2008.05.016

Agyenim, F., Hewitt, N., Eames, P., Smyth, M., 2010. A review of materials, heat transfer and phase change problem formulation for latent heat thermal energy storage systems (LHTESS). Renew. Sustain. Energy Rev. 14, 615–628. https://doi.org/10.1016/j.rser.2009.10.015

Ahmed, S.E., Abderrahmane, A., Alotaibi, S., Younis, O., Almasri, R.A., Hussam, W.K., 2021. Enhanced Heat Transfer for NePCM-Melting-Based Thermal Energy of Finned Heat Pipe. Nanomaterials 12, 129. https://doi.org/10.3390/nano12010129

Al Siyabi, I., Khanna, S., Mallick, T., Sundaram, S., 2019. An experimental and numerical study on the effect of inclination angle of phase change materials thermal energy storage system. J. Energy Storage 23, 57–68. https://doi.org/10.1016/j.est.2019.03.010

Alva, G., Lin, Y., Fang, G., 2018. An overview of thermal energy storage systems. Energy 144, 341–378. https://doi.org/10.1016/j.energy.2017.12.037

Amin, N.A.M., Bruno, F., Belusko, M., 2014. Effective thermal conductivity for melting in PCM encapsulated in a sphere. Appl. Energy 122, 280–287. https://doi.org/10.1016/j.apenergy.2014.01.073

ANSYS FLUENT User's Guide, 15.0. ed, 2013. . ANSYS, Inc.

Arfi, O., Mezaache, E.H., Laouer, A., 2023. Numerical investigation of double layered PCM building envelope during charging cycle for energy saving. Int. Commun. Heat Mass Transf. 144, 106797. https://doi.org/10.1016/j.icheatmasstransfer.2023.106797

Atayilmaz, Ş.O., 2011. Experimental and numerical study of natural convection heat transfer from horizontal concentric cylinders. Int. J. Therm. Sci. 50, 1472–1483. https://doi.org/10.1016/j.ijthermalsci.2011.03.019

Bechiri, M., Mansouri, K., 2015. Analytical solution of heat transfer in a shell-and-tube latent thermal energy storage system. Renew. Energy 74, 825–838.

https://doi.org/10.1016/j.renene.2014.09.010

Beckmann, W., 1931. Die Wärmeübertragung in zylindrischen Gasschichten bei natürlicher Konvektion. Forsch. auf dem Gebiete des Ingenieurwesens 2, 165–178. https://doi.org/10.1007/BF02578801

Bentilla, E.W., Sterrett, K.F., Karre, L.E., 1966. Research and development study on thermal control by use of fusible materials, NASA Technical Report, Northrop Space Laboratories.

Boger, D. V., Westwater, J.W., 1967. Effect of Buoyancy on the Melting and Freezing Process. J. Heat Transfer 89, 81–89. https://doi.org/10.1115/1.3614327

Bonacina, C., Comini, G., Fasano, A., Primicerio, M., 1973. Numerical solution of phase-change problems. Int. J. Heat Mass Transf. 16, 1825–1832. https://doi.org/10.1016/0017-9310(73)90202-0

bp, 2022. bp Statistical Review of World Energy [WWW Document]. URL https://www.bp.com/content/dam/bp/business-sites/en/global/corporate/pdfs/energy-economics/statistical-review/bp-stats-review-2022-full-report.pdf

Braga, S.L., Viskanta, R., 1992. Transient natural convection of water near its density extremum in a rectangular cavity. Int. J. Heat Mass Transf. 35, 861–875. https://doi.org/10.1016/0017-9310(92)90253-O

Cao, X., Yuan, Y., Xiang, B., Highlight, F., 2018. Effect of natural convection on melting performance of eccentric horizontal shell and tube latent heat storage unit. Sustain. Cities Soc. 38, 571–581. https://doi.org/10.1016/j.scs.2018.01.025

Carslaw, H.S., Jaeger, J.C., 1959. Conduction of Heat in Solids, 2nd ed. ed. Oxford University Press.

Celik, I.B., Ghia, U., Roache, P.J., Freitas, C.J., Coleman, H., Raad, P.E., 2008. Procedure for estimation and reporting of uncertainty due to discretization in CFD applications. J. Fluids Eng. Trans. ASME 130, 0780011–0780014. https://doi.org/10.1115/1.2960953

Chen, L., Fan, A., 2022. Effects of shell modifications and operational parameters on melting uniformity of a vertical multi-section shell-and-tube latent heat thermal energy storage unit. J. Energy Storage 55, 105593. https://doi.org/10.1016/j.est.2022.105593

CHOI, K., HONG, J., 1990. Study of ultrasonic enhancement in melting process of phase-change materials, in: 5th Joint Thermophysics and Heat Transfer Conference. American Institute of Aeronautics and Astronautics, Reston, Virigina. https://doi.org/10.2514/6.1990-1727

Choi, S.U.S., Eastman, J.A., 1995. Enhancing thermal conductivity of fluids with nanoparticles. Am. Soc. Mech. Eng. Fluids Eng. Div. FED 231, 99–105.

Colla, L., Fedele, L., Mancin, S., Buonomo, B., Ercole, D., Manca, O., 2015. Nano-PCMs for passive electronic cooling applications. J. Phys. Conf. Ser. 655, 012030. https://doi.org/10.1088/1742-6596/655/1/012030

Darzi, A.A.R., Farhadi, M., Sedighi, K., 2012. Numerical study of melting inside concentric and eccentric horizontal annulus. Appl. Math. Model. 36, 4080–4086. https://doi.org/10.1016/j.apm.2011.11.033

De Césaro Oliveski, R., Becker, F., Rocha, L.A.O., Biserni, C., Eberhardt, G.E.S., 2021. Design of fin structures for phase change material (PCM) melting process in rectangular cavities. J. Energy Storage 35. https://doi.org/10.1016/j.est.2021.102337

Dong, Y., Zhang, X., Wang, F., Zhang, G., Shi, X., Shuai, Y., 2022. Numerical study on the thermal performance analysis of packed-bed latent heat thermal storage system with biomimetic vein hierarchical structure. Int. J. Green Energy 19, 592–602. https://doi.org/10.1080/15435075.2021.1952208

El Qarnia, H., 2009. Numerical analysis of a coupled solar collector latent heat storage unit using various phase change materials for heating the water. Energy Convers. Manag. 50, 247–254. https://doi.org/10.1016/j.enconman.2008.09.038

Elsanusi, O.S., Nsofor, E.C., 2021. Melting of multiple PCMs with different arrangements inside a heat exchanger for energy storage. Appl. Therm. Eng. 185, 116046. https://doi.org/10.1016/j.applthermaleng.2020.116046

Fadl, M., Eames, P.C., 2019. Numerical investigation of the influence of mushy zone parameter Amush on heat transfer characteristics in vertically and horizontally oriented thermal energy storage systems. Appl. Therm. Eng. 151, 90–99. https://doi.org/10.1016/j.applthermaleng.2019.01.102

Fairbanks, H.V., 1979. Influence of Ultrasound Upon Heat Transfer Systems, in: 1979 Ultrasonics Symposium. IEEE, pp. 384–387. https://doi.org/10.1109/ULTSYM.1979.197226

Farid, M., Kim, Y., Honda, T., Kanzawa, A., 1989. THE ROLE OF NATURAL CONVECTION DURING MELTING AND SOLIDIFICATION OF PCM IN A VERTICAL CYLINDER. Chem. Eng. Commun. 84, 43–60. https://doi.org/10.1080/00986448908940334

Farid, M.M., Husian, R.M., 1990. An electrical storage heater using the phase-change method of heat storage. Energy Convers. Manag. 30, 219–230. https://doi.org/10.1016/0196-8904(90)90003-H

Farid, M.M., Kanzawa, A., 1989. Thermal Performance of a Heat Storage Module Using PCM's With Different Melting Temperatures: Mathematical Modeling. J. Sol. Energy Eng. 111, 152–157. https://doi.org/10.1115/1.3268301

Farid, M.M., Mohamed, A.K., 1987. EFFECT OF NATURAL CONVECTION ON THE PROCESS OF MELTING AND SOLIDIFICATION OF PARAFFIN WAX. Chem. Eng. Commun. 57, 297–316. https://doi.org/10.1080/00986448708960492

Gao, Z., Yao, Y., Wu, H., 2019. Validation of a melting fraction-based effective thermal conductivity correlation for prediction of melting phase change inside a sphere. Int. J. Therm. Sci. 142, 247–257. https://doi.org/10.1016/j.ijthermalsci.2019.04.029

Ghalambaz, Mohammad, Mehryan, S.A.M., Veismoradi, A., Mahdavi, M., Zahmatkesh, I., Kazemi, Z., Younis, O., Ghalambaz, Mehdi, Chamkha, A.J., 2021. Melting process of the nano-enhanced phase change material (NePCM) in an optimized design of shell and tube thermal energy storage (TES): Taguchi optimization approach. Appl. Therm. Eng. 193, 116945. https://doi.org/10.1016/j.applthermaleng.2021.116945

Gürbüz, H., Demirtürk, S., Akçay, H., Topalcı, Ü., 2023. Experimental investigation on electrical power and thermal energy storage performance of a solar hybrid PV/T-PCM energy conversion system. J. Build. Eng. 69, 106271. https://doi.org/10.1016/j.jobe.2023.106271

Haddad, Z., Iachachene, F., Oztop, H.F., 2021. Melting characteristics of organic phase change material in a wavy trapezoidal cavity. J. Mol. Liq. 332, 112132. https://doi.org/10.1016/j.molliq.2019.112132

Hale, N.W., Viskanta, R., 1978. Photographic observation of the solid-liquid interface motion during melting of a solid heated from an isothermal vertical wall. Lett. Heat Mass Transf. 5, 329–337. https://doi.org/https://doi.org/10.1016/0017-9310(84)90143-13

Hameed, G., Ghafoor, M.A., Yousaf, M., Imran, M., Zaman, M., Elkamel, A., Haq, A., Rizwan, M., Wilberforce, T., Abdelkareem, M.A., Olabi, A.G., 2022. Low temperature phase change materials for thermal energy storage: Current status and computational perspectives. Sustain. Energy Technol. Assessments 50, 101808. https://doi.org/10.1016/j.seta.2021.101808

Hamilton, R.L., Crosser, O.K., 1962. Thermal Conductivity of Heterogeneous Two-Component Systems. Ind. Eng. Chem. Fundam. 1, 187–191. https://doi.org/10.1021/i160003a005

Hasan, A., 1994a. Thermal energy storage system with stearic acid as phase change material. Energy Convers. Manag. 35, 843–856. https://doi.org/10.1016/0196-8904(94)90034-5

Hasan, A., 1994b. Phase change material energy storage system employing palmitic acid. Sol. Energy 52, 143–154. https://doi.org/10.1016/0038-092X(94)90064-7

Hessami, M.A., Pollard, A., Rowe, R.D., Ruth, D.W., 1985. A study of free convective heat transfer in a horizontal annulus with a large radii ratio. J. Heat Transfer 107, 603–610. https://doi.org/10.1115/1.3247467

Hirata, T., Nishida, K., 1989. An analysis of heat transfer using equivalent thermal conductivity of liquid phase during melting inside an isothermally heated horizontal cylinder. Int. J. Heat Mass Transf. 32, 1663–1670. https://doi.org/10.1016/0017-9310(89)90049-5

Ho, C.J., Chen, S., 1986. Numerical simulation of melting of ice around a horizontal cylinder. Int. J. Heat Mass Transf. 29, 1359–1369. https://doi.org/10.1016/0017-9310(86)90168-7

Ho, C.J., Viskanta, R., 1984. Heat transfer during melting from an isothermal vertical wall. J. Heat Transfer 106, 12–19. https://doi.org/10.1115/1.3246624

Holman, J.P., 1986. Heat Transfer, 6th ed. McGraw-Hill.

Humphries, W.R., Griggs, E.I., 1977. A design handbook for phase change thermal control and energy storage devices.

IRENA, 2020. Innovation Outlook: Thermal Energy Storage, International Renewable Energy Agency, Abu Dhabi.

Ismail, K.A.R., Henríquez, J.R., Moura, L.F.M., Ganzarolli, M.M., 2000. Ice formation around isothermal radial finned tubes. Energy Convers. Manag. 41, 585–605. https://doi.org/10.1016/S0196-8904(99)00128-4

Ismail, K.A.R., Lino, F.A.M., Machado, P.L.O., Teggar, M., Arıcı, M., Alves, T.A., Teles, M.P.R., 2022. New potential applications of phase change materials: A review. J. Energy Storage 53, 105202. https://doi.org/10.1016/j.est.2022.105202

Ismail, M., Zahra, W.K., Hassan, H., 2023. Experimental study of vapor compression refrigeration system enhanced via tubular heat exchanger incorporating single/dual phase change materials. Case Stud. Therm. Eng. 49, 103164. https://doi.org/10.1016/j.csite.2023.103164

Jany, P., Bejan, A., 1988. Scaling theory of melting with natural convection in an enclosure. Int. J. Heat Mass Transf. 31, 1221–1235. https://doi.org/10.1016/0017-9310(88)90065-8

Jayathunga, D., Weliwita, J.A., Karunathilake, H., Witharana, S., 2023. Economic Feasibility of Thermal Energy Storage-Integrated Concentrating Solar Power Plants. Solar 3, 132–160. https://doi.org/10.3390/solar3010010

Jouhara, H., Żabnieńska-Góra, A., Khordehgah, N., Ahmad, D., Lipinski, T., 2020. Latent thermal energy storage technologies and applications: A review. Int. J. Thermofluids 5–6, 100039. https://doi.org/10.1016/j.ijft.2020.100039

Kaabinejadian, A., Moghimi, M., Fakhari, I., 2023. Design, modeling, and thermo-economic optimization of an innovative continuous solar-powered hybrid desalination plant integrated with latent heat thermal energy storage. Appl. Therm. Eng. 219, 119576. https://doi.org/10.1016/j.applthermaleng.2022.119576

Kalapala, L., Devanuri, J.K., 2020. Energy and exergy analyses of latent heat storage unit positioned at different orientations – An experimental study. Energy 194, 116924. https://doi.org/10.1016/j.energy.2020.116924

Kamkari, B., Shokouhmand, H., Bruno, F., 2014. Experimental investigation of the effect of inclination angle on convection-driven melting of phase change material in a rectangular enclosure. Int. J. Heat Mass Transf. 72, 186–200. https://doi.org/10.1016/j.ijheatmasstransfer.2014.01.014

Kheirabadi, A.C., Groulx, D., 2015. The effect of the mushy-zone constant on simulated phase change heat transfer, in: International Symposium on Advances in Computational Heat Transfer. pp. 528–549. https://doi.org/10.1615/ICHMT.2015.IntSympAdvComputHeatTransf.460

Kohyani, M.T., Ghasemi, B., Raisi, A., Aminossadati, S.M., 2017. Melting of cyclohexane–Cu nano-phase change material (nano-PCM) in porous medium under magnetic field. J. Taiwan Inst. Chem. Eng. 77, 142–151. https://doi.org/10.1016/j.jtice.2017.04.037

Kuehn, T.H., Goldstein, R.J., 1976. Correlating equations for natural convection heat transfer between horizontal circular cylinders. Int. J. Heat Mass Transf. 19, 1127–1134. https://doi.org/10.1016/0017-9310(76)90145-9

Kurnia, J.C., Sasmito, A.P., 2018. Numerical investigation of heat transfer performance of a rotating latent heat thermal energy storage. Appl. Energy 227, 542–554. https://doi.org/10.1016/j.apenergy.2017.08.087

Lacroix, M., 1993. Numerical simulation of melting and resolidification of a phase change material around two cylindrical heat exchangers. Numer. Heat Transf. Part A Appl. 24, 143–160. https://doi.org/10.1080/10407789308902610

Lacroix, M., Benmadda, M., 1998. Analysis of natural convection melting from a heated wall with vertically oriented fins. Int. J. Numer. Methods Heat Fluid Flow 8, 465–478. https://doi.org/10.1108/09615539810213241

Le Gallo, M., Sebastian, A., 2020. An overview of phase-change memory device physics. J. Phys. D. Appl. Phys. 53. https://doi.org/10.1088/1361-6463/ab7794

Lewis, R.W., Roberts, P.M., 1987. Finite element simulation of solidification problems. Appl. Sci. Res. 44, 61–92. https://doi.org/10.1007/BF00412007

Li, H., Wang, N., He, S., Gao, M., 2022. Effect of inner-tube spacing on charging and discharging performance of latent energy storage heat exchangers. Appl. Therm. Eng. 216, 119112. https://doi.org/10.1016/j.applthermaleng.2022.119112

Li, W., Wang, J., Zhang, X., Liu, X., Dong, H., 2020. Experimental and numerical investigation of the melting process and heat transfer characteristics of multiple phase change materials. Int. J. Energy Res. 44, 11219–11232. https://doi.org/10.1002/er.5718

Liao, Z., Xu, C., Ren, Y., Gao, F., Ju, X., Du, X., 2018. A novel effective thermal conductivity correlation of the PCM melting in spherical PCM encapsulation for the packed bed TES system. Appl. Therm. Eng. 135, 116–122. https://doi.org/10.1016/j.applthermaleng.2018.02.048

Liu, C., Groulx, D., 2014. Experimental study of the phase change heat transfer inside a horizontal cylindrical latent heat energy storage system. Int. J. Therm. Sci. 82, 100–110. https://doi.org/10.1016/j.ijthermalsci.2014.03.014

Liu, J., Liu, Z., Nie, C., 2021. Phase transition enhancement through circumferentially arranging multiple phase change materials in a concentric tube. J. Energy Storage 40, 102672. https://doi.org/10.1016/j.est.2021.102672

Mahdi, J.M., Mohammed, H.I., Hashim, E.T., Talebizadehsardari, P., Nsofor, E.C., 2020. Solidification enhancement with multiple PCMs, cascaded metal foam and nanoparticles in the shell-and-tube energy storage system. Appl. Energy 257, 113993. https://doi.org/10.1016/j.apenergy.2019.113993

Mahdi, M.S., Hasan, A.F., Mahood, H.B., Campbell, A.N., Khadom, A.A., Karim, A.M. em A., Sharif, A.O., 2019. Numerical study and experimental validation of the effects of

orientation and configuration on melting in a latent heat thermal storage unit. J. Energy Storage 23, 456–468. https://doi.org/10.1016/j.est.2019.04.013

Mahdi, M.S., Mahood, H.B., Khadom, A.A., Campbell, A.N., 2021. Numerical simulations and experimental verification of the thermal performance of phase change materials in a tube-bundle latent heat thermal energy storage system. Appl. Therm. Eng. 194, 117079. https://doi.org/10.1016/j.applthermaleng.2021.117079

Mahdi, M.S., Mahood, H.B., Mahdi, J.M., Khadom, A.A., Campbell, A.N., 2020. Improved PCM melting in a thermal energy storage system of double-pipe helical-coil tube. Energy Convers. Manag. 203, 112238. https://doi.org/10.1016/j.enconman.2019.112238

Marušić, A., Lončar, D., 2020. Experimental validation of high-temperature latent heat storage model using melting front propagation data. Appl. Therm. Eng. 164. https://doi.org/10.1016/j.applthermaleng.2019.114520

Mat, S., Al-Abidi, A.A., Sopian, K., Sulaiman, M.Y., Mohammad, A.T., 2013. Enhance heat transfer for PCM melting in triplex tube with internal-external fins. Energy Convers. Manag. 74, 223–236. https://doi.org/10.1016/j.enconman.2013.05.003

Mehta, D.S., Solanki, K., Rathod, M.K., Banerjee, J., 2019. Thermal performance of shell and tube latent heat storage unit: Comparative assessment of horizontal and vertical orientation. J. Energy Storage 23, 344–362. https://doi.org/10.1016/j.est.2019.03.007

Mesalhy, O., Lafdi, K., Elgafy, A., Bowman, K., 2005. Numerical study for enhancing the thermal conductivity of phase change material (PCM) storage using high thermal conductivity porous matrix. Energy Convers. Manag. 46, 847–867. https://doi.org/10.1016/j.enconman.2004.06.010

Michels, H., Pitz-Paal, R., 2007. Cascaded latent heat storage for parabolic trough solar power plants. Sol. Energy 81, 829–837. https://doi.org/10.1016/j.solener.2006.09.008

Mostafavi Tehrani, S.S., Shoraka, Y., Diarce, G., Taylor, R.A., 2019. An improved, generalized effective thermal conductivity method for rapid design of high temperature shell-and-tube latent heat thermal energy storage systems. Renew. Energy 132, 694–708. https://doi.org/10.1016/j.renene.2018.08.038

Mourad, A., Aissa, A., Abed, A.M., Smaisim, G.F., Toghraie, D., Fazilati, M.A., Younis, O., Guedri, K., Alizadeh, A., 2022. The numerical analysis of the melting process in a modified shell-and-tube phase change material heat storage system. J. Energy Storage 55, 105827. https://doi.org/10.1016/j.est.2022.105827

Okada, M., 1984. Analysis of heat transfer during melting from a vertical wall. Int. J. Heat Mass Transf. 27, 2057–2066. https://doi.org/10.1016/0017-9310(84)90192-3

Patankar, S., 1980. Numerical heat transfer and fluid flow. Hemisphere Publishing Corporation.

Prud'homme, M., Nguyen, T.H., Mao, P.G., 1993. Numerical simulation of melting inside a rotating cylindrical enclosure. Int. J. Heat Mass Transf. 36, 57–69. https://doi.org/10.1016/0017-9310(93)80066-4

Raithby, G.D., Hollands, K.G.T., 1975. A General Method of Obtaining Approximate Solutions to Laminar and Turbulent Free Convection Problems. Adv. Heat Transf. 11, 265–315. https://doi.org/10.1016/S0065-2717(08)70076-5

Ramsey, J.W., Sparrow, E.M., 1978. Melting and Natural Convection Due to a Vertical Embedded Heater. J. Heat Transfer 100, 368–370. https://doi.org/10.1115/1.3450812

Reichl, C., Both, S., Mascherbauer, P., Emhofer, J., 2022. Comparison of Two CFD Approaches Using Constant and Temperature Dependent Heat Capacities during the Phase Transition in PCMs with Experimental and Analytical Results. Processes 10. https://doi.org/10.3390/pr10020302

Rocha, T.T.M., Teggar, M., Trevizoli, P.V., de Oliveira, R.N., 2023a. Potential of latent thermal energy storage for performance improvement in small-scale refrigeration units: A review. Renew. Sustain. Energy Rev. 187, 113746. https://doi.org/10.1016/j.rser.2023.113746

Rocha, T.T.M., Trevizoli, P.V., de Oliveira, R.N., 2023b. A timeline of the phase-change problem for latent thermal energy storage systems: A review of theoretical approaches from the 1970′s to 2022. Sol. Energy 250, 248–284. https://doi.org/10.1016/j.solener.2022.12.035

Rocha, T.T.M., Trevizoli, P.V., de Oliveira, R.N., 2023c. The role of the phase-change material properties, porosity constant, and their combination for melting problems using the enthalpy-porosity scheme. Therm. Sci. Eng. Prog. 102198. https://doi.org/10.1016/j.tsep.2023.102198

Rozenfeld, A., Kozak, Y., Rozenfeld, T., Ziskind, G., 2017. Experimental demonstration, modeling and analysis of a novel latent-heat thermal energy storage unit with a helical fin. Int. J. Heat Mass Transf. 110, 692–709. https://doi.org/10.1016/j.ijheatmasstransfer.2017.03.020

Saeed, A.M., Abderrahmane, A., Qasem, N.A.A., Mourad, A., Alhazmi, M., Ahmed, S.E., Guedri, K., 2022. A numerical investigation of a heat transfer augmentation finned pear-

shaped thermal energy storage system with nano-enhanced phase change materials. J. Energy Storage 53, 105172. https://doi.org/10.1016/j.est.2022.105172

Seddegh, S., Wang, X., Henderson, A.D., 2016. A comparative study of thermal behaviour of a horizontal and vertical shell-and-tube energy storage using phase change materials. Appl. Therm. Eng. 93, 348–358. https://doi.org/10.1016/j.applthermaleng.2015.09.107

Selvakumar, R.D., Qiang, L., Kang, L., Traoré, P., Wu, J., 2021. Numerical modeling of solid-liquid phase change under the influence an external electric field. Int. J. Multiph. Flow 136. https://doi.org/10.1016/j.ijmultiphaseflow.2020.103550

Shaker, M.Y., Sultan, A.A., El Negiry, E.A., Radwan, A., 2021. Melting and solidification characteristics of cylindrical encapsulated phase change materials. J. Energy Storage 43, 103104. https://doi.org/10.1016/j.est.2021.103104

Shakrina, G., Rivera-Tinoco, R., Bouallou, C., 2022. Numerical investigation and extensive parametric analysis of cryogenic latent heat shell and tube thermal energy storage system. Therm. Sci. Eng. Prog. 34, 101440. https://doi.org/10.1016/j.tsep.2022.101440

Shen, Y., Liu, Y., Liu, S., Mazhar, A.R., 2022. A dynamic method to optimize cascaded latent heat storage systems with a genetic algorithm: A case study of cylindrical concentric heat exchanger. Int. J. Heat Mass Transf. 183, 122051. https://doi.org/10.1016/j.ijheatmasstransfer.2021.122051

Shiruanian, A., Faghri, M., Zhang, Z., Asako, Y., 1998. Numerical solution of the effect of vibration on melting of unfixed rectangular phase-change material under variable-gravity environment. Numer. Heat Transf. Part A Appl. 34, 257–278. https://doi.org/10.1080/10407789808913986

Shmueli, H., Ziskind, G., Letan, R., 2010. Melting in a vertical cylindrical tube: Numerical investigation and comparison with experiments. Int. J. Heat Mass Transf. 53, 4082–4091. https://doi.org/10.1016/j.ijheatmasstransfer.2010.05.028

Shokouhmand, H., Kamkari, B., 2013. Experimental investigation on melting heat transfer characteristics of lauric acid in a rectangular thermal storage unit. Exp. Therm. Fluid Sci. 50, 201–212. https://doi.org/10.1016/j.expthermflusci.2013.06.010

Siegel, R., 1977. Solidification of low conductivity material containing dispersed high conductivity particles. Int. J. Heat Mass Transf. 20, 1087–1089. https://doi.org/10.1016/0017-9310(77)90195-8

Singh, R.P., Kaushik, S.C., Rakshit, D., 2020. Performance evaluation of charging process in a

cascade latent heat storage system (C-LHSS) based on heat flux DSC results. Int. J. Therm. Sci. 151, 106274. https://doi.org/10.1016/j.ijthermalsci.2020.106274

Souayfane, F., Biwole, P.H., Fardoun, F., 2018. Melting of a phase change material in presence of natural convection and radiation: A simplified model. Appl. Therm. Eng. 130, 660–671. https://doi.org/10.1016/j.applthermaleng.2017.11.026

Sparrow, E.M., Schmidt, R.R., Ramsey, J.W., 1978. Experiments on the Role of Natural Convection in the Melting of Solids. J. Heat Transfer 100, 11–16. https://doi.org/10.1115/1.3450484

Sun, J., Nawaz, K., Rendall, J., Elatar, A., Brechtl, J., 2023. Heat pump water heater enhanced with phase change materials thermal energy storage: Modeling study. Int. Commun. Heat Mass Transf. 146, 106917. https://doi.org/10.1016/j.icheatmasstransfer.2023.106917

Szekely, J., Chhabra, P.S., 1970. The effect of natural convection on the shape and movement of the melt-solid interface in the controlled solidification of lead. Metall. Mater. Trans. 1, 1195–1203. https://doi.org/10.1007/BF02900231

Taqi Al-Najjar, H.M., Mahdi, J.M., 2022. Novel mathematical modeling, performance analysis, and design charts for the typical hybrid photovoltaic/phase-change material (PV/PCM) system. Appl. Energy 315, 119027. https://doi.org/10.1016/j.apenergy.2022.119027

Teertstra, P., Yovanovch, M.M., 1998. Comprehensive review of natural convection in horizontal circular annuli. Am. Soc. Mech. Eng. Heat Transf. Div. HTD 357, 141–152.

Teertstra, P., Yovanovich, M.M., Culham, J.R., 2005. Analytical Modeling of Natural Convection in Horizontal Annuli, in: 43rd AIAA Aerospace Sciences Meeting and Exhibit. American Institute of Aeronautics and Astronautics, Reston, Virigina. https://doi.org/10.2514/6.2005-959

Thomas, B.G., Samarasekera, I. V., Brimacombe, J.K., 1984. Comparison of numerical modeling techniques for complex, two-dimensional, transient heat-conduction problems. Metall. Trans. B 15, 307–318. https://doi.org/10.1007/BF02667334

Tian, L.L., Liu, X., Chen, S., Shen, Z.G., 2020. Effect of fin material on PCM melting in a rectangular enclosure. Appl. Therm. Eng. 167. https://doi.org/10.1016/j.applthermaleng.2019.114764

Tian, Y., Zhao, C.Y., 2011. A numerical investigation of heat transfer in phase change materials (PCMs) embedded in porous metals. Energy 36, 5539–5546. https://doi.org/10.1016/j.energy.2011.07.019

Troxler, C.J., Freeman, T.B., Rodriguez, R.M., Boetcher, S.K.S., 2023. Experimental and Numerical Investigation of Lauric Acid Melting at Suboptimal Inclines. ASME Open J. Eng. 2, 1–14. https://doi.org/10.1115/1.4056348

UNFCCC, 2015. The Paris Agreement [WWW Document]. United Nations Framew. Conv. Clim. Chang. URL https://unfccc.int/process-and-meetings/the-paris-agreement/the-paris-agreement (accessed 8.9.21).

Vivès, C., 1988. Effects of a forced couette flow during the controlled solidification of a pure metal. Int. J. Heat Mass Transf. 31, 2047–2062. https://doi.org/10.1016/0017-9310(88)90116-0

Vogel, J., Johnson, M., 2019. Natural convection during melting in vertical finned tube latent thermal energy storage systems. Appl. Energy 246, 38–52. https://doi.org/10.1016/j.apenergy.2019.04.011

Vogel, J., Thess, A., 2019. Validation of a numerical model with a benchmark experiment for melting governed by natural convection in latent thermal energy storage. Appl. Therm. Eng. 148, 147–159. https://doi.org/10.1016/j.applthermaleng.2018.11.032

Voller, V., Cross, M., 1981. Accurate solutions of moving boundary problems using the enthalpy method. Int. J. Heat Mass Transf. 24, 545–556. https://doi.org/10.1016/0017-9310(81)90062-4

Voller, V.R., 1990. FAST IMPLICIT FINITE-DIFFERENCE METHOD FOR THE ANALYSIS OF PHASE CHANGE PROBLEMS. Numer. Heat Transf. Part B Fundam. 17, 155–169. https://doi.org/10.1080/10407799008961737

Voller, V.R., Cross, M., Markatos, N.C., 1987. An enthalpy method for convection/diffusion phase change. Int. J. Numer. Methods Eng. 24, 271–284. https://doi.org/10.1002/nme.1620240119

Voller, V.R., Prakash, C., 1987. A fixed grid numerical modelling methodology for convection-diffusion mushy region phase-change problems. Int. J. Heat Mass Transf. 30, 1709–1719. https://doi.org/10.1016/0017-9310(87)90317-6

Wang, H., Xu, H., Liu, C., Zhang, Z., Ling, X., Jiang, F., 2021. Numerical investigation of melting enhancement for paraffin in an innovative finned-plate latent heat thermal energy storage unit. J. Energy Storage 43, 103222. https://doi.org/10.1016/j.est.2021.103222

Wang, W.W., Zhang, K., Wang, L.B., He, Y.L., 2013. Numerical study of the heat charging and discharging characteristics of a shell-and-tube phase change heat storage unit. Appl.

Therm. Eng. 58, 542–553. https://doi.org/10.1016/j.applthermaleng.2013.04.063

Watanabe, T., Kanzawa, A., 1995. Second law optimization of a latent heat storage system with PCMS having different melting points. Heat Recover. Syst. CHP 15, 641–653. https://doi.org/10.1016/0890-4332(95)90044-6

Watanabe, T., Kikuchi, H., Kanzawa, A., 1993. Enhancement of charging and discharging rates in a latent heat storage system by use of PCM with different melting temperatures. Heat Recover. Syst. CHP 13, 57–66. https://doi.org/10.1016/0890-4332(93)90025-Q

Webb, B.W., Viskanta, R., 1985. On the characteristic length scale for correlating melting heat transfer data. Int. Commun. Heat Mass Transf. 12, 637–646. https://doi.org/10.1016/0735-1933(85)90016-8

Xu, Y., Zheng, Z.J., Chen, S., Cai, X., Yang, C., 2021. Parameter analysis and fast prediction of the optimum eccentricity for a latent heat thermal energy storage unit with phase change material enhanced by porous medium. Appl. Therm. Eng. 186, 116485. https://doi.org/10.1016/j.applthermaleng.2020.116485

Yan, P., Fan, W., Han, Y., Ding, H., Wen, C., Elbarghthi, A.F.A., Yang, Y., 2023. Leaf-vein bionic fin configurations for enhanced thermal energy storage performance of phase change materials in smart heating and cooling systems. Appl. Energy 346, 121352. https://doi.org/10.1016/j.apenergy.2023.121352

Yang, H.D., Oh, Y.K., 2007. A study on melting phenomena and enhanced heat transfer of phase change material by ultrasonic vibrations. Key Eng. Mater. 345-346 II, 889–892. https://doi.org/10.4028/www.scientific.net/kem.345-346.889

Yang, H.D., Oh, Y.K., 2006. Experimental and Numerical Study on Enhanced Heat Transfer of Solid-Liquid PCM by Ultrasonic Wave. Key Eng. Mater. 326–328, 1145–1148. https://doi.org/10.4028/www.scientific.net/kem.326-328.1145

Yang, L., Cao, X., Zhang, N., Xiang, B., Zhang, Z., Qian, B., 2019. Thermal reliability of typical fatty acids as phase change materials based on 10,000 accelerated thermal cycles. Sustain. Cities Soc. 46, 101380. https://doi.org/10.1016/j.scs.2018.12.008

Ye, W., Khodadadi, J.M., 2022. Effects of arrow-shape fins on the melting performance of a horizontal shell-and-tube latent heat thermal energy storage unit. J. Energy Storage 54, 105201. https://doi.org/10.1016/j.est.2022.105201

Yen, Y.-C., 1966. Natural convection in ice melting from below, Cold Regions Research and Engineering Laboratory (U.S.).

Youdelis, W. V., Colton, D.R., Cahoon, J., 1964. ON THE THEORY OF ALLOY SOLIDIFICATION IN A MAGNETIC FIELD. Can. J. Phys. 42, 2238–2258. https://doi.org/10.1139/p64-205

Yuan, Y., Cao, X., Xiang, B., Du, Y., 2016. Effect of installation angle of fins on melting characteristics of annular unit for latent heat thermal energy storage. Sol. Energy 136, 365–378. https://doi.org/10.1016/j.solener.2016.07.014

Zeneli, M., Malgarinos, I., Nikolopoulos, A., Nikolopoulos, N., Grammelis, P., Karellas, S., Kakaras, E., 2019. Numerical simulation of a silicon-based latent heat thermal energy storage system operating at ultra-high temperatures. Appl. Energy 242, 837–853. https://doi.org/10.1016/j.apenergy.2019.03.147

Zeneli, M., Nikolopoulos, A., Karellas, S., Nikolopoulos, N., 2021. Numerical methods for solid-liquid phase-change problems, in: Ultra-High Temperature Thermal Energy Storage, Transfer and Conversion. LTD, pp. 165–199. https://doi.org/10.1016/B978-0-12-819955-8.00007-7

Zhang, L., Yang, P., Li, W., Klemeš, J.J., Zeng, M., Wang, Q., 2022. A new structure of PCHE with embedded PCM for attenuating temperature fluctuations and its performance analysis. Energy 254. https://doi.org/10.1016/j.energy.2022.124462

Zhen-Xiang, G., Mujumdar, A.S., 1995. A new solar receiver thermal store for space-based activities using multiple composite phase-change materials. J. Sol. Energy Eng. Trans. ASME 117, 215–220. https://doi.org/10.1115/1.2847798

APPENDIX A – DERIVATION OF THE DISCRETIZED EQUATIONS FOR THE SIMPLIFIED MODEL

Different discretized equations must be written for central and boundary volumes, although the same governing equation apply to them all, as presented by Eq. 38. After integrating it over a volume and rearranging, Eq. A1 is found, which is valid for the whole domain.

$$\frac{\left(h_{\mathrm{P}}-{h_{\mathrm{P}}}^{0}\right)\Delta r.\Delta \mathrm{z}.r_{\mathrm{P}}}{\Delta t} = \left(\alpha r\left.\frac{\partial h}{\partial r}\right|_{\mathrm{n}}-\alpha r\left.\frac{\partial h}{\partial r}\right|_{\mathrm{s}}\right)\Delta \mathrm{z}+\left(\alpha\left.\frac{\partial h}{\partial z}\right|_{\mathrm{e}}-\alpha\left.\frac{\partial h}{\partial z}\right|_{\mathrm{w}}\right)\Delta r.r_{\mathrm{P}} - \frac{\rho L\left(f_{\mathrm{P}}-{f_{\mathrm{P}}}^{0}\right)\Delta r.\Delta \mathrm{z}.r_{\mathrm{P}}}{\Delta t} \tag{A1}$$

For the central volumes, the first order derivatives are approximated by central differences, as presented in Eq. A2.

$$\alpha r\left.\frac{\partial h}{\partial r}\right|_{\mathrm{n}} = \alpha_{\mathrm{n}} r_{\mathrm{n}}\frac{(h_{\mathrm{N}}-h_{\mathrm{P}})}{\Delta r_{\mathrm{n}}} \tag{A2a}$$

$$\alpha r\left.\frac{\partial h}{\partial r}\right|_{\mathrm{s}} = \alpha_{\mathrm{s}} r_{\mathrm{s}}\frac{(h_{\mathrm{P}}-h_{\mathrm{S}})}{\Delta r_{\mathrm{s}}} \tag{A2b}$$

$$\alpha\left.\frac{\partial h}{\partial z}\right|_{\mathrm{e}} = \alpha_{\mathrm{e}}\frac{(h_{\mathrm{E}}-h_{\mathrm{P}})}{\Delta z} \tag{A2c}$$

$$\alpha\left.\frac{\partial h}{\partial z}\right|_{\mathrm{w}} = \alpha_{\mathrm{w}}\frac{(h_{\mathrm{P}}-h_{\mathrm{W}})}{\Delta z} \tag{A2d}$$

Substituting Eq. A2 into Eq. A1 and rearranging, Eq. 38 is found, with the coefficients given by Eq. 39. For boundary volumes, different conditions apply, therefore, distinct coefficients must be written. Considering the nomenclature given in Figure A1, the first order derivatives, for each volume, are given in Eqs. A3-A7.

Figure A1. Nomenclature to derive the coefficients of Eq. 38 for the boundary volumes.

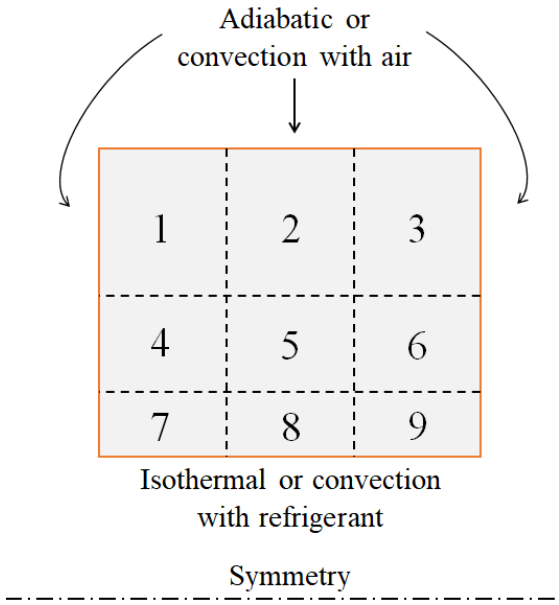

Source: the author.

Volume 1

-Convective boundary condition

For the north face:

$$k r_{\mathrm{n}} \left.\frac{\partial T}{\partial r}\right|_{\mathrm{n}} = \alpha r_{\mathrm{n}} \left.\frac{\partial h}{\partial r}\right|_{\mathrm{n}} = r_{\mathrm{n}} h_{\mathrm{air}} (T_{\mathrm{air}} - T_{\mathrm{wall}}) = \frac{(T_{\mathrm{wall}} - T)}{\ln\left(\frac{r_{\mathrm{n}}}{r_{\mathrm{P}}}\right)/k} = \frac{T_{\mathrm{air}} - T}{\frac{1}{r_{\mathrm{n}} h_{\mathrm{air}}} + \ln\left(\frac{r_{\mathrm{n}}}{r_{\mathrm{P}}}\right)/k}$$

Using the definition of sensible enthalpy, $h = \rho c_{\mathrm{p}} (T - T_{\mathrm{m}})$, the boundary condition take the form of Eq. A3.

$$\alpha r_{\mathrm{n}} \left.\frac{\partial h}{\partial r}\right|_{\mathrm{n}} = \frac{\rho c_{\mathrm{p}} (T_{\mathrm{air}} - T_{\mathrm{m}}) - h_{\mathrm{P}}}{\rho c_{\mathrm{p}} \left[\frac{1}{r_{\mathrm{n}} h_{\mathrm{air}}} + \ln\left(\frac{r_{\mathrm{n}}}{r_{\mathrm{P}}}\right)/k\right]} \tag{A3}$$

In a similar fashion for the west face:

$$-k \left.\frac{\partial T}{\partial z}\right|_{\mathrm{w}} = -\alpha \left.\frac{\partial h}{\partial z}\right|_{\mathrm{w}} = h_{\mathrm{air}} (T_{\mathrm{air}} - T_{\mathrm{wall}}) = \frac{(T_{\mathrm{wall}} - T)}{\left(\frac{\Delta z}{2}\right)/k} = \frac{T_{\mathrm{air}} - T}{\frac{1}{h_{\mathrm{air}}} + \frac{\Delta z}{2k}}$$

Using the enthalpy definition, the west derivative is written by Eq. A4.

$$-\alpha \left.\frac{\partial h}{\partial z}\right|_{\mathrm{w}} = \frac{\rho c_{\mathrm{p}} (T_{\mathrm{air}} - T_{\mathrm{m}}) - h_{\mathrm{P}}}{\rho c_{\mathrm{p}} \left[\frac{1}{h_{\mathrm{air}}} + \frac{\Delta z}{2k}\right]} \tag{A4}$$

The remaining faces assumes the derivatives given by Eq. A2.

-Adiabatic boundary condition

The same equations developed above for the convective boundary conditions can be used by setting the convective coefficient equal to a very small value.

Volume 2

The only boundary is the north face and its derivative is the same as that of volume 1.

Volume 3

The derivative of the north face is the same as that of volume 1. For the east face, Eq. A5 can be written.

$$\alpha \left.\frac{\partial h}{\partial z}\right|_{\mathrm{e}} = \frac{\rho c_{\mathrm{p}}(T_{\mathrm{air}} - T_{\mathrm{m}}) - h_{\mathrm{P}}}{\rho c_{\mathrm{p}}\left[\frac{1}{h_{\mathrm{air}}} + \frac{\Delta z}{2k}\right]} \tag{A5}$$

Volume 4

The west derivative is the same as that of volume 1.

Volume 6

The derivative of face east is the same as that of volume 3.

Volume 7

The west derivative is the same as that of volume 1. The south face can be subject to convection, due to the flow of refrigerant fluid, or to a constant temperature.

-Convective boundary condition

$$-kr_{\mathrm{s}} \left.\frac{\partial T}{\partial r}\right|_{\mathrm{s}} = -\alpha r_{\mathrm{s}} \left.\frac{\partial h}{\partial r}\right|_{\mathrm{s}} = r_{\mathrm{s}} h_{\mathrm{r}}(T_{\mathrm{r}} - T_{\mathrm{wall}}) = \frac{(T_{\mathrm{wall}} - T)}{\ln\left(\frac{r_{\mathrm{P}}}{r_{\mathrm{s}}}\right)/k} = \frac{T_{\mathrm{r}} - T}{\frac{1}{r_{\mathrm{s}} h_{\mathrm{r}}} + \ln\left(\frac{r_{\mathrm{P}}}{r_{\mathrm{s}}}\right)/k}$$

Using the definition of sensible enthalpy, the boundary condition take the form of Eq. A6.

$$-\alpha r_{\mathrm{s}} \left.\frac{\partial h}{\partial r}\right|_{\mathrm{s}} = \frac{\rho c_{\mathrm{p}}(T_{\mathrm{r}} - T_{\mathrm{m}}) - h_{\mathrm{P}}}{\rho c_{\mathrm{p}}\left[\frac{1}{r_{\mathrm{s}} h_{\mathrm{r}}} + \ln\left(\frac{r_{\mathrm{P}}}{r_{\mathrm{s}}}\right)/k\right]} \tag{A6}$$

-Isothermal condition

$$-kr_{\mathrm{s}}\left.\frac{\partial T}{\partial r}\right|_{\mathrm{s}} = -\alpha r_{\mathrm{s}}\left.\frac{\partial h}{\partial r}\right|_{\mathrm{s}} = \frac{(T_{\mathrm{wall}} - T)}{\ln\left(\frac{r_{\mathrm{P}}}{r_{\mathrm{s}}}\right)/k}$$

With the definition of sensible enthalpy, Eq. A7 is found.

$$-\alpha r_{\mathrm{s}}\left.\frac{\partial h}{\partial r}\right|_{\mathrm{s}} = \frac{\rho c_{\mathrm{p}}(T_{\mathrm{wall}} - T_{\mathrm{m}}) - h_{\mathrm{P}}}{\rho c_{\mathrm{p}}\left[\ln\left(\frac{r_{\mathrm{P}}}{r_{\mathrm{s}}}\right)/k\right]} \tag{A7}$$

For implementation purposes, only Eq. A6 is considered. If the isothermal condition applies, then the convective coefficient is set to a very small value and the refrigerant temperature is assumed equal to the wall temperature. Doing so, Eq. A6 becomes the same as Eq. A7.

Volume 8

The derivative of face south is the same as that of volume 7.

Volume 9

The derivative of face south is the same as that of volume 7, while for face east it is the same as that of volume 3.

Finally, when Eq. A1, with the corresponding derivatives (Eqs. A3 to A7), is cast in the form of Eq. 38, the coefficients for each boundary volume are those presented in Table A1. In practice, due to the high length/diameter ratio of the PCM heat exchanger considered in this work, the areas of the west and east boundaries become negligible, such that adiabatic conditions may be imposed.

Table A1. Coefficients of Eq. 38 for each boundary volume.

Volume	A_{N}	A_{S}	A_{E}	A_{W}	A_{P}	B
1	0	$\frac{\Delta z}{\Delta r_{\mathrm{s}}}\alpha_{\mathrm{s}} r_{\mathrm{s}}$	$\frac{\Delta r}{\Delta z_{\mathrm{e}}}\alpha_{\mathrm{e}} r_{\mathrm{P}}$	0	$A_{\mathrm{S}} + A_{\mathrm{E}} + \frac{r_{\mathrm{P}}\Delta z\Delta r}{\Delta t} + \frac{\Delta \mathrm{z}}{\rho c_{\mathrm{p}}\left[\frac{1}{r_{\mathrm{n}} h_{\mathrm{air}}} + \ln\left(\frac{r_{\mathrm{n}}}{r_{\mathrm{P}}}\right)/k\right]} + \frac{\Delta r . r_{\mathrm{P}}}{\rho c_{\mathrm{p}}\left[\frac{1}{h_{\mathrm{air}}} + \frac{\Delta z}{2k}\right]}$	$\frac{r_{\mathrm{P}}\Delta z\Delta r}{\Delta t}\left[{h_{\mathrm{P}}}^{0} + \rho L\left({f_{\mathrm{P}}}^{0} - f_{\mathrm{P}}\right)\right] + \frac{(T_{\mathrm{air}} - T_{\mathrm{m}})\Delta \mathrm{z}}{\left[\frac{1}{r_{\mathrm{n}} h_{\mathrm{air}}} + \ln\left(\frac{r_{\mathrm{n}}}{r_{\mathrm{P}}}\right)/k\right]} + \frac{(T_{\mathrm{air}} - T_{\mathrm{m}})\Delta r . r_{\mathrm{P}}}{\left[\frac{1}{h_{\mathrm{air}}} + \frac{\Delta z}{2k}\right]}$
2	0	$\frac{\Delta z}{\Delta r_{\mathrm{s}}}\alpha_{\mathrm{s}} r_{\mathrm{s}}$	$\frac{\Delta r}{\Delta z_{\mathrm{e}}}\alpha_{\mathrm{e}} r_{\mathrm{P}}$	$\frac{\Delta r}{\Delta z_{\mathrm{w}}}\alpha_{\mathrm{w}} r_{\mathrm{P}}$	$A_{\mathrm{S}} + A_{\mathrm{E}} + A_{\mathrm{W}} + \frac{r_{\mathrm{P}}\Delta z\Delta r}{\Delta t} + \frac{\Delta \mathrm{z}}{\rho c_{\mathrm{p}}\left[\frac{1}{r_{\mathrm{n}} h_{\mathrm{air}}} + \ln\left(\frac{r_{\mathrm{n}}}{r_{\mathrm{P}}}\right)/k\right]}$	$\frac{r_{\mathrm{P}}\Delta z\Delta r}{\Delta t}\left[{h_{\mathrm{P}}}^{0} + \rho L\left({f_{\mathrm{P}}}^{0} - f_{\mathrm{P}}\right)\right] + \frac{(T_{\mathrm{air}} - T_{\mathrm{m}})\Delta \mathrm{z}}{\left[\frac{1}{r_{\mathrm{n}} h_{\mathrm{air}}} + \ln\left(\frac{r_{\mathrm{n}}}{r_{\mathrm{P}}}\right)/k\right]}$
3	0	$\frac{\Delta z}{\Delta r_{\mathrm{s}}}\alpha_{\mathrm{s}} r_{\mathrm{s}}$	0	$\frac{\Delta r}{\Delta z_{\mathrm{w}}}\alpha_{\mathrm{w}} r_{\mathrm{P}}$	$A_{\mathrm{S}} + A_{\mathrm{W}} + \frac{r_{\mathrm{P}}\Delta z\Delta r}{\Delta t} + \frac{\Delta \mathrm{z}}{\rho c_{\mathrm{p}}\left[\frac{1}{r_{\mathrm{n}} h_{\mathrm{air}}} + \ln\left(\frac{r_{\mathrm{n}}}{r_{\mathrm{P}}}\right)/k\right]} + \frac{\Delta r . r_{\mathrm{P}}}{\rho c_{\mathrm{p}}\left[\frac{1}{h_{\mathrm{air}}} + \frac{\Delta z}{2k}\right]}$	$\frac{r_{\mathrm{P}}\Delta z\Delta r}{\Delta t}\left[{h_{\mathrm{P}}}^{0} + \rho L\left({f_{\mathrm{P}}}^{0} - f_{\mathrm{P}}\right)\right] + \frac{(T_{\mathrm{air}} - T_{\mathrm{m}})\Delta \mathrm{z}}{\left[\frac{1}{r_{\mathrm{n}} h_{\mathrm{air}}} + \ln\left(\frac{r_{\mathrm{n}}}{r_{\mathrm{P}}}\right)/k\right]} + \frac{(T_{\mathrm{air}} - T_{\mathrm{m}})\Delta r . r_{\mathrm{P}}}{\left[\frac{1}{h_{\mathrm{air}}} + \frac{\Delta z}{2k}\right]}$
4	$\frac{\Delta z}{\Delta r_{\mathrm{n}}}\alpha_{\mathrm{n}} r_{\mathrm{n}}$	$\frac{\Delta z}{\Delta r_{\mathrm{s}}}\alpha_{\mathrm{s}} r_{\mathrm{s}}$	$\frac{\Delta r}{\Delta z_{\mathrm{e}}}\alpha_{\mathrm{e}} r_{\mathrm{P}}$	0	$A_{\mathrm{N}} + A_{\mathrm{S}} + A_{\mathrm{E}} + \frac{r_{\mathrm{P}}\Delta z\Delta r}{\Delta t} + \frac{\Delta r . r_{\mathrm{P}}}{\rho c_{\mathrm{p}}\left[\frac{1}{h_{\mathrm{air}}} + \frac{\Delta z}{2k}\right]}$	$\frac{r_{\mathrm{P}}\Delta z\Delta r}{\Delta t}\left[{h_{\mathrm{P}}}^{0} + \rho L\left({f_{\mathrm{P}}}^{0} - f_{\mathrm{P}}\right)\right] + \frac{(T_{\mathrm{air}} - T_{\mathrm{m}})\Delta r . r_{\mathrm{P}}}{\left[\frac{1}{h_{\mathrm{air}}} + \frac{\Delta z}{2k}\right]}$

6	$\frac{\Delta z}{\Delta r_{\mathrm{n}}}\alpha_{\mathrm{n}}r_{\mathrm{n}}$	$\frac{\Delta z}{\Delta r_{\mathrm{s}}}\alpha_{\mathrm{s}}r_{\mathrm{s}}$	0	$\frac{\Delta r}{\Delta z_{\mathrm{w}}}\alpha_{\mathrm{w}}r_{\mathrm{P}}$	$A_{\mathrm{N}}+A_{\mathrm{S}}+A_{\mathrm{W}}+\frac{r_{\mathrm{P}}\Delta z\Delta r}{\Delta t}+\frac{\Delta r.r_{\mathrm{P}}}{\rho c_{\mathrm{p}}\left[\frac{1}{h_{\mathrm{air}}}+\frac{\Delta z}{2k}\right]}$	$\frac{r_{\mathrm{P}}\Delta z\Delta r}{\Delta t}\left[{h_{\mathrm{P}}}^{0}+\rho L\left({f_{\mathrm{P}}}^{0}-f_{\mathrm{P}}\right)\right]+\frac{(T_{\mathrm{air}}-T_{\mathrm{m}})\Delta r.r_{\mathrm{P}}}{\left[\frac{1}{h_{\mathrm{air}}}+\frac{\Delta z}{2k}\right]}$
7	$\frac{\Delta z}{\Delta r_{\mathrm{n}}}\alpha_{\mathrm{n}}r_{\mathrm{n}}$	0	$\frac{\Delta r}{\Delta z_{\mathrm{e}}}\alpha_{\mathrm{e}}r_{\mathrm{P}}$	0	$A_{\mathrm{N}}+A_{\mathrm{E}}+\frac{r_{\mathrm{P}}\Delta z\Delta r}{\Delta t}+\frac{\Delta r.r_{\mathrm{P}}}{\rho c_{\mathrm{p}}\left[\frac{1}{h_{\mathrm{air}}}+\frac{\Delta z}{2k}\right]}+\frac{\Delta \mathrm{z}}{\rho c_{\mathrm{p}}\left[\frac{1}{r_{\mathrm{s}}h_{\mathrm{r}}}+\ln\left(\frac{r_{\mathrm{P}}}{r_{\mathrm{s}}}\right)/k\right]}$	$\frac{r_{\mathrm{P}}\Delta z\Delta r}{\Delta t}\left[{h_{\mathrm{P}}}^{0}+\rho L\left({f_{\mathrm{P}}}^{0}-f_{\mathrm{P}}\right)\right]+\frac{(T_{\mathrm{air}}-T_{\mathrm{m}})\Delta r.r_{\mathrm{P}}}{\left[\frac{1}{h_{\mathrm{air}}}+\frac{\Delta z}{2k}\right]}+\frac{(T_{\mathrm{r}}-T_{\mathrm{m}})\Delta \mathrm{z}}{\left[\frac{1}{r_{\mathrm{s}}h_{\mathrm{r}}}+\ln\left(\frac{r_{\mathrm{P}}}{r_{\mathrm{s}}}\right)/k\right]}$
8	$\frac{\Delta z}{\Delta r_{\mathrm{n}}}\alpha_{\mathrm{n}}r_{\mathrm{n}}$	0	$\frac{\Delta r}{\Delta z_{\mathrm{e}}}\alpha_{\mathrm{e}}r_{\mathrm{P}}$	$\frac{\Delta r}{\Delta z_{\mathrm{w}}}\alpha_{\mathrm{w}}r_{\mathrm{P}}$	$A_{\mathrm{N}}+A_{\mathrm{E}}+A_{\mathrm{W}}+\frac{r_{\mathrm{P}}\Delta z\Delta r}{\Delta t}+\frac{\Delta \mathrm{z}}{\rho c_{\mathrm{p}}\left[\frac{1}{r_{\mathrm{s}}h_{\mathrm{r}}}+\ln\left(\frac{r_{\mathrm{P}}}{r_{\mathrm{s}}}\right)/k\right]}$	$\frac{r_{\mathrm{P}}\Delta z\Delta r}{\Delta t}\left[{h_{\mathrm{P}}}^{0}+\rho L\left({f_{\mathrm{P}}}^{0}-f_{\mathrm{P}}\right)\right]+\frac{(T_{\mathrm{r}}-T_{\mathrm{m}})\Delta \mathrm{z}}{\left[\frac{1}{r_{\mathrm{s}}h_{\mathrm{r}}}+\ln\left(\frac{r_{\mathrm{P}}}{r_{\mathrm{s}}}\right)/k\right]}$
9	$\frac{\Delta z}{\Delta r_{\mathrm{n}}}\alpha_{\mathrm{n}}r_{\mathrm{n}}$	0	0	$\frac{\Delta r}{\Delta z_{\mathrm{w}}}\alpha_{\mathrm{w}}r_{\mathrm{P}}$	$A_{\mathrm{N}}+A_{\mathrm{W}}+\frac{r_{\mathrm{P}}\Delta z\Delta r}{\Delta t}+\frac{\Delta \mathrm{z}}{\rho c_{\mathrm{p}}\left[\frac{1}{r_{\mathrm{s}}h_{\mathrm{r}}}+\ln\left(\frac{r_{\mathrm{P}}}{r_{\mathrm{s}}}\right)/k\right]}+\frac{\Delta r.r_{\mathrm{P}}}{\rho c_{\mathrm{p}}\left[\frac{1}{h_{\mathrm{air}}}+\frac{\Delta z}{2k}\right]}$	$\frac{r_{\mathrm{P}}\Delta z\Delta r}{\Delta t}\left[{h_{\mathrm{P}}}^{0}+\rho L\left({f_{\mathrm{P}}}^{0}-f_{\mathrm{P}}\right)\right]+\frac{(T_{\mathrm{r}}-T_{\mathrm{m}})\Delta \mathrm{z}}{\left[\frac{1}{r_{\mathrm{s}}h_{\mathrm{r}}}+\ln\left(\frac{r_{\mathrm{P}}}{r_{\mathrm{s}}}\right)/k\right]}+\frac{(T_{\mathrm{air}}-T_{\mathrm{m}})\Delta r.r_{\mathrm{P}}}{\left[\frac{1}{h_{\mathrm{air}}}+\frac{\Delta z}{2k}\right]}$

Source: the author.

APPENDIX B – REFRIGERATION CYCLE FOR POTENTIAL APPLICATION OF LATENT THERMAL ENERGY STORAGE

The simplified model developed in this work could be employed to investigate the behavior of a small-scale refrigeration cycle coupled with PCMs. This cycle shall be composed of the following components: compressor, oil separator, condenser, filter-drier, capillary tube, evaporator, and accumulator. A schematic representation of the small-scale apparatus to validate the refrigeration model is presented in Figure B.1, while a representation of the model for such cycle is illustrated in Figure B.2.

Figure B.1. Schematic of the experimental apparatus. P: pressure sensor; T: temperature sensor.

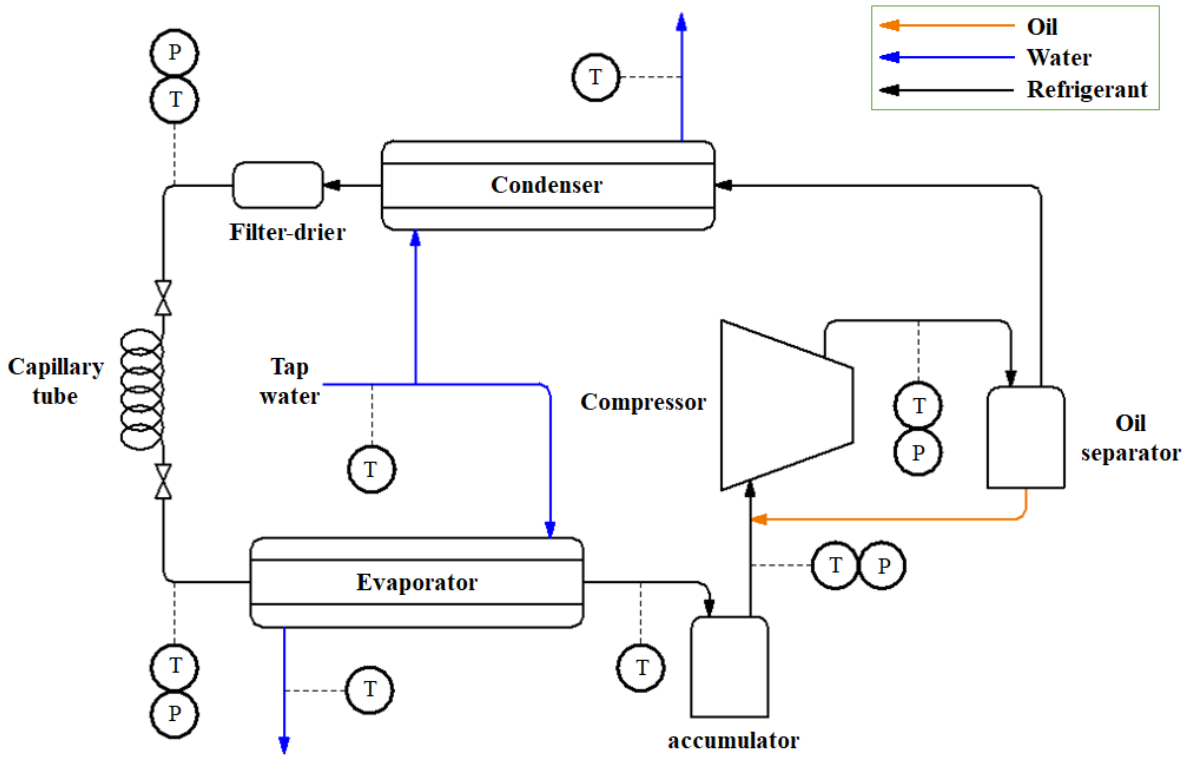

Source: the author.

Figure B.2. List of input/output variables used in the refrigeration model.

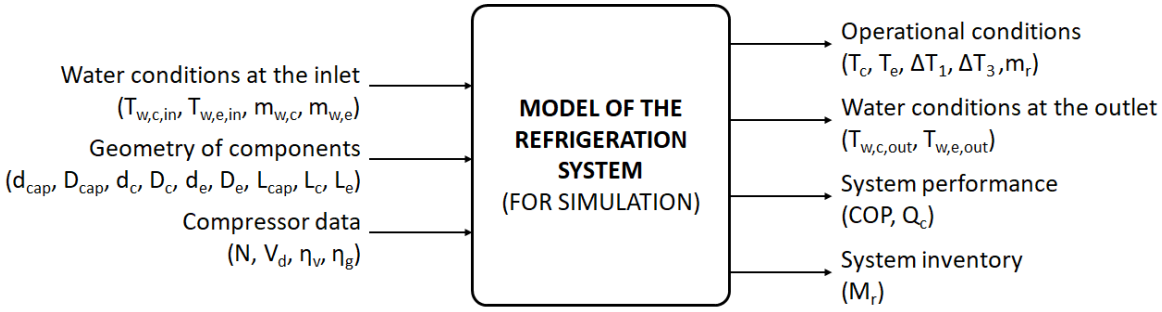

Source: the author.

where T is temperature, m is the mass flow rate, d and D is are diameters, L is length, COP is the coefficient of performance, Q is the heat transfer rate, N is the rotational speed, V_{d} is the volumetric displacement, and η is efficiency. The subscripts w, r, c, e, in, out, cap, v, and g denote water, refrigerant, condenser, evaporator, inlet, outlet, capillary tube, volumetric, and global, respectively.